



AGH

AGH UNIVERSITY OF SCIENCE AND TECHNOLOGY

Faculty of Physics and Applied Computer Science

Department of Condensed Matter Physics

DOCTORAL DISSERTATION

*Physiochemical properties of nanocomposites based on
 $M_xFe_{3-x}O_4$ magnetic nanoparticles and polythiophene*

Author: mgr Roma Wirecka
Main Discipline: Physical sciences

First Supervisor: prof. dr hab. inż. Andrzej Bernasik
Second Supervisor: prof. dr hab. Szczepan Zapotoczny

Krakow, 2023

OŚWIADCZENIE AUTORA ROZPRAWY

Oświadczam, świadoma odpowiedzialności karnej za poświadczenie nieprawdy, że niniejszą rozprawę doktorską wykonałam osobiście i samodzielnie oraz, że nie korzystałam z innych źródeł niż wymienione w pracy.

12 maja 2023 r.

.....

mgr Roma Wirecka

OŚWIADCZENIA PROMOTORÓW

Niniejsza rozprawa jest gotowa do oceny przez recenzentów.

12 maja 2023 r.

.....

prof. dr hab. inż. Andrzej Bernasik

.....

prof. dr hab. Szczepan Zapotoczny



**European
Funds**

Knowledge Education Development



European Union

European
Social Fund

This doctoral dissertation was prepared under the Operational Program Knowledge Education Development, project number POWR.03.02.00-00-I004/16, co-funded by the European Union.



**ACADEMIC CENTRE
FOR MATERIALS
AND NANOTECHNOLOGY AGH**

This doctoral dissertation was supported by the infrastructure of the Academic Centre For Materials And Nanotechnology AGH.

Abstract

This dissertation establishes and presents an approach that may be taken, while designing and developing new conducting nanocomposites based on magnetic nanoparticles and conjugated polymers.

The main goal of the first phase of this research, was to study the influence of content of dopants on size, shape and magnetic properties of metal oxide nanoparticles. To achieve that the synthesis of iron oxide and zinc ferrite nanoparticles was realized with thorough analysis using numerous methods like vibrating sample magnetometry, X-ray photoelectron spectroscopy, transmission electron microscopy and more. In addition, the presence of a shell, made of capping agents used during the synthesis, was observed and studied. Such a shell adds additional interface which must be taken into consideration, while designing nanocomposites based on polymers and nanoparticles. This issue was further investigated in the following parts of the study.

In the next step, a unique measurement procedure was established. It was proposed that proper application of X-ray photoelectron spectroscopy combined with Gas Cluster Ion Beam allows to study the chemical composition of not only the surface of nanoparticles, but also the deeper layers of measured samples. What is more important, it was proven that here established procedure of sample's sputtering, allows to study subsequent shells of nanoparticles without changing the states of elements present in the sample, which sometimes may be an issue.

Then, I have proposed an altered method of synthesis of nanoparticles involving conjugated polymers during the whole process of nanoparticle formation to resolve the problem of additional layer covering nanoparticles. As a result, there was less control over the morphology, but the shell was modified, so that the electrical conductivity of pure nanoparticles was observed. What is more, two distinct nanocomposites, based on two different types of nanoparticles, were formed (using the classical and newly designed synthesis protocol), and enhanced electrical properties of newly designed nanoparticles were shown.

Finally, the study presents the comparison of resistance of six different nanocomposites. Namely, magnetite, cobalt ferrite and nickel ferrite nanoparticles, obtained following the classical and newly designed synthesis protocol, were mixed with poly(3-hexylthiophene-2,5-diyl). Subsequently, not only their electrical resistance was measured, but also the electric response in the external magnetic field, changing in the range of up to 1500 mT, was studied for four out of sixed samples. As a result, I have obtained over 5% change in the resistivity for the nanocomposite based on iron oxide nanoparticles synthesized in the presence of conjugated polymer. On the other hand, similar nanocomposite, but with nanoparticles coated with surfactant capping agents, showed only 1% of such alteration,

proving that the interface engineering is a crucial point in nanocomposite materials of that type.

To sum up, during my doctoral studies I have modified and created a synthetic protocol which allows to obtain nanoparticles with two distinct shells – electrically insulating or conducting. What is more, the importance of interface between the nanocomposite's components was evidenced, which paves the way for enhancement of the electromagnetic response in the field of inorganic/organic nanocomposites.

Streszczenie

Celem niniejszej rozprawy jest przedstawienie procedury projektowania i wytwarzania nowych kompozytów przewodzących na bazie nanocząstek magnetycznych i polimerów skoniugowanych.

W początkowej fazie badań skupiono się na syntezie nanocząstek tlenku żelaza i ferrytów cynku o różnej zawartości domieszek. Zastosowanie takich technik badawczych jak magnetometria z wibrującą sondą, spektroskopia fotoelektronów z zakresu promieniowania X, transmisyjna mikroskopia elektronowa oraz inne, pozwoliło na określenie wpływu zawartości domieszek na rozmiar, kształt i własności magnetyczne otrzymanych nanocząstek. Ponadto zaobserwowano obecność otoczki zbudowanej z zastosowanych podczas syntezy środków powierzchniowo czynnych, która dodaje dodatkową warstwę na granicy pomiędzy nanocząstką a polimerem, co powinno być wzięte pod uwagę w trakcie projektowania nanokompozytu. Obecność powłoki była tematem kolejnego etapu pracy.

Kolejnym krokiem było opracowanie procedury pomiarowej nanocząstek, która pozawalałaby na pomiar składu nie tylko powierzchni, ale również rdzenia materiału. Zaproponowano, aby za pomocą spektroskopii fotoelektronów w zakresie promieniowania X w połączeniu z rozpylaniem jonowym działem klastrowym możliwe było nie tylko badanie składu chemicznego powierzchni nanocząstek, ale także głębszych warstw próbek. Dodatkowo udowodniono, że zastosowana metoda rozpylania powierzchniowego pozwala na badanie głębszych warstw powierzchni nanocząstek bez zmiany stanu chemicznego próbki, co jest częstym problemem w podobnych układach.

W celu rozwiązania problemu dodatkowej warstwy pokrywającej nanocząstki, opracowano zmodyfikowaną syntezę, w której polimer był obecny podczas całego procesu formowania nanocząstek. W rezultacie kontrola nad morfologią była mniejsza, jednakże powłoka została zmodyfikowana, a nanocząstki wykazały zdolność przewodzenia prądu elektrycznego. Stworzono również, dwa odrębne nanokompozyty, oparte na dwóch różnych typach nanocząstek (otrzymanymi w obecności i bez obecności polimeru podczas syntezy), oraz pokazano ulepszone właściwości elektryczne nowo opracowanych materiałów.

Końcowym etapem badań było zbadanie odpowiedzi elektrycznej sześciu różnych nanokompozytów opartych na nanocząstkach magnetycznych i polimerze skoniugowanym. Nanocząstki magnetytu, ferrytu kobaltu i ferrytu niklu, otrzymane zgodnie z pierwszą i nowo opracowaną syntezą, zmieszano z poli(3-heksylofeno-2,5-diylenem) i zbadano ich odpowiedź elektryczną w zewnętrznym polu magnetycznym, osiągającym wartość do 1500 mT. W efekcie uzyskano ponad 5% zmianę rezystywności nanokompozytu na bazie nanocząstek tlenku żelaza syntetyzowanego w obecności skoniugowanego polimeru. Warto nadmienić, że podobny nanokompozyt, ale z

nanocząstkami pokrytymi środkami powierzchniowymi, wykazywał tylko 1% zmianę odpowiedzi elektrycznej.

Podsumowując, podczas moich studiów doktoranckich zmodyfikowałam i opracowałam syntezę nanocząstek magnetycznych z dwoma różnymi powłokami. Pozwoliło mi to na stworzenie nanokompozytów i zbadanie ich przewodnictwa w zewnętrznym polu magnetycznym w szerokim zakresie temperatur. W zależności od rdzenia i powłoki użytych nanocząstek, nanokompozyty różniły się zmianą oporu w zewnętrznym polu magnetycznym. Dodatkowo udowodniłam, że podczas projektowania nanokompozytów do zastosowania w elektronice należy pamiętać o wpływie interfejsu między związkami nieorganicznymi i organicznymi. Wszystko to, może znacząco wpłynąć na odpowiedź elektromagnetyczną materiałów otrzymywanych w przyszłości.

Table of Contents

Abstract	6
Streszczenie	8
The structure of the dissertation.....	11
Introduction.....	13
Synthesis of magnetic nanoparticles	13
Synthesis of nanocomposites	13
Interfaces in nanomaterials	15
Electrical conductivity of nanoparticle based polymer nanocomposites	16
Magnetic Field Effects (MFE)	16
Synthesis of nanoparticles	19
Distribution of dopants in iron oxide based nanoparticles.....	21
Shell of the nanoparticle and its influence on the electrical conductivity.....	25
Magnetoelectrically responsive nanocomposites based on magnetic nanoparticles	28
Summary	31
Abbreviations.....	37
My articles and conferences.....	38
Articles	38
Conferences	39
Reprints of publications and Statements of Authors contribution	40

The structure of the dissertation

This doctoral thesis describes my published findings in the fields of magnetic nanoparticles and magnetoelectric hybrid nanocomposites. The research was focused on the impact of the nanoparticles' shell on the electrical conductivity and magnetoresistive response of the nanocomposites consisting of magnetic nanoparticles and conjugated polymer. The dissertation is based on four publications, which were published in the international journals from the Thomson Scientific Master Journal List, and are as follows:

[1] Lachowicz D., Wirecka R., Górka-Kumik W., Marzec M. M., Gajewska M., Kmita A., Żukrowski J., Sikora M., Zapotoczny S., Bernasik A., „Gradient of zinc content in core-shell zinc ferrite nanoparticles – precise study on composition and magnetic properties”, *Physical Chemistry Chemical Physics*, 2019, 21(42), 23473, doi: 10.1039/c9cp03591e

[2] Wirecka R., Marzec M. M., Marciszko-Wiąckowska M., Lis M., Gajewska M., Trynkiewicz E., Lachowicz D., Bernasik A., „The effect of shell modification in iron oxide nanoparticles on electrical conductivity in polythiophene-based nanocomposites”, *Journal of Materials Chemistry C*, 2021, 9(32), 10453, doi: 10.1039/d1tc02949e

[3] Wirecka R., Lachowicz D., Berent K., Marzec M. M., Bernasik A., „Ion distribution in iron oxide, zinc and manganese ferrite nanoparticles studied by XPS combined with argon gas cluster ion beam sputtering”, *Surfaces and Interfaces*, 2022, 30, 101865, doi: 10.1016/j.surfin.2022.101865

[4] Wirecka R., Maćkosz K., Żywczak A., Marzec M. M., Zapotoczny S., Bernasik A., „Magnetoresistive Properties of Nanocomposites Based on Ferrite Nanoparticles and Polythiophene”, *Nanomaterials*, 2023, 13(5), 879; doi: 10.3390/nano13050879

This work consists of three general parts. Firstly, the introduction describes the aim and focus of my research, additionally showing the importance of such study in the field. The second part consist of four chapters describing and summarizing the findings of the aforementioned articles, which should help in understanding the path that was taken in my studies. Lastly, I have created a summary of all my work done during my doctoral studies, in the field of magnetic nanoparticles and organic electronics to demonstrate the relevance of my research. At the end of the thesis, there is a chapter consisting of articles with statements of authorship, list of my achievements, conferences I have participated in, and all scientific articles to which I have contributed.

My contribution to the presented articles

During my doctoral studies and the preparation of the abovementioned articles, I was responsible for:

- Optimization and performing the syntheses of nanoparticles in squalene and dodecanoic acid;
- Modification and performing the syntheses of nanoparticles in P3HT;
- Design and synthesis of nanocomposites;
- Analysis of TEM results;
- All XPS measurements were conducted and analyzed by me. Discussions were carried out with M.M. Marzec and A. Bernasik;
- Sample preparation for VSM measurements, with partial contribution to their analyses;
- Sample preparation for conductivity measurements in dark and under illumination, and all connected measurements;
- Sample preparation for conductivity measurements in the external magnetic field, and all connected measurements;

I prepared the XPS analysis and TEM analysis chapters and I was involved in the formulation of the main goals of the studies presented in the article entitled: „Gradient of zinc content in core-shell zinc ferrite nanoparticles – precise study on composition and magnetic properties”. For the three remaining articles, I was the main author of the manuscripts in which I conducted most or all experiments and participated in the conceptual part of the studies. The discussions were carried with all the authors. What is more, I was responsible for the design and writing of the first drafts of the manuscripts.

Introduction

Synthesis of magnetic nanoparticles

Thanks to numerous potential as well as already commercialized applications of magnetic nanoparticles based on iron oxides, they have attracted great scientific interest. As a result, many routes to obtain oxides with precisely controlled size, morphology and magnetic properties, were developed [5]. The commonly used synthesis methods include (co)precipitation, electrochemical, solvothermal and thermal decomposition [6].

One of the simplest approach to synthesize iron oxide nanoparticles is by using (co)precipitation method applying iron salts in an aqueous medium. It allows to get a large amount of the product in an affordable and fast way. However, the synthesis medium (water) typically results in a surface functionalization of nanoparticles with hydroxylic groups that may lead to their aggregation and poor stability in non-polar solvents [7]. Nevertheless, such nanoparticles may be good candidates for biological applications, like hyperthermia [8]. When nanoparticles are supposed to be used in organic solvents, the poor stability may be tackled by ligand exchange, which increases their stability in organic solvents [9]. As an alternative method, creating a shell over the magnetic core may be applied. Another problem may be related to the control over diameter, size distribution or shape that in the coprecipitation approach is often not satisfying, nor reproducible [10].

Another interesting synthesis route is a thermal decomposition method. Typically, in this group of syntheses, metalloorganic compounds are mixed with solvents and surface control agents (capping agents) and are heated up to approx. 300°C. In such a high temperature, the decomposition of metalloorganic compounds occurs and formation of nanoparticles takes place [11]. Depending on the temperature, time of decomposition, and used components, it is possible to obtain nanoparticles of different sizes, shapes, ion distribution or magnetic properties [12]. Additionally, the control over the physical properties is relatively good, syntheses are reproducible, and nanoparticles are stable in organic solvents. All of that makes this group of syntheses a perfect candidate to obtain nanoparticles for organic-inorganic nanocomposites. On the negative side - most syntheses are made only in the small batches, because of potential problems with heating distribution in large syntheses vessels. Additionally, the presence of capping agents may result in creation of shell made of them, covering the magnetic core of nanoparticles [13], which may impact the interface between nanoparticle and another material.

Synthesis of nanocomposites

The properties of nanocomposites based on nanomaterials and polymers depend on several factors, among which the four most important are: the properties of the materials that make the composite, the quality of dispersion of one component in another, the

homogeneity of the entire material, and the interactions between the matrix and the filler [14]. Depending on the properties we want to focus on, one of four main methods of obtaining nanocomposites can be selected.

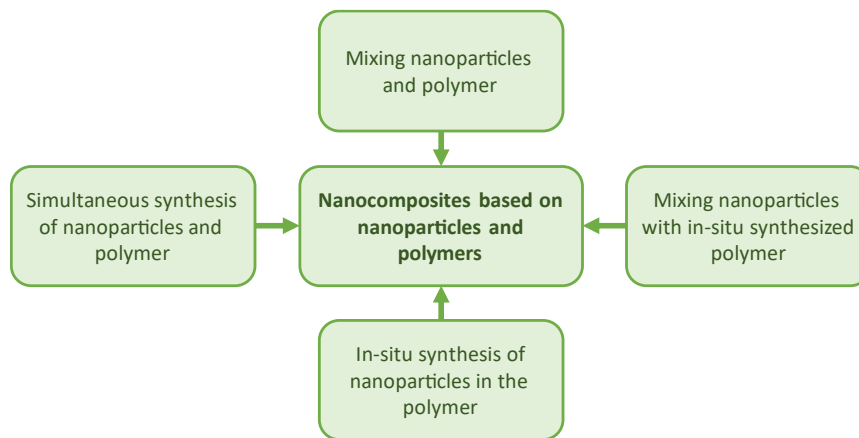


Figure 1. Summary of different approaches to create nanocomposites based on nanoparticles and polymers.

The methods of obtaining nanocomposites, not only differ in potential results and final properties, but also the difficulty may rise with introduced alterations (Figure 1). The simplest way, and probably the most popular one, is to obtain nanoparticles and polymer separately before creating nanocomposite, and then mix them together [15]. It results in obtaining a material of potentially isolated ingredients, with no control over the interface, with clustered nanoparticles between the polymer chains. The final properties of such formed composites may not be as good as in more complex approaches, but still materials with improved toughness or enhanced power conversion efficiency in solar cells may be obtained [16,17].

The two other methods involve either synthesis of a polymer in the presence of nanoparticles, or nanoparticles in the presence of a polymer. For the first one, we can possibly obtain the polymer with desired parameters, for example, if we want to design composites with increased toughness and selectivity for polymer based membranes [18,19]. Unfortunately, in this approach nanoparticles may influence the chain formation and the physicochemical properties of obtained polymer [20,21]. In the second approach, we can synthesize nanoparticles in the already formed polymer. This may result in better connections between nanoparticles and macromolecules, which is very important if we want to use such nanocomposite in e.g., electrical devices [22]. When no insulating shell is present on the surface of nanoparticles, their electrical properties may enhance the properties of the whole nanocomposite [23]. Unfortunately, using this procedure may result in polymer degradation or irregularity of shape and size of nanoparticles if no shape controlling substances (capping agents) are used. These two methods give us more control over the connection made between the components but are far more complicated than the simple mixing of nanoparticles in the polymer matrix. In addition, it may be very hard to synthesize particles with small size distribution or a shape of choice. In case of

polymer synthesis, it may bring unexpected results with high chain length distribution. In case of conducting polymers, it is highly probable that the conductivity of such compound will be poor as it relies highly on the regioregularity of a polymer chain.

The last and the most difficult approach is to design and perform simultaneous synthesis of both materials [24]. This potentially may bring the best results, because we can precisely choose the properties of the nanoparticles used, and the polymer used. Unfortunately, this kind of synthesis is very hard to perform, as it combines the drawbacks of two beforementioned approaches [25].

Interfaces in nanomaterials

One of the most important advantage of using organic compounds in composite materials for electronic applications is their distinguishing characteristics – no oxidating and insulating form is created on their surface when exposed to air [26]. This results in undisturbed interface between organic/organic or organic/inorganic material, with possibly enhanced control over engineering of such interface which impacts the properties of a nanocomposite.

In organic electronics, the interface influences the mobility, charge transport, width of energy bandgap and overall efficiency of a device [27]. One of interesting example is organic photovoltaics (OPVs), in which newly designed devices have numerous interfaces, and the careful engineering of those allows to obtain power conversion efficiencies which can compete with classical silicon-based photovoltaics [28]. At the border between electron accepting material and electron donor material, the exciton diffusion and dissociation takes places which directly impacts the efficiency of the OPV. The creation of a complex, interpenetrating layer, highly increases the area between two materials and the transport of charge carriers is facilitated, as well as a number of recombined electron/hole pairs is diminished [16]. What is more, the addition of layers in such devices, increase the spectrum of photons that can be absorbed, and enhances the energy level alignment between the donor and acceptor materials, which may enhance the power conversion efficiency. At the border of these layers, the interface must be carefully modelled to minimize the loss of charge carriers [26].

Another interesting use of the interface engineering is coating of nanoparticles with shells to enhance their magnetic response or biocompatibility [29,30]. In one of the studies, the problem of dangling bonds of iron in iron oxide nanoparticles was analyzed and resolved. The iron atoms at the surface of nanoparticle negatively influence the magnetic response of the material, but coating of the iron oxide surface with gold was proposed to create a nanocomposite in which the noble metal atoms stabilize the dangling bonds of Fe_3O_4 , which increase their resemblance to the core of nanoparticles [30].

Electrical conductivity of nanoparticle based polymer nanocomposites

The conduction mechanisms in metal based systems have been thoroughly studied, and the theory behind it is accepted, but the description of conduction in organic materials is more complex. There are many theories of charge transport in organic materials but they have number of limitations [31–34]. What is more, if nanocomposites are considered additives can dramatically change the mechanism of conductivity, so it may be very hard to propose a mechanism, which will describe the electrical conductivity of organic/inorganic nanocomposites. It is worth mentioning that even a small amount of nanoparticles (<1 vol.%) can increase the conductivity of a polymer-based nanocomposite by a factor of $\sim 10^8$. To achieve such good results, the careful engineering of nanomaterials (nanoparticles, nanowires, nanotubes etc.) based on the understanding of the relation between structure and properties is a must [31].

The variable range hopping model of conductivity in amorphous materials is often used to describe the conduction mechanisms in nanoparticle/polymer nanocomposites. This model is based on an assumption that the charge carriers with variable activation energy may “hop” between sites by the certain length, which is increasing with the decrease of the temperature. Recently, this model was used to describe the electrical conductivity in the nanocomposites based on polyaniline and magnetic nanoparticles for which, after the addition of nanoparticles, the conductivity decreased from $\sim 60 \text{ } \Omega/\text{cm}$ (for pure polymer) to the $\sim 300 \text{ } \Omega/\text{cm}$ (polyaniline mixed with cobalt ferrite). Such behavior was ascribed to the creation of isolated islands of nanoparticles in the polymer matrix. What is more, the change in the conductivity varied between magnetite and ferrite nanoparticles, showing that even a small difference in a type of filler may have a significant impact of the electrical properties of the final nanocomposite [35].

Magnetic Field Effects (MFE)

Some properties of organic semiconducting materials may change when the external magnetic field is applied. Such phenomenon is called Magnetic Field Effect, and it can affect the electrical conductivity, photoluminescence, photocurrent, dielectric constant, and many more parameters. The effect is the result of spin-dependent carrier recombination, exciton dissociation, and electric polarization, and the general value of MFE may be calculated by the formulae presented below:

$$MFE = \frac{S_B - S_0}{S_0}$$

In which S_B is a measured value of a chosen parameter (for example resistance) under the applied external magnetic field and S_0 is the measured value without applied external magnetic field. The MFE is typically presented in percentage. The external magnetic field influences the spin mixing and spin conserving process, which may result in the positive or negative change of the measured value [36].

One of the interesting examples of MFE is the magnetoresistance. It is a change of resistivity (hence conductivity) of a substance in the external magnetic field and it was observed for numerous materials and systems. There are five types of magnetoresistive phenomena: ordinary, anisotropic, tunnelling, giant and colossal magnetoresistance. Additionally, if change of resistivity is observed in organic materials, in which no magnetic material is present, then it may be called as organic magnetoresistance. The organic magnetoresistance is typically not as strong as for the metallic materials, but it created a new field of studies thanks to flexible and semitransparent properties of such materials, which can be used for magnetic field sensors, or even used in electronics. Since magnetic field influences the spin, a new field emerged – organic spintronics [37].

Worth mentioning are the hardships connected to the magnetic field effects in the organic or hybrid materials. It is important to acknowledge that there are numerous potential phenomena occurring between two materials, which may greatly affect the final performance of the systems including e.g. organic magnetoresistance. Additionally, giant magnetoresistance or tunnelling magnetoresistance may be observed, as well as anisotropic phenomena, so to be able to improve the future hybrid spintronic devices, the interface between materials should be well established, with a reliable tracking of the source of MFEs in the final devices [38].

Motivation and aim

Composites based on magnetic nanoparticles and electrically conducting polymers are of high interest due to possibility to alter their physiochemical properties in numerous ways, their sustainability and low costs of production. As our understanding of such materials expands rapidly and significantly, one day they may become the basis for cheap, rapidly produced and environmentally friendly organic electronic devices. However, to achieve that, much more studies must be conducted to fully understand what and how influences the final properties of such hybrid materials.

The motivation behind this dissertation was not only to study factors influencing the electromagnetic response of polymer based nanocomposites, but also to analyze the interface between nanoparticles and polymers. Thorough analysis of a border between matrix and the filler could be a study that was missing to better understand the phenomena occurring in such systems. An additional motivation, yet not less important part of this study, was to get an insight into the nanoparticles formation process, with the emphasis on different shells. What is more, the procedure that would allow to analyze the distribution of different compounds in the core and shell of iron oxide based nanoparticles and not destroy the chemical composition of the sample itself, was missing in the field of nanoparticles.

The aim of this work was to propose the method to enhance the electromagnetic response of the nanocomposites based on electrically conductive polymers and magnetic nanoparticles. Until now, numerous studies have shown that the introduction of the nanoparticles to the polymer matrix has an impact on the electric response of the final composite but detailed understanding of the influence of various factors on the physiochemical properties of such materials was missing. What is more, a clear path how such a response can be altered and enhanced was not yet paved.

The study presented in this dissertation, showing the influence of iron oxide based nanoparticles on the electromagnetic response of the nanocomposites with polymer matrix, namely poly(3-hexylthiophene-2,5-diyl), paves the way to the improvement of such response in similar systems, which may broaden application of the composites in the field of organic electronics.

Synthesis of nanoparticles

In the hybrid systems based on nanoparticles and polymers it is important not only to analyze the properties of nanoparticles, but also to understand the interface and its role in the final properties of the materials.

Based on the article entitled: "Gradient of zinc content in core-shell zinc ferrite nanoparticles – precise study on composition and magnetic properties".

One of the important things that needs to be taken into consideration while creating a nanocomposite or hybrid material, is to be able to synthesize nanoparticles in a controlled manner with the properties that will be of use in the final material. For that purpose, I synthesized four different types of nanoparticles: iron oxide and three zinc ferrites with different zinc content. I chose the modified thermal decomposition method in a controlled gas atmosphere as a synthesis procedure, which uses organometallic compounds as an iron oxides precursor. As a size and shape controlling substances squalene and dodecanoic acid were used, which also affect the boiling temperature of the reactive mixture. The goal was to obtain superparamagnetic nanoparticles with high saturation magnetization (M_s) and to study how different synthetic parameters affect the shape and structure of the nanoparticles.

To confirm that the obtained products are in fact nanoparticles, the transmission electron microscopy was used while the energy dispersive X-ray spectroscopy allowed to confirm the presence of iron, zinc and oxygen in the samples. The average size of the iron oxide nanoparticles was determined to be equal to 28.6 ± 3.4 nm. For the rest of the samples the sizes of the nanoparticles decreased with the increasing content of zinc and ranged from 22.3 ± 2.6 nm, through 11.2 ± 1.4 nm to 9.6 ± 0.9 nm. Based on the TEM micrograph some magnetic interactions between the nanoparticles may be expected.

To further exploit the magnetic properties of obtained nanoparticles, I prepared samples for the VSM and MS measurements. The measurements confirmed that the dominant phase is superparamagnetic, with saturation magnetization between 70 to 85 emu/g at 80 K. Based on a weak correlation between the size of nanoparticles and the temperature maxima observed in the zero field cooling curve, the VSM measurements suggested the core/shell structure of the nanoparticles. The MS measurements indicated similar characteristics as the results showed non-homogenous distribution of zinc in the ferrites structures. In the next steps of the study, I observed the core/shell structure of the nanoparticles not only related to the zinc inclusions, but also the organic layer at the outer shell of the nanoparticles.

During the synthesis I used squalene and dodecanoic acid acting as the capping agents to ensure small size distribution and regular shapes of the nanoparticles. The TGA was used to check if this compounds attach to the surface of nanoparticles permanently. The results

showed that the samples have high content of organic matter, varying in the range 17%-20.6% depending on the sample. These results allowed to estimate the thickness of the carbon outer layer on the nanoparticles, which was found to be 4.1 nm for iron oxide, and between 3.0 to 1.5 nm for the zinc ferrites, depending on the zinc content.

Since the interface between two materials formed in hybrid systems is one of the main factors influencing the properties of the final nanocomposite, I decided to perform full X-ray photoelectron spectroscopy analysis (XPS) combined with the Argon Gas Cluster Ion Beam sputtering (GCIB). Using GCIB allowed me to reveal the composition of the samples, layer by layer, with highly reduced risk of changing the chemical structure of sputtered material. I analyzed the C1s region and showed that the lines of O-C=O, which can be assigned to dodecanoic acid, have higher concentration in the samples consisting of smaller nanoparticles, which suggest that the acid has the largest impact on the size of the nanoparticles. For the zinc ferrite nanoparticles, two types of structures were observed: the high zinc content layer is between the carbon layer and the mostly iron core, or the core of the nanoparticle is made of the zinc rich phase covered with iron rich shell. Comparing the precursors content in the reactive mixture prior to the synthesis, the results from the ICP-OES and XPS, allowed me to conclude that if the amount of zinc is high then it will be mostly incorporated in the core of the nanoparticles, but if the zinc content is small it will cover the iron rich core (see Figure 2).

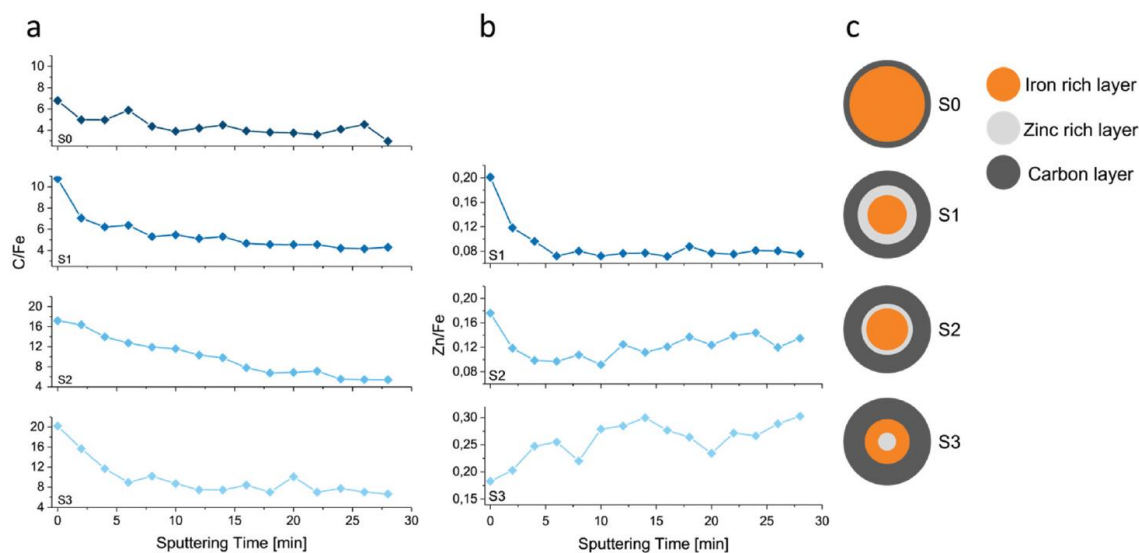


Figure 2. Atomic concentration ratio of (a) C/Fe and (b) Zn/Fe determined from XPS measurements combined with Ar-GCIB sputtering measured after every 2 minutes of sputtering; (c) core/shell model structures proposed on the basis of the obtained results [1]

This study gave me good insight into the factors influencing the size and magnetic properties of nanoparticles. Furthermore, the carbon shell, which is a result of the chosen way of synthesis, is unavoidable and may be thick enough to have negative insulating impact especially if such nanoparticles will be used in the polymer/nanoparticle hybrid.

Distribution of dopants in iron oxide based nanoparticles

X-ray photoelectron spectroscopy is a surface sensitive method which can measure chemical composition of a material with the sampling depth up to 10 nm. As one of the goals of my studies was to characterize the surface of the nanoparticles, this method was chosen, as it is precise, nondestructive and greatly informative. In addition, XPS can be enhanced with sputtering guns: monoatomic and cluster, which can remove the surface impurities or provide us with the depth profiles of the measured samples. Knowing that, I decided that the next part of my study should be focused on developing the measurement protocol for nanoparticles and optimizing the fitting procedure of Fe2p spectra to reflect the structure characterized by other methods, which can be of use in the investigation of a core/shell structure of nanomaterials.

Based on the article entitled: "Ion distribution in iron oxide, zinc and manganese ferrite nanoparticles studied by XPS combined with argon gas cluster ion beam sputtering"

To analyze the impact of XPS and sputtering method on the structure of chosen nanoparticles, firstly I checked the influence of X-rays on the iron oxide crystal. As expected, even after extended exposure time (170 minutes) of irradiation, the spectra of Fe2p region did not change. This proved that the longtime of X-ray based measurement has no altering effect on the iron oxide structure, and even long time of irradiation during depth profiling will not false the results.

Secondly, I checked the influence of Ar⁺ monoatomic sputtering on the chemical state of iron. The iron oxide crystal was sputtered 17 times for 1 minute at a time. In the middle of the sputtering the reduced to the ground state iron (Fe⁰) line appeared, which indicated, that the sputtering will reduce the iron present in the sample. Moreover, the shape and intensity of the satellite region changed significantly suggesting that the line connected to the Fe²⁺ satellite is increasing and the line connected to the defected states of iron is becoming more prominent. Knowing that, I could conclude that the monoatomic gun should not be used to characterize the core/shell structure of nanoparticles, and another approach is necessary.

Lastly, I checked the influence of GCIB sputtering on the structure of zinc ferrite nanoparticles. The first approach was to sputter for two minutes, measure and analyze the same spot for 7 subsequent series. As a result, the sputtering lasted for 14 minutes, during which most of the carbon layer was removed, and the iron rich layer was revealed. The zinc content was stable during the whole measurement. Surprisingly, when I removed the sample from the apparatus there was a visible square in the center of the substrate. After the SEM examination, it was concluded that, when the carbon layer was removed from the nanoparticles, they were probably sintered by the X-ray radiation. Knowing that another approach was proposed, and from now, the sputtering would be done in one

place, but the XPS measurement would be taken from 16 different spots in the range of the sputtering area (the spot-by-spot procedure, with schematics shown in Figure 3).

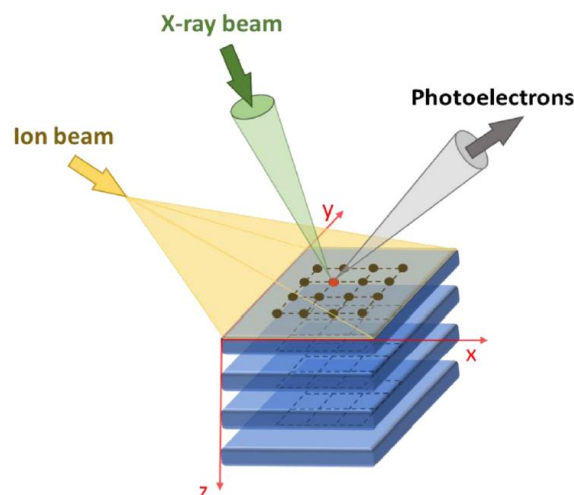


Figure 3. Schematic view of the procedure of sputtering and spectra acquisition in the Spot-by-Spot Procedure. Each dot represents spot of $100\ \mu\text{m}$ in diameter which was irradiated by the X-ray beam [3].

Firstly, I conducted the measurement on the iron oxide crystal to optimize the procedure on a fully characterized sample. During the optimization of the fitting procedure, I decided to analyze only one part of the Fe2p region, the Fe2p_{3/2}, because the Fe2p_{1/2} region has lower intensity and as the binding energy rises (the measurement error may be larger). With the use of GCIB I was able to obtain a depth profile for 16 subsequent layers of the samples. At the surface I confirmed presence of the Fe₂O₃, which upon further removal, changed to the Fe₃O₄ with 1:1:1 ratio of three different iron species (Fe²⁺_{octa}:Fe³⁺_{octa}:Fe³⁺_{tetra}), and two satellites present in the positions similar to that found in the literature. This model I have used to characterize four types of nanoparticles: iron oxide, zinc ferrite, manganese ferrite and zinc-manganese ferrite. I synthesized all nanoparticles using the same synthesis protocol (modified thermal decomposition method), with the same iron to dopant ratio, and with the same size and morphology of the final product.

The XPS results showed that pure iron oxide nanoparticles were covered with a carbon layer under which some non-stoichiometric iron oxide was found. After five cycles of 2 minutes of sputtering, the 1:1:1 ratio of iron species was observed, with two satellites line, meaning that the core of the nanoparticle is made of magnetite. Based on the XPS results and the fitting procedure created based on the iron oxide crystal, I concluded that the core/shell structure of the nanoparticle was made of (from the core) Fe₃O₄ followed by the layer of α - or γ -Fe₂O₃ (and Fe_xO_y) and a shell made of squalene and dodecanoic acid, which I used as capping agents during the synthesis (for atomic concentrations of all four types of nanoparticles, please see Figure 4).

Second nanoparticles that I studied, were manganese ferrites. Similarly, nanoparticles were covered with carbon layer, followed by some non-stoichiometric iron oxides. During the sputtering concentration of manganese was decreasing along with the thinning of the FWHM of iron states, which may mean that some iron states connected to the manganese in the structure are less abundant in the core area. As a result of changes in the concentration of different metal ions, I proposed that the manganese may replace some Fe^{2+} ions at the surface of the nanoparticles. Moreover, I observed two states of manganese in the structure of the nanoparticles - Mn^{2+} and Mn^{3+} . During the sputtering the proportion $\text{Mn}^{2+}:\text{Mn}^{3+}$ is moving towards the access of Mn^{3+} , which was an important observation. Typically, when using ion sputtering, the ion state of metal ions may reduce, but here I observed the exact opposite, which indicates that the GCIB sputtering applied with the spot-by-spot procedure can be used to analyze depth profiles of metal oxide materials in a reliable manner without damaging the chemical structure of the studied materials.

The third type of nanoparticles I studied were zinc ferrites. Typically, in the stoichiometric ZnFe_2O_4 , the spinel structure changes from inverse (observed for magnetite) to normal. In case of these nanoparticles, line ascribed to $\text{Fe}^{2+}_{\text{octa}}$ is present, but no characteristic features in the satellite region can be found (the intensities of two satellite lines are similar) suggesting that the iron phase is made of α - or γ - Fe_2O_3 with the inclusions of zinc ferrite. What is more, the concentration of iron and zinc remains stable during 30 minutes of sputtering. As a result of this analysis, I concluded that zinc can stabilize the structure of the nanoparticle, and if used in the zinc/iron molar ratio of 0.2/0.8 it is possible to obtain a homogenous ferrite throughout the nanoparticle.

The last nanoparticles I studied, were based on two dopants: zinc and manganese. During sputtering, the ratio between iron states is not changing, and the FWHMs for the dopants are stable and similar to this for the beforehand described ferrites, except that additional line in the zinc region was observed. Such results suggest that manganese may occupy similar interstices, regardless the presence of zinc in the structure, but for zinc the atoms may occupy different states if other dopant are introduced during the synthesis.

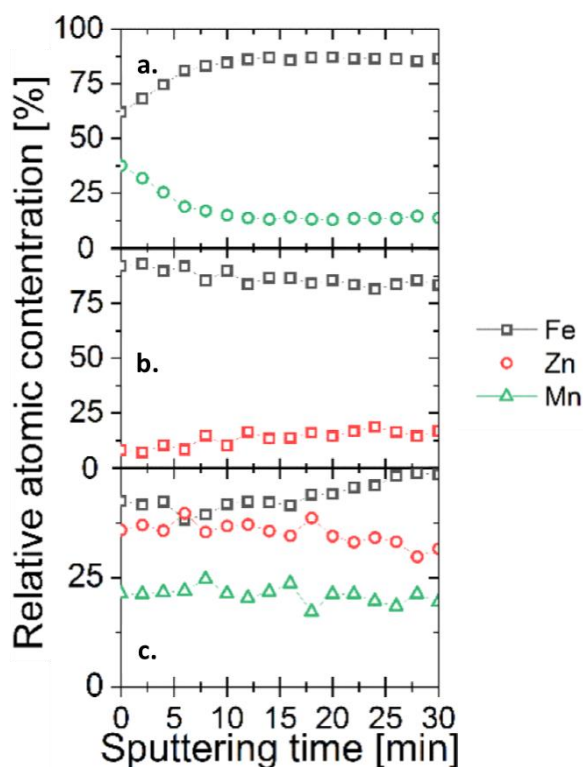


Figure 4. Graphs representing changes in the relative atomic concentration for iron, zinc and mangan in the (a) Mn(Sq), (b) Zn(Sq) and (c) for MnZn(Sq) nanoparticles after every two minutes of Ar-GCIB sputtering. In case of Mn(Sq), after 10 minutes of sputtering the concentration of iron and dopant is stabilizing in the structure of the nanoparticle. In case of two other types of materials, the concentration is not altering during the sputtering.

All of the studies and analyses I conducted and presented were an important part of the characterization method created for the iron oxide based nanoparticles. These results showed that, depending on the used dopant (and its amount), the structure of the final product may be different, which greatly increased my understanding of the ferrites and iron oxides composition-structure relationships. Additionally, I showed that GCIB and spot-by-spot procedure does not reduce the oxidation state of metal ions, which was of great importance for a reliable study of the structure and interfaces in the next stage of my doctoral studies.

Shell of the nanoparticle and its influence on the electrical conductivity

My XPS studies showed, that carbon shell, made of squalene and dodecanoic acid in the synthesized nanoparticles, is unavoidable, and it's thickness may negatively impact the electrical properties of the nanoparticles. As I presented the ability to synthesize different types of ferrite nanoparticles using thermal decomposition method using the mentioned capping agents, I decided to try to synthesize nanoparticles in the presence of a conductive polymer to possibly enhance the electrical properties of the nanoparticle/polymer interface. This part of my doctoral studies is thoroughly described in the next article.

Based on the article entitled: "The effect of shell modification in iron oxide nanoparticles on electrical conductivity in polythiophene-based nanocomposites"

The next step to obtain materials, which would have desired magnetic and electric properties, was to mix magnetic nanoparticles with an electrically conductive polymer. I chose poly(3-hexylthiophene-2,5-diyl) (P3HT) as it is thoroughly studied and its electrical properties are well-defined [39]. As this polymer has high decomposition temperature I decided to try to synthesize magnetic nanoparticles in the presence of P3HT without any other capping agents to study how different interface influence the properties of nanocomposites. Similar syntheses had been previously conducted so I knew that P3HT can be used in such synthesis [23].

Firstly, I compared morphology, crystallographic structure and magnetic properties of the nanoparticles formed either in the presence of squalene and dodecanoic acid (Fe(Sq)) or P3HT (Fe(P3HT)). For those techniques I was responsible for preparation of the samples and analysis of the results, but the measurements were not conducted by me. As a result, it was shown that nanoparticles are single crystalline with similar diameters (around 10 nm). The characteristic peaks for crystalline P3HT in the diffractogram are visible in both pure polymer sample and Fe(P3HT) which confirms that the polymer is present in the nanoparticles' sample. In case of magnetic properties, Fe(P3HT) has slightly higher saturation magnetization, which is surprising, knowing that the polymer shell may increase the surface spin disorientation, by changing the nanoparticles' surface magnetic anisotropy. The enhancement may be the result of the weak ferromagnetic properties of P3HT, which improved the properties of the magnetic nanoparticle covered with it.

The next step was the analysis of the chemical structure of the nanoparticles with the use of Fourier transform infrared spectroscopy (FT-IR) and XPS. I selected these techniques as they should show whether the thiophane rings from the polymer's structure were altered during the synthesis (for example if they were oxidized) and the XPS would provide me with the chemical structure, hence the type, of iron oxide nanoparticles that

were obtained. The analysis of the FTIR results confirmed the presence of P3HT and iron oxide in the Fe(P3HT). The XPS measurement and analysis I conducted proved that the polymer's structure is not destroyed during the synthesis and, more importantly, the analysis of S2p region indicated that coordinate bonding is created between sulphur from the polymer and iron atoms from the nanoparticle. Additionally, GCIB sputtering was used to unravel the structure of nanoparticles. Similarly to my previous studies, Fe(Sq) nanoparticles were covered shell made of squalene and dodecanoic acid. The thin layer of iron oxide between shell and core, both in Fe(Sq) and Fe(P3HT), was made from either hematite or maghemite. Furthermore, I uncovered the core of the nanoparticles, using GCIB sputtering, and showed that it is made of magnetite.

All of the beforementioned techniques and results showed that the used and modified protocol of nanoparticles' synthesis may be applied to successfully create nanoparticles with the shell of choice. What is more, I did not find any significant differences in both types of nanoparticles, except for the shell - one made of potentially insulating squalene and dodecanoic acid, and the other one made of electrically conductive P3HT. Thus, these nanoparticles are great candidates for the study of electrical properties of materials based on electrically conductive polymer matrix and magnetically responsive filler. This result was important for reaching a final goal of my doctoral studies that was to obtain a magnetoelectrically responsive nanocomposite.

During my research on the conductivity of the nanoparticles, pure Fe(Sq) gave no electrical response, which was somehow surprising since it is well-known that iron oxide nanoparticles are p-type semiconductors [40]. This is possibly a result of carbon shell which insulates the core of nanoparticles. On the other hand, Fe(P3HT) conduct electricity much better than pure thin polymer film. I believe it may be explained by the conductivity of nanoparticles which, when directly connected with the conductive matrix, enhances the conductive properties of P3HT. In the last part of this study, I obtained nanocomposites made of P3HT matrix and 30% weight content of nanoparticles. It allowed me to study the influence of nonconductive filler on the electrical properties of the films. The Fe(Sq) nanoparticles increased the conductivity of polymer, which I was explained by doping of the polymer chain by the dodecanoic acid. Additionally, I checked the influence of light, and the best results gave pristine polymer, showing that my nanocomposites are not suitable if one wants to obtain highly electrically conductive materials in light. However, when used in dark conditions, nanocomposites based on Fe(P3HT) and P3HT conduct electricity 6 times better than the pure polymer. The increase of the conductivity is explained not only by the direct connection between semiconductive nanoparticle and the polymer, but also by the better adjustment of the hole injection barrier, which height was checked by the ultraviolet photoelectron spectroscopy.

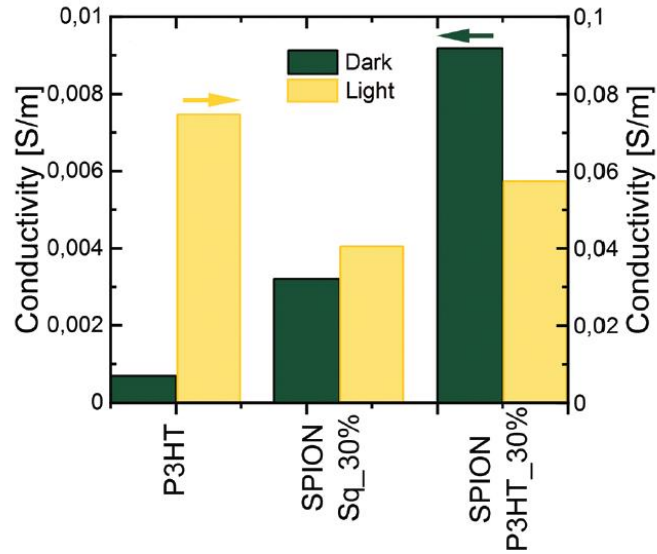


Figure 5. Conductivity values measured for thin films of P3HT, NP(Sq) and NP(P3HT). In dark, nanoparticles covered with squalene do not influence the conductivity of the polymer film, but the nanoparticles synthesized in-situ of the P3HT matrix are improving the conductivity of the material over 9-times [2].

All of these results, show that the obtained materials are good candidates for the electrically conductive hybrid nanomaterials. As the main goals of my doctoral studies were to study the interface between nanoparticle and polymer and to obtain magnetoelectrically responsive hybrid material, I managed to show that even the residual carbon shell may have significant impact on the conductivity of the composite and that iron oxide nanoparticles enhance the transport of electric charge carriers in the material.

Magnetoelectrically responsive nanocomposites based on magnetic nanoparticles

Previous chapters have already proven that magnetite nanoparticles with the conductive shell can be synthesized and that the interface has an impact on the conductivity of polymer-based nanocomposites. As a result, I decided to check the influence of such fillers on the properties of the nanoparticle/polymer nanocomposite. My approach to this subject and the obtained results are the main topic of the last article involved in this dissertation.

Based on the article entitled: "Magnetoresistive Properties of Nanocomposites Based on Ferrite Nanoparticles and Polythiophene"

To understand the influence of the filler and properly characterize nanocomposites, different magnetic nanoparticles were chosen. For the primary filler I selected magnetite, and for two additional, cobalt ferrite and nickel ferrite were used. All three types of nanoparticles were synthesized following the same protocol as in the previous works, with two distinctive shells – insulating and electrically conductive.

To check the morphology of nanoparticles, TEM was used. All NP(Sq) samples had larger diameters and had more regular shapes than their P3HT-coated counterparts. The diameter of magnetite nanoparticles, both Fe(Sq) and Fe(P3HT), was calculated to be around 10 nm, regardless of the shell. The same was observed for nickel ferrite nanoparticles (Ni(Sq) and Ni(P3HT)), but in this case the nanoparticles were two times smaller (diameter equal to 5 nm). It was a surprising result showing that the capping agent used during the synthesis had no influence on the size, but could help to obtain more regular nanoparticles. The second characteristics checked for all samples was the magnetic response. The parameter which was interesting for us, from this analysis point of view, was the samples' M_s , so the VSM method was used. The highest M_s was observed for the magnetite samples, which was almost the same, regardless of the shell. In case of nickel ferrite nanoparticles, the M_s values were small, almost 4 times smaller in comparison to Fe(Sq). This may be the result of the small particle diameter, hence the biggest surface to core volume ratio. In such case, the highest impact of the structural distortions on the overall magnetic response may be observed. The cobalt ferrite nanoparticles with the shell made of polymer (Co(P3HT)) are two times smaller than the nanoparticles formed in the presence of the capping agents (Co(Sq)), which has its reflection in the M_s values. For Co(Sq) saturation is achieved with the two times higher value than for Co(P3HT). Additionally, I compared the measured values of M_s with the bulk values from literature, and found that for all samples the bulk values are higher. These result suggest that the magnetic core of the nanoparticle is covered with a magnetic dead layer, which potentially lowers the magnetic response of the nanoparticles [41].

The next step was to create nanocomposites and determine the electrical response of the nanoparticles. To achieve that I mixed solutions of nanoparticles with P3HT. Secondly, I measured the conductivity of the samples in a wide range of temperatures (200 to 400 K) to determine the conduction mechanism. Based on the results, I concluded that in the nanocomposites we can observe thermally activated conduction mechanism, with the charge carriers hopping or tunneling between nanoparticle and polymer chain. I was not able to measure conductivity of pure P3HT and in the [2] I showed that nanoparticles covered with squalene and dodecanoic acid, cannot conduct electricity. Since all nanocomposites were electrically conductive, we can conclude that nanocomposites based on P3HT and magnetic nanoparticles enhance the electrical properties of a final material. To further study the mechanism, I calculated the disorder ratio, to check how different types of nanoparticles disturbed the polymer chains present in all samples. The NP(Sq) fillers had smaller influence on the samples disorder, which can be explained with the isolated character of the nanoparticles. When it comes to NP(P3HT), the addition of chains from shells, may lead to increased number of distortions and interactions, which results in an increased disorder of the conduction paths. Additionally, better conductivity results should be observed for NP(P3HT) based nanocomposites, since the highly spin polarized charge carriers may be injected to the polymer matrix, without as high barrier as in case of NP(Sq) nanoparticles. This was proven by applying the variable-range hopping model (VRH), which allowed to calculate the Mott temperature, which reflects the disorder of the polymer chain present in the sample (similar to the already calculated disorder ratio). The result for magnetite and cobalt ferrite based samples followed the trend of the VRH function well, which suggested the 3D VRH electrical conduction mechanism. Since, these four types of nanoparticles gave the highest magnetic response, it is possible that the magnetic core of nanoparticles play an important role in the stabilization of spins of charge carriers, which leads to lowering the probability of scattering.

In the last part of this study, I focused on the electrical properties of the formed materials, but in the external magnetic field. The conductivity of nanocomposites was measured in the external magnetic field with varying strength of up to 1500 mT. The nickel based nanoparticles showed no change of conductivity with the increase of magnetic field. These samples showed the weakest response to the magnetic field in the VSM measurement and followed the VRH model with poor results, with no change in the conductivity, even in the high magnetic field, as it was anticipated. On the other hand, four remaining nanocomposites, showed good response. The increase of the conductivity in the external magnetic field was observed - from 1%, for Fe(Sq) based nanocomposite, to 5.5%, for Fe(P3HT) based nanocomposite at 200 K. For the Co(Sq) to Co(P3HT) based nanocomposites the observed increase was from 2.5 % to 4.5 % at 200 K (Figure 6). Better results for NP(P3HT) based samples, might be explained by the forward interference

model proposed by Nguyen, Spivan and Shlovskii [42]. It discusses the conductivity of a system by the sum of all possible paths that the charge carrier may use. If the NP(P3HT) acts as a filler, the carriers from nanoparticles bring high added value, but if the NP(Sq) are used, they act like insulated elements, hence are not adding much to the overall performance of the material.

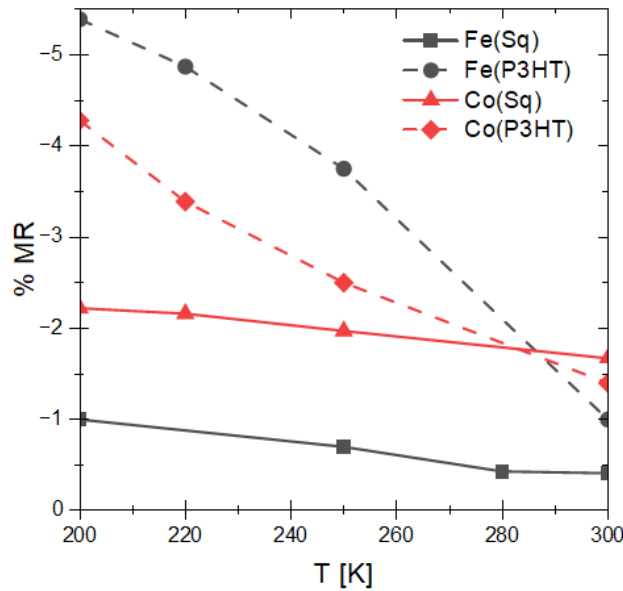


Figure 6. The graph shows the summary of change in magnetoresistance values in external magnetic field of 1500 mT for all measured samples in different temperatures [4].

To sum up these findings, nanoparticles acting as a filler can be a simple solution to enhance the electric properties of the polymer based materials. In addition, the magnetic response can be achieved which opens many potential applications for relatively easy obtainable nanocomposite. Moreover, the performed studies showed that the interface play a pivotal role in the conductivity and magnetoelectric response of materials based on more than one component.

Summary

In this study, I showed a comprehensive approach that may be taken to design and create nanocomposites based on nanoparticles and conjugated polymers. This study brings new approaches to obtain materials with well-described interactions between filler and matrix and a good understanding of the consequences of choosing the nanocomposite's components.

Firstly, I proposed a synthesis of magnetite and zinc ferrites, with varying substitution amounts, in the presence of capping agents. This allowed me to study the influence of a feed composition and synthetic conditions on the size, and magnetic properties of final products. Additionally, I realized that the carbon shell is unavoidable, and its thickness may result in the electric insulation of single nanoparticles.

Next, I performed a thorough analysis of Fe2p XPS spectra of magnetite and three different ferrites, to enrich my characterization protocol and understanding of the dopant distribution in different nanoparticles. What is more, the study proved the negative impact of often-used monoatomic sputtering on the structure of studied material. As an alternative, I proposed a nondestructive procedure for the XPS measurements performed with a use of GCIB sputtering, which allows a reliable study of subsequent layers of materials covering metal oxide nanoparticles.

The second part of my dissertation was more focused on the creation of an electrically responsive nanocomposite. An alternative approach to the synthesis of nanoparticles was proposed – in the presence of polymer instead of capping agents. This way I could create nanoparticles, which could have a direct connection to the polymer matrix without the insulating barrier made of capping agents. Both types of nanoparticles were thoroughly studied to establish differences in morphology and magnetic response, and the interactions between nanoparticles and conjugated polymer were proved. The electric characterization showed that nanoparticles synthesized in the presence of capping agents are insulators, but mixing with conductive polymer can enhance the properties of such a system. On the other hand, nanoparticles created directly in the polymer matrix showed very good electrical properties even without the addition of polymer post-synthesis.

The last part of my doctoral thesis showed an easy way to create an electromagnetically responsive nanocomposite based on conjugated polymer and magnetic nanoparticles. The study confirmed, that the used filler and its properties greatly influence the characteristics of a final material. In the analyzed system it was possible to enhance the conductivity of material by 5 times, just by altering the shell of nanoparticles, which shows and proves that the interface plays an important role in materials based on more than one component.

The main goal of my thesis was to create a hybrid material and analyze the role of an interface in the systems based on nanoparticles and conjugated polymers. All of the results presented above confirm the importance of the interface between a magnetic core of a filler and a polymer. What is equally important, they show successful synthesis of different magneto-responsive hybrid systems, which fulfills the assumptions made at the beginning of my doctoral studies and this thesis.

Bibliography

1. Lachowicz, D.; Wirecka, R.; Górka-Kumik, W.; Marzec, M.M.; Gajewska, M.; Kmita, A.; Żukrowski, J.; Sikora, M.; Zapotoczny, S.; Bernasik, A. Gradient of Zinc Content in Core-Shell Zinc Ferrite Nanoparticles-Precise Study on Composition and Magnetic Properties. *Phys. Chem. Chem. Phys.* **2019**, *21*, 23473–23484, doi:10.1039/c9cp03591e.
2. Wirecka, R.; Marzec, M.M.; Marciszko-Wiąckowska, M.; Lis, M.; Gajewska, M.; Trynkiewicz, E.; Lachowicz, D.; Bernasik, A. The Effect of Shell Modification in Iron Oxide Nanoparticles on Electrical Conductivity in Polythiophene-Based Nanocomposites. *J. Mater. Chem. C* **2021**, *9*, 10453–10461, doi:10.1039/D1TC02949E.
3. Wirecka, R.; Lachowicz, D.; Berent, K.; Marzec, M.M.; Bernasik, A. Ion Distribution in Iron Oxide, Zinc and Manganese Ferrite Nanoparticles Studied by XPS Combined with Argon Gas Cluster Ion Beam Sputtering. *Surfaces and Interfaces* **2022**, *30*, doi:10.1016/j.surfin.2022.101865.
4. Wirecka, R.; Maćkosz, K.; Żywczak, A.; Marzec, M.M.; Zapotoczny, S.; Bernasik, A. Magnetoresistive Properties of Nanocomposites Based on Ferrite Nanoparticles and Polythiophene. *Nanomaterials* **2023**, *13*, doi:10.3390/nano13050879.
5. Muro-Cruces, J.; Roca, A.G.; López-Ortega, A.; Fantechi, E.; Del-Pozo-Bueno, D.; Estradé, S.; Peiró, F.; Sepúlveda, B.; Pineider, F.; Sangregorio, C.; et al. Precise Size Control of the Growth of Fe₃O₄ Nanocubes over a Wide Size Range Using a Rationally Designed One-Pot Synthesis. *ACS Nano* **2019**, doi:10.1021/acsnano.9b01281.
6. Laurent, S.; Forge, D.; Port, M.; Roch, A.; Robic, C.; Vander Elst, L.; Muller, R.N. Magnetic Iron Oxide Nanoparticles: Synthesis, Stabilization, Vectorization, Physicochemical Characterizations and Biological Applications. *Chem. Rev.* **2008**, *108*, 2064–2110, doi:10.1021/CR068445E/ASSET/CR068445E.FP.PNG_V03.
7. Besenhard, M.O.; LaGrow, A.P.; Hodzic, A.; Kriechbaum, M.; Panariello, L.; Bais, G.; Loizou, K.; Damilos, S.; Margarida Cruz, M.; Thanh, N.T.K.; et al. Co-Precipitation Synthesis of Stable Iron Oxide Nanoparticles with NaOH: New Insights and Continuous Production via Flow Chemistry. *Chem. Eng. J.* **2020**, *399*, 125740, doi:10.1016/J.CEJ.2020.125740.
8. Lachowicz, D.; Kaczyńska, A.; Wirecka, R.; Kmita, A.; Szczerba, W.; Bodzoń-Kulakowska, A.; Sikora, M.; Karewicz, A.; Zapotoczny, S. A Hybrid System for Magnetic Hyperthermia and Drug Delivery: SPION Functionalized by Curcumin Conjugate. *Mater.* **2018**, *Vol. 11*, Page 2388 **2018**, *11*, 2388, doi:10.3390/MA11122388.
9. Wang, X.; Tilley, R.D.; Watkins, J.J. Simple Ligand Exchange Reactions Enabling Excellent Dispersibility and Stability of Magnetic Nanoparticles in Polar Organic, Aromatic, and Protic Solvents. *Langmuir* **2014**, *30*, 1514–1521, doi:10.1021/LA404757Q/SUPPL_FILE/LA404757Q_SI_001.PDF.
10. Ramimoghadam, D.; Bagheri, S.; Hamid, S.B.A. Progress in Electrochemical Synthesis of Magnetic Iron Oxide Nanoparticles. *J. Magn. Magn. Mater.* **2014**, *368*,

- 207–229, doi:10.1016/j.jmmm.2014.05.015.
11. Lassenberger, A.; Grü Newald, T.A.; Van Oostrum, P.D.J.; Rennhofer, H.; Amenitsch, H.; Zirbs, R.; Lichtenegger, H.C.; Reimhult, E. Monodisperse Iron Oxide Nanoparticles by Thermal Decomposition: Elucidating Particle Formation by Second-Resolved in Situ Small-Angle X-Ray Scattering. **2017**, doi:10.1021/acs.chemmater.7b01207.
 12. Qiao, L.; Fu, Z.; Li, J.; Ghosen, J.; Zeng, M.; Stebbins, J.; Prasad, P.N.; Swihart, M.T. Standardizing Size-and Shape-Controlled Synthesis of Monodisperse Magnetite (Fe₃O₄) Nanocrystals by Identifying and Exploiting Effects of Organic Impurities. **2017**, doi:10.1021/acsnano.7b02752.
 13. Wilson, D.; Langell, M.A. XPS Analysis of Oleylamine/Oleic Acid Capped Fe₃O₄ Nanoparticles as a Function of Temperature. *Appl. Surf. Sci.* **2014**, *303*, 6–13, doi:10.1016/j.apsusc.2014.02.006.
 14. Munoz-Bonilla, A.; Sanchez-Marcos, J.; Herrasti, P. *Conducting Polymer Hybrids*; Kumar, V., Kalia, S., Swart, H., Eds.; Springer, 2017; ISBN 978-3-319-46456-5.
 15. Zhang, W.; Xu, Y.; Wang, H.; Xu, C.; Yang, S. Fe₃O₄ Nanoparticles Induced Magnetic Field Effect on Efficiency Enhancement of P3HT:PCBM Bulk Heterojunction Polymer Solar Cells. *Sol. Energy Mater. Sol. Cells* **2011**, *95*, 2880–2885, doi:10.1016/j.solmat.2011.06.005.
 16. Wang, K.; Yi, C.; Liu, C.; Hu, X.; Chuang, S.; Gong, X. Effects of Magnetic Nanoparticles and External Magnetostatic Field on the Bulk Heterojunction Polymer Solar Cells. *Sci. Rep.* **2015**, *5*, 9265, doi:10.1038/srep09265.
 17. Benchaabane, A.; Ben Hamed, Z.; Telfah, A.; Abderrahmane Sanhoury, M.; Kouki, F.; Zellama, K.; Bouchriha, H. Effect of OA-ZnSe Nanoparticles Incorporation on the Performance of PVK Organic Photovoltaic Cells. *Mater. Sci. Semicond. Process.* **2017**, *64*, 115–123, doi:10.1016/j.mssp.2017.03.018.
 18. Chen, S.H.; Souna, A.J.; Stranick, S.J.; Jhalaria, M.; Kumar, S.K.; Soles, C.L.; Chan, E.P. Controlling Toughness of Polymer-Grafted Nanoparticle Composites for Impact Mitigation †. *This J. is Cite this Soft Matter* **2022**, *18*, 256, doi:10.1039/d1sm01432c.
 19. Bilchak, C.R.; Buenning, E.; Asai, M.; Zhang, K.; Durning, C.J.; Kumar, S.K.; Huang, Y.; Benicewicz, B.C.; Gidley, D.W.; Cheng, S.; et al. Polymer-Grafted Nanoparticle Membranes with Controllable Free Volume. *Macromolecules* **2017**, *50*, 7111–7120, doi:10.1021/ACS.MACROMOL.7B01428/SUPPL_FILE/MA7B01428_SI_001.PDF.
 20. Khan, J.; Harton, S.E.; Akcora, P.; Benicewicz, B.C.; Kumar, S.K. Polymer Crystallization in Nanocomposites: Spatial Reorganization of Nanoparticles. *Macromolecules* **2009**, *42*, 5741–5744, doi:10.1021/MA900794T/ASSET/IMAGES/MEDIUM/MA-2009-00794T_0005.GIF.
 21. Jimenez, A.M.; Krauskopf, A.A.; Pérez-Camargo, R.A.; Zhao, D.; Pribyl, J.; Jestin, J.; Benicewicz, B.C.; Müller, A.J.; Kumar, S.K. Effects of Hairy Nanoparticles on Polymer Crystallization Kinetics. *Macromolecules* **2019**, *52*, 9186–9198, doi:10.1021/ACS.MACROMOL.9B01380/SUPPL_FILE/MA9B01380_SI_001.PDF.

22. Liang, Y.N.; Yu, K.; Yan, Q.; Hu, X. Colloidal CuInSe₂ Nanocrystals: From Gradient Stoichiometry toward Homogeneous Alloyed Structure Mediated by Conducting Polymer P3HT. *ACS Appl. Mater. Interfaces* **2013**, *5*, 4100–4106, doi:10.1021/am3032212.
23. Dayal, S.; Kopidakis, N.; Olson, D.C.; Ginley, D.S.; Rumbles, G. Direct Synthesis of CdSe Nanoparticles in Poly(3-Hexylthiophene). *J. Am. Chem. Soc.* **2009**, *131*, 17726–17727, doi:10.1021/ja9067673.
24. Jacobo, S.E.; Apesteguy, J.C.; Lopez Anton, R.; Schegoleva, N.N.; Kurlyandskaya, G. V. Influence of the Preparation Procedure on the Properties of Polyaniline Based Magnetic Composites. *Eur. Polym. J.* **2007**, *43*, 1333–1346, doi:10.1016/j.eurpolymj.2007.01.024.
25. Sun, H.Z.; Yang, B. In Situ Preparation of Nanoparticles/Polymer Composites. *Sci. China, Ser. E Technol. Sci.* **2008**, *51*, 1886–1901, doi:10.1007/s11431-008-0109-6.
26. Fahlman, M.; Fabiano, S.; Gueskine, V.; Simon, D.; Berggren, M.; Crispin, X. Interfaces in Organic Electronics. *Nat. Rev. Mater.* **2019**, *4*, 627–650, doi:10.1038/s41578-019-0127-y.
27. Zacher, B.; Gantz, J.L.; Richards, R.E.; Armstrong, N.R. Organic Solar Cells - At the Interface. *J. Phys. Chem. Lett.* **2013**, *4*, 1949–1952, doi:10.1021/JZ4009932/ASSET/IMAGES/LARGE/JZ-2013-009932_0001.JPEG.
28. Graetzel, M.; Janssen, R.A.J.; Mitzi, D.B.; Sargent, E.H. Materials Interface Engineering for Solution-Processed Photovoltaics. *Nature* **2012**, *488*, 304–312, doi:10.1038/nature11476.
29. Zhao, H.; Wang, Y.; Bao, L.; Chen, C. Engineering Nano-Bio Interfaces from Nanomaterials to Nanomedicines. *Accounts Mater. Res.* **2022**, *3*, 812–829, doi:10.1021/ACCOUNTSMR.2C00072/ASSET/IMAGES/MEDIUM/MR2C00072_0010.GIF.
30. Baskakov, A.O.; Solov'eva, A.Y.; Ioni, Y. V.; Starchikov, S.S.; Lyubutin, I.S.; Khodos, I.I.; Avilov, A.S.; Gubin, S.P. Magnetic and Interface Properties of the Core-Shell Fe₃O₄/Au Nanocomposites. *Appl. Surf. Sci.* **2017**, *422*, 638–644, doi:10.1016/j.apsusc.2017.06.029.
31. Mutiso, R.M.; Winey, K.I. *7.17 - Electrical Conductivity of Polymer Nanocomposites*; Elsevier B.V., 2012; Vol. 7; ISBN 9780080878621.
32. Fratini, S.; Nikolka, M.; Salleo, A.; Schweicher, G.; Sirringhaus, H. Charge Transport in High-Mobility Conjugated Polymers and Molecular Semiconductors. *Nat. Mater.* **2020**, *19*, 491–502, doi:10.1038/s41563-020-0647-2.
33. Gu, H.; Guo, J.; Yan, X.; Wei, H.; Zhang, X.; Liu, J.; Huang, Y.; Wei, S.; Guo, Z. Electrical Transport and Magnetoresistance in Advanced Polyaniline Nanostructures and Nanocomposites. *Polymer (Guildf)*. **2014**, *55*, 4405–4419, doi:10.1016/j.polymer.2014.05.024.
34. Liu, C.; Huang, K.; Park, W.T.; Li, M.; Yang, T.; Liu, X.; Liang, L.; Minari, T.; Noh, Y.Y. A Unified Understanding of Charge Transport in Organic Semiconductors: The Importance of Attenuated Delocalization for the Carriers. *Mater. Horizons* **2017**, *4*,

608–618, doi:10.1039/c7mh00091j.

35. Guo, J.; Chen, Z.; Abdul, W.; Kong, J.; Khan, M.A.; Young, D.P.; Zhu, J.; Guo, Z. Tunable Positive Magnetoresistance of Magnetic Polyaniline Nanocomposites. *Adv. Compos. Hybrid Mater.* **2021**, *4*, 534–542, doi:10.1007/s42114-021-00242-z.
36. Xu, H.; Wang, M.; Yu, Z.G.; Wang, K.; Hu, B. Magnetic Field Effects on Excited States, Charge Transport, and Electrical Polarization in Organic Semiconductors in Spin and Orbital Regimes. *Adv. Phys.* **2019**, *68*, 49–121, doi:10.1080/00018732.2019.1590295.
37. Gu, H.; Zhang, X.; Wei, H.; Huang, Y.; Wei, S.; Guo, Z. An Overview of the Magnetoresistance Phenomenon in Molecular Systems. *Chem. Soc. Rev.* **2013**, *42*, 5907–5943, doi:10.1039/c3cs60074b.
38. Ding, S.; Tian, Y.; Hu, W. Cornerstone of Molecular Spintronics: Strategies for Reliable Organic Spin Valves. *Nano Res.* **2021**, *14*, 3653–3668, doi:10.1007/S12274-021-3310-6.
39. Obrzut, J.; Page, K.A. Electrical Conductivity and Relaxation in Poly(3-Hexylthiophene). *Phys. Rev. B - Condens. Matter Mater. Phys.* **2009**, *80*, 1–7, doi:10.1103/PhysRevB.80.195211.
40. Cornell, R.M.; Schwertmann, U. *The Iron Oxides: Structure, Properties, Reactions, Occurrences, and Uses*; Wiley-VCH, 1996; ISBN 9783527285761.
41. Geng, R.; Luong, H.M.; Pham, M.T.; Das, R.; Stojak Repa, K.; Robles-Garcia, J.; Duong, T.A.; Pham, H.T.; Au, T.H.; Lai, N.D.; et al. Magnetically Tunable Organic Semiconductors with Superparamagnetic Nanoparticles. *Mater. Horizons* **2019**, *6*, 1913–1922, doi:10.1039/c9mh00265k.
42. Nguen, V.L.; Spivak, B.Z.; Shklovskii, B.I. Tunnel Hopping in Disordered Systems. *JETP lett* **1985**, *62*, 1021–1026.

Abbreviations

Co(Sq) – cobalt ferrite nanoparticles synthesized in the presence of capping agents

Co(P3HT) – cobalt ferrite nanoparticles synthesized in the presence of P3HT

FT-IR – Fourier transform infrared spectroscopy

Fe(Sq) – iron oxide nanoparticles synthesized in the presence of capping agents

Fe(P3HT) – iron oxide nanoparticles synthesized in the presence of P3HT

FWHM – full width at half maximum

GCIB – Gas Cluster Ion Beam

ICP-OES – Inductively coupled plasma optical emission spectroscopy.

MFE – Magnetic Field Effects

Mn(Sq) – manganese ferrite nanoparticles synthesized in the presence of capping agents

MnZn(Sq) – zinc manganese ferrite nanoparticles synthesized in the presence of capping agents

MS – Mössbauer spectroscopy

M_s – saturation magnetization

NP(Sq) – magnetic nanoparticles synthesized in the presence of squalene and dodecanoic acid

NP(P3HT) – magnetic nanoparticles synthesized in the presence of P3HT

OPVs – organic photovoltaics

P3HT – poly(3-hexylthiophene-2,5-diyl)

TEM – transmission electron microscopy

TGA – Thermogravimetric analysis

VSM – Vibrating Sample Magnetometry

XPS – X-ray photoelectron spectroscopy

Zn(Sq) – zinc ferrite nanoparticles synthesized in the presence of squalene and dodecanoic acid

My articles and conferences

Articles

1. Lachowicz D., Kaczyńska A., **Wirecka R.**, Kmita A., Szczerba W., Bodzoń – Kułakowska A., Sikora M., Karewicz A., Zapotoczny S., „A hybrid system for magnetic hyperthermia and drug delivery: SPION functionalized by curcumin conjugate”, *Materials*, 2018, 11(12), 2388, doi: 10.3390/ma11122388
2. Lachowicz D., Mielczarek P., **Wirecka R.**, Berent K., Karewicz A., Szuwarzyński M., Zapotoczny S., „Nanohydrogels Based on Self-Assembly of Cationic Pullulan and Anionic Dextran Derivatives for Efficient Delivery of Piroxicam”, *Pharmaceutics*, 2019, 11(12), 622, doi: 10.3390/pharmaceutics11120622
3. Lachowicz D., **Wirecka R.**, Górka – Kumik W., Marzec M.M., Gajewska M., Kmita A., Żukrowski J., Sikora M., Zapotoczny S., Bernasik A., „Gradient of zinc content in core-shell zinc ferrite nanoparticles – precise study on composition and magnetic properties”, *Phys. Chem. Chem. Phys.*, 2019, 21(42), 23473-23484, doi: 10.1039/C9CP03591E
4. Palumbo G., Kollbek K., **Wirecka R.**, Bernasik A., Górny M., „Effect of CO₂ partial pressure on the corrosion inhibition of N80 carbon steel by gum arabic in a CO₂-water saline environment for shale oil and gas industry”, *Materials*, 1-24, doi: 10.3390/ma13194245
5. Lachowicz D., Kaczyńska A.; Bodzoń-Kulakowska A., Karewicz A., **Wirecka R.**, Szuwarzyński M., Zapotoczny S., „Coacervate Thermoresponsive Polysaccharide Nanoparticles as Delivery System for Piroxicam”, *Int. J. Mol. Sci.*, 2020, 21(24), 9664; doi: 10.3390/ijms21249664
6. Palumbo G., Dunikowski D., **Wirecka R.**, Mazur T., Lelek-Borkowska U., Wawer K., Banaś J., „Effect of Grain Size on the Corrosion Behavior of Fe-3wt.%Si-1wt.%Al Electrical Steels in Pure Water Saturated with CO₂”, *Materials*, 2021, 14(17), 5084, doi: 10.3390/ma14175084
7. **Wirecka R.**, Marzec M.M., Marciszko-Wiąckowska M., Lis M., Gajewska M., Trynkiewicz E., Lachowicz D., Bernasik A., „The effect of shell modification in iron oxide nanoparticles on electrical conductivity in polythiophene-based nanocomposites”, *J. Mater. Chem. C*, 2021, 9(32), 10453-10461, doi: 10.1039/D1TC02949E
8. **Wirecka R.**, Lachowicz D., Berent K., Marzec M.M., Bernasik A., „Ion distribution in iron oxide, zinc and manganese ferrite nanoparticles studied by XPS combined with argon gas cluster ion beam sputtering”, *Surf. Interfaces*, 2022, 30, 101865 doi: 10.1016/j.surfin.2022.101865

9. **Wirecka R.**, Maćkosz K., Żywczak A., Marzec M.M., Zapotoczny S., Bernasik A., „Magnetoresistive Properties of Nanocomposites Based on Ferrite Nanoparticles and Polythiophene”, *Nanomaterials*, 2023, 13(5), 879, doi: 10.3390/nano13050879
10. Lachowicz D., Kmita A., **Wirecka R.**, Berent K., Szuwarzyński M., Zapotoczny S., Pajdak A., Cios G., Mazur-Panasiuk N., Pyrc K., Bernasik A., „Aerogels based on cationically modified chitosan and poly(vinyl alcohol) for efficient capturing of viruses”, *Carbohydr. Polym.*, 2023, 312, 120756, doi: 10.1016/j.carbpol.2023.120756

Conferences

1. 11th International Conference on Nanophotonics, Wrocław, Poland, „Zn_xFe_{3-x}O₄ nanoparticles characterization by X-ray Photoelectron Spectroscopy coupled with Gas Cluster Ion Beam” – Poster
2. ANM 2019 : 14th International conference on Advanced Nanomaterials, Aveiro, Portugal, „Ferrite nanoparticles characterization by X-ray Photoelectron Spectroscopy coupled with Gas Cluster Ion Beam” – Oral presentation
3. 6th Nano Today Conference, Lisbon, Portugal, „Synthesis and characterization of magnetic nanoparticles embedded in poly(3-hexylthiophene-2,5-diyl) for photovoltaic applications” – Oral presentation
4. 45 Zjazd Fizyków Polskich, Kraków, Poland, „Charakterystyka fizykochemiczna nanocząstek magnetycznych w przewodzącej otoczce do zastosowań w elektronice organicznej” - Poster
5. 14th International Symposium on Flexible Organic Electronics, Thessaloniki, Greece, „Modification of nanoparticles' shell as a way to enhance electrical properties of iron oxide/polythiophene based hybrid material” – Oral presentation

Reprints of publications and Statements of Authors contribution



Cite this: *Phys. Chem. Chem. Phys.*,
2019, 21, 23473

Gradient of zinc content in core–shell zinc ferrite nanoparticles – precise study on composition and magnetic properties†

Dorota Lachowicz,[‡] Roma Wirecka,[‡] Weronika Górka-Kumik,[‡] Mateusz Marek Marzec,^a Marta Gajewska,^a Angelika Kmita,^a Jan Żukrowski,^a Marcin Sikora,^a Szczepan Zapotoczny^d and Andrzej Bernasik^{*,b}

A broad spectrum of applications of magnetic nanoparticles leads to the need for the precise tuning of their magnetic properties. In this study, a series of magnetite and zinc-ferrite nanoparticles were successfully prepared by modified high-temperature synthesis in a controlled gas atmosphere. Nanoparticles with different zinc to iron ratios and pure Fe₃O₄ were obtained. The structure of the nanoparticles was studied by transmission electron microscopy and Mössbauer spectroscopy. These revealed the single domain character of the nanoparticles and the influence of the synthesis temperature and zinc to iron ratio on their shape and size. Chemical structure was characterized by inductively coupled plasma optical emission spectroscopy, energy dispersive X-ray spectroscopy and thermogravimetric analysis. X-ray photoelectron spectroscopy coupled with an argon gas cluster ion beam (Ar-GCIB) allowed the study of subsequent layers of the nanoparticles without altering their chemical structure. This revealed the presence of a carbon layer on all nanoparticles consisting of capping agents used in the synthesis and revealed the core–shell character of the zinc ferrite particles. In addition, different types of zinc infusions in the nanoparticle structure were observed when using different Zn/Fe ratios. Finally, magnetic studies performed by means of vibrating sample magnetometry proved the superparamagnetic behavior of all the samples.

Received 26th June 2019,
Accepted 27th September 2019

DOI: 10.1039/c9cp03591e

rsc.li/pccp

Introduction

Magnetic nanoparticles with characteristic properties can be used in many applications, such as catalysis,¹ electronics² and medicine.³ Control over the size, morphology and surface treatment of these nanoparticles makes it possible to broaden their applicability in many areas. The controlled properties of magnetic nanoparticles make them a promising candidate as a component of new hybrid materials for future magnetic sensors or solar cell applications.^{4–7}

Among the many magnetic particles containing iron, one of the largest groups are iron oxides. The most common of these

are: hematite (α -Fe₂O₃), maghemite (γ -Fe₂O₃) and magnetite (Fe₃O₄).^{8–10} Presently, studies on iron oxide-based magnetic nanoparticles are focused on the development of new methods for their synthesis and surface modification.^{8,11–14} The main problem is obtaining monodispersed objects of a certain size and shape in a repeatable process. Unfortunately, typical methods of synthesis require a purification step such as magnetic filtration or size exclusion. Currently, a lot of magnetic nanoparticle synthesis methods have been described, *e.g.* sonochemical reactions,¹⁵ thermal decomposition reactions,^{16,17} hydrolysis, sol–gel, microemulsions and co-precipitation techniques.^{18–20} However, control over the size, shape and magnetic properties of nanoparticles during these processes still remains a challenge.

The size of the nanoparticles has a decisive impact on their magnetic properties. When magnetite nanoparticles (Fe₃O₄) are smaller than 20–30 nm, they exhibit exceptional magnetic behavior called superparamagnetism.^{21–23} This phenomenon is characterized by two properties: nanoparticles exhibit no hysteresis loop, and hence the coercivity equals zero; and secondly, when magnetization (M) dependencies are measured at different temperatures (T), such plots should overlap when M is normalized to T .²⁴ Magnetic properties of magnetite nanoparticles can be tuned by:

^a AGH University of Science and Technology, Academic Centre for Materials and Nanotechnology, al. A. Mickiewicza 30, 30-059 Krakow, Poland.
E-mail: bernasik@agh.edu.pl

^b AGH University of Science and Technology, Faculty of Physics and Applied Computer Science, al. A. Mickiewicza 30, 30-059 Krakow, Poland

^c Faculty of Physics, Astronomy and Applied Computer Science, Jagiellonian University, Prof. Stanisława Łojasiewicza 11, 30-348 Krakow, Poland

^d Faculty of Chemistry, Jagiellonian University, Gronostajowa 2, 30-387 Krakow, Poland

† Electronic supplementary information (ESI) available. See DOI: 10.1039/c9cp03591e

‡ These authors equally contributed to the manuscript.

- partial substitution of iron ions with zinc,²⁵ barium,²⁶ manganese or cobalt,²⁷ for example
- adding “capping” agents to the synthesis, which, by influencing the boiling point of the reaction mixture, can limit the growth of the nanoparticles during their synthesis;^{17,28} (this allows us to obtain nanoparticles of desired shapes and sizes, and hence adjust the magnetic properties²⁹);
- synthesis of core-shell nanoparticles, instead of homogeneous particles.³⁰

Additionally, a high surface-to-volume ratio permits their functionalization which, with the tuning of magnetic properties, results in potential uses of the final product in many fields, such as: hyperthermia,³¹ organic photovoltaics,^{32,33} drug delivery systems,³⁴ ferrofluids³⁵ and as a promising anode material for lithium-ion batteries.³⁶

$Zn_xFe_{3-x}O_4$ belongs to the spinel ferrite family in which O^{2-} ions create a face-centered cubic lattice. In this structure, metal ions are equally divided into three groups: Fe^{2+} in an octahedral structure (B-sites), Fe^{3+} in an octahedral structure (B-sites) and Fe^{3+} with Zn^{2+} in tetrahedral interstices (A-site).²⁵ Although Fe_3O_4 crystallizes in an inverse spinel structure, it is believed that even a small addition of zinc changes its structure to normal spinel.³⁷ Because structure has a big impact on the magnetic properties of nanoparticles, the transition from inverse to normal spinel leads to a change in magnetic properties, such as magnetic saturation, which is of great importance in the field of biology.³⁸

In the present paper, we have studied the structural and magnetic properties of magnetite and zinc ferrite nanoparticles with two different degrees of Fe substitution. Synthesis under precisely controlled conditions allows us to obtain nanoparticles with a well-defined size and shape. In recent years, there has been increased interest in the synthesis of mono-dispersed nanocrystals with controllable sizes and well-known structure. While indeed there are a number of ways to obtain iron oxide nanoparticles, each of them has its particular advantages and disadvantages. Up to now, various synthetic protocols for obtaining iron oxide nanoparticles, based on a thermal decomposition method, have been proposed. Among these is a method using surfactants – dodecanoic acid³⁹ and squalene.⁴⁰ In this work, we focused on the synthesis of zinc ferrite nanoparticles and on how the presence of squalene and dodecanoic acid affects the incorporation of zinc ions into the spinel structure. In previous work on the synthesis of nanoparticles of non-stoichiometric zinc ferrite by a thermal decomposition method, the usually used surfactant was oleic acid.⁴¹ No effect of oleic acid was observed on the formation of core-shell zinc ferrite nanoparticles.

For structural characterization, X-ray photoelectron spectroscopy with an argon gun cluster ion beam (Ar-GCIB) was used. Sputtering with Ar-GCIB allowed the investigation of changes in the Zn/Fe ratio in subsequent layers of nanoparticles. The layer structures of the nanoparticles had a significant impact on their magnetic properties, which were studied using vibrating sample magnetometry and Mössbauer spectroscopy. Magnetic properties of the doped and undoped nanoparticles are discussed. Finally, depending on the Zn concentration and size of the nanoparticles, core-shell models have been proposed.

Experimental

Materials

$Fe(acac)_3$ (acac = acetylacetonate) (97%), $Zn(acac)_2$ ($\geq 95\%$), dibenzyl ether ($\geq 98\%$), squalane ($\geq 95\%$) and dodecanoic acid ($\geq 98\%$) were purchased from Sigma Aldrich. All reagents were used as received.

Synthesis of magnetite nanoparticles

Magnetite nanoparticles were synthesized using a modified thermal decomposition method in a controlled gas atmosphere.^{42,43} In the Fe_3O_4 synthesis (S0) 176.5 mg (0.5 mmol) of $Fe(acac)_3$ and 520.0 mg (3 mmol) of dodecanoic acid were mixed with the addition of 7.5 ml of dibenzyl ether and 5 ml of squalane. To obtain nanoparticles of the desired chemical composition, the whole synthesis was carried out in a controlled argon atmosphere. The synthesis consisted of three temperature regimes. First, the flask was heated to 80 °C and kept at this temperature for 90 minutes to provide good dissolution of all ingredients and full degassing of the mixture. Then, the mixture was heated to 200 °C and kept for 90 minutes at this temperature, and finally the suspension was heated to 280 °C and kept for 60 minutes at this temperature. After cooling to room temperature, the mixture was washed with acetone and centrifuged. The supernatant was disposed of and replaced with pure acetone. This procedure was carried out 3 times. The final washing was performed with chloroform, in which the nanoparticles were finally suspended.

Synthesis of zinc ferrite nanoparticles

Three different types of zinc ferrite nanoparticles were synthesized using a modified thermal decomposition method in a controlled gas atmosphere. In the first synthesis (S1) 141.0 mg (0.4 mmol) of $Fe(acac)_3$, 26.5 mg (0.1 mmol) of $Zn(acac)_2$ and 520.0 mg (3 mmol) of dodecanoic acid were mixed with the addition of 7.5 ml of dibenzyl ether and 5 ml of squalane. To obtain nanoparticles of the desired chemical composition, the whole synthesis was carried out in a controlled argon atmosphere. The synthesis consisted of three temperature regimes. First, the flask was heated to 80 °C and kept for 90 minutes at this temperature to provide good dissolution of all ingredients and full degassing of the mixture. Then, the mixture was heated to 200 °C and kept for 90 minutes at this temperature, and lastly the suspension was heated to 280 °C and kept for 60 minutes at this temperature. After cooling down to room temperature, the mixture was washed with acetone and centrifuged. The supernatant was disposed of and replaced with pure acetone. The procedure was carried out 3 times. The last washing was performed with chloroform in which the nanoparticles were finally suspended.

In the second synthesis (S2), the amount of all substrates was doubled and a bigger flask was used to achieve better temperature distribution in the mixture. This also allowed us to increase the final temperature to 290 °C. In the final synthesis (S3) 213.7 mg (0.6 mmol) of $Fe(acac)_3$, 105.4 mg (0.4 mmol) of $Zn(acac)_2$ and 1040 mg (6 mmol) of dodecanoic acid were mixed with the addition of 15 ml of dibenzyl ether and 10 ml of squalane.

The mixture was heated and cleaned in the same manner as in the S1 synthesis.

Characterization methods

Transmission electron microscopy. The morphology, size distribution and average particle size were measured using micrographs from TEM Tecnai TF 20 X-TWIN (FEI). TEM and HR-TEM pictures were analyzed using Image-J software. Additionally, chemical composition was examined using energy dispersive X-ray spectroscopy (EDX).

Inductively coupled plasma optical emission spectroscopy. The chemical composition of the precipitated materials was analyzed with inductively coupled plasma optical emission spectroscopy (ICP-OES) using a Thermo Scientific iCAP 7000 Plus. All samples were dissolved in a mixture of hydrochloric acid and nitric acid.

Magnetometry. The volume magnetic properties of the nanoparticles were probed using a vibrating sample magnetometer (VSM) LakeShore type 7407. Magnetization profiles (hysteresis curves) were measured at selected temperatures using magnetic flux up to 10 kOe. These provided a fingerprint of superparamagnetic behavior and allowed us to determine loop opening characterized by a coercive field, H_C . In addition, the temperature dependence of DC magnetic susceptibility was measured under a steady magnetic flux of 100 Oe during sample heating, preceded by zero field cooling (ZFC). These provided a fingerprint of the blocking temperature evolution, which is expected to follow a similar trend to the characteristic temperature corresponding to maxima of the susceptibility curve, T_{max} .

Mössbauer spectroscopy. The ^{57}Fe Mössbauer absorption spectra were measured at room temperature ($T = 300\text{ K}$) and at cryogenic temperatures ($T = 80\text{ K}$) utilizing a ^{57}Co source in an Rh matrix. A spectrometer of an electromechanical type, working in the constant-acceleration mode was used. The 14.4 keV γ -rays were detected with a proportional counter. The velocity scale was calibrated at room temperature with metallic iron foil. The low temperature spectra were analyzed by means of a least squares fitting procedure with a set of magnetically-split spectral components corresponding to different local environments of iron atoms.

Thermogravimetric analysis. Thermogravimetric analysis (TGA) was done using a differential scanning calorimeter SDT Q600 (TA Instruments, New Castle, DE, USA). Samples in the form of powder were heated up to $1100\text{ }^\circ\text{C}$ with a heating rate of $\beta = 10\text{ }^\circ\text{C min}^{-1}$ in a He flux of 100 ml min^{-1} . The results of TG analysis were used to determine the mass of organic content in each as-made sample, which allowed us to normalize the magnetization of the experimental data with the nanoparticle amount.⁴⁴

X-ray photoelectron spectroscopy. Chemical characterization was carried out in a PHI 5000 VersaProbe II spectrometer with an Al $K\alpha$ monochromatic X-ray beam. The X-ray source was operated at 25 W and 15 kV beam voltages. Spectra were collected from 16 points each of $100\text{ }\mu\text{m}$ diameter. A separation distance of $100\text{ }\mu\text{m}$ between points was kept. This procedure allowed us to reduce the possible influence of the X-ray beam on the nanoparticles at every measured spot. Dual beam charge compensation with 7 eV Ar^+ ions and 1 eV electrons was used to maintain a constant sample surface potential regardless of the

sample conductivity. The pass energy of the hemispherical analyzer for the iron (Fe 2p) spectra was fixed at 23.5 eV and for other elements at 46.95 eV. Depth profiles were carried out with an Ar-GCIB with approximately 4000 atoms per cluster, 10 kV beam voltage and 35 nA current. The sputter area was set to $3 \times 3\text{ mm}^2$. Starting from the second analysis point, prior to the XPS measurement, sputtering was carried out for 2 minutes. The spectra were charge corrected to the main line of the carbon C 1s spectrum set to 284.8 eV.

For the XPS measurements, the synthesized nanoparticles were suspended in chloroform, then drops of the solution were deposited on a substrate (Si wafer) and left to dry. This procedure was repeated until the substrate was completely covered.

Results and discussion

Morphological and chemical characterization

The preparation of nanoparticles in thermal decomposition synthesis is usually carried out using one of two methods: 'hot injection' or 'heating-up' methods. The hot-injection method is based on achieving rapid homogeneous nucleation by injecting reagents into the surfactant solution (at high temperature) and then the growth phase can be controlled. The heating-up process comprises the gradual heating of the pre-mixed precursor solution, solvent and surfactant to a predetermined temperature, and thus initiation of the formation and growth of nanoparticles. In this work we focused on the heating-up process, in which the presence of squalane and dodecanoic acid in the reaction mixture and the introduction of Zn additives strongly affect the formation of the nanoparticles. Despite published works^{37,38} on the mechanisms of nucleation and growth during the formation of nanoparticles, creating an accurate model which takes into account all the parameters is still a challenge. The influence of all synthesis parameters on the shape, size and chemical composition of the nanoparticles is still largely empirically determined.^{45–47}

As mentioned in the experimental part, thermal decomposition syntheses of nanoparticles were undertaken in the presence of 0, 0.6 and 1.2 formula units of Zn in $\text{Zn}_x\text{Fe}_{3-x}\text{O}_4$, as the formation of magnetite was expected, based on existing literature on doping iron oxide nanoparticles.^{48,49} In this method, zinc(II) acetylacetonate and iron(III) acetylacetonate were used without any other iron(II) source. The ICP-OES measurements indicated the chemical composition of the obtained nanoparticles. Comparison of theoretical and experimentally determined formulae are

Table 1 Theoretical amounts of zinc and theoretical formulae compared with the actual amounts of zinc determined via ICP-OES measurements with the respective determined formula

Samples	Theoretical amount of zinc x	Theoretical formula	Determined amount of zinc x	Determined formula
S0	0	Fe_3O_4	0.00	Fe_3O_4
S1	0.6	$\text{Zn}_{0.6}\text{Fe}_{2.4}\text{O}_4$	0.14	$\text{Zn}_{0.14}\text{Fe}_{2.86}\text{O}_4$
S2	0.6	$\text{Zn}_{0.6}\text{Fe}_{2.4}\text{O}_4$	0.12	$\text{Zn}_{0.12}\text{Fe}_{2.88}\text{O}_4$
S3	1.2	$\text{Zn}_{1.2}\text{Fe}_{1.8}\text{O}_4$	0.24	$\text{Zn}_{0.24}\text{Fe}_{2.76}\text{O}_4$

summarized in Table 1. The results clearly indicate that the actual Zn content is much lower than expected. For these syntheses, it can be seen that Zn impoverishment is about 75–80% of what should be incorporated into the iron oxide structure. The lower content of zinc in the structure could be related to different reaction mechanisms, probably occurring when the nanoparticles were forming. For example, the reaction of the reduction of Fe(III) to Fe(II) might disturb zinc incorporation.⁴⁹

The morphology of the synthesized nanoparticles, their size and shape were determined using TEM. Observation of the nanoparticles at higher magnification allows us to determine their morphological details more precisely (for HR-TEM images see ESI†).

The nanoparticles obtained during syntheses S0 and S1 had an average size of 28.6 ± 3.4 nm and 22.3 ± 2.6 nm, respectively, while in the case of S2 and S3 syntheses, the obtained nanocrystallites had

slightly smaller average sizes, about 11.2 ± 1.4 nm and 9.6 ± 0.9 nm respectively.

Additionally, the biggest nanoparticles are hexagonal while the small ones consist of a mixture of hexagons, squares and spheres. S1 and S0 create agglomerates while S3 are mostly separated. These show possible magnetic interaction between larger nanoparticles. Micrographs with histograms are presented in Fig. 1 and 2, respectively. EDX analysis confirmed iron and oxygen in the S0 sample with the addition of zinc in all of the zinc ferrite nanoparticles (see ESI†). These resulted in a change in the local concentration of reactants, which remained in accordance with the literature data.⁴⁵ The size of the obtained crystallites, among other things, is significantly influenced by the temperature of the synthesis process, especially in the case of the synthesis of nanoparticles by the thermal decomposition of organometallic compounds.^{46,50}

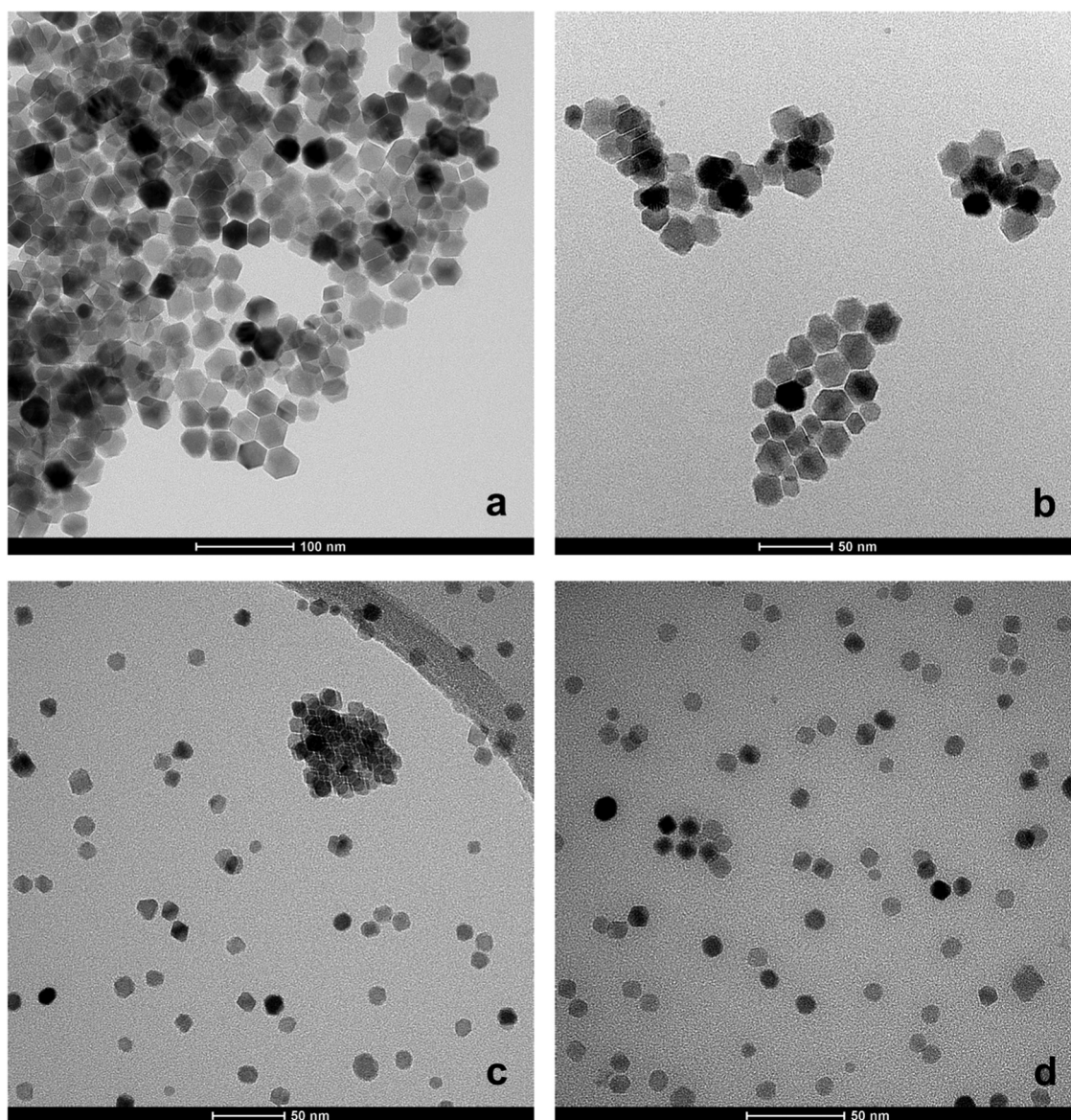


Fig. 1 TEM images for S0 (a), S1 (b), S2 (c), S3 (d).

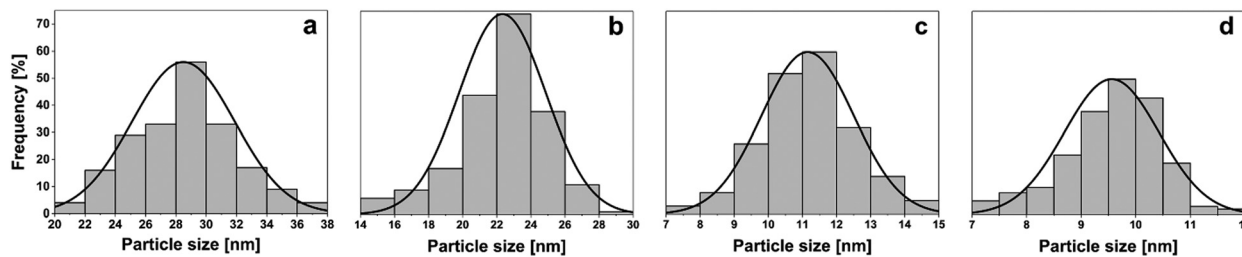


Fig. 2 Histograms fitted with normal size distribution of S0 (a), S1 (b), S2 (c), S3 (d).

Magnetic properties

In order to explore the magnetic properties of all the nanoparticle systems studied, a few milligram samples of loose particles with different zinc contents and geometries were probed. The magnetization of ferromagnetic nanoparticles is significantly responsive to the microstructure of the samples. Superparamagnetism occurs when the volume of a particle is so small that it consists of a single domain alone. Such particles preserve a

tendency to magnetization saturation, but magnetic hysteresis is suppressed. The latter is only observed below the blocking temperature, *i.e.* when the magnetic anisotropy energy of the superparamagnetic nanoparticle exceeds the thermal fluctuation energy.

Fig. 3 shows the hysteresis loops recorded at three selected temperatures, namely cryogenic ($T = 80$ K), room ($T = 290$ K) and elevated temperature ($T = 440$ K). All the studied samples

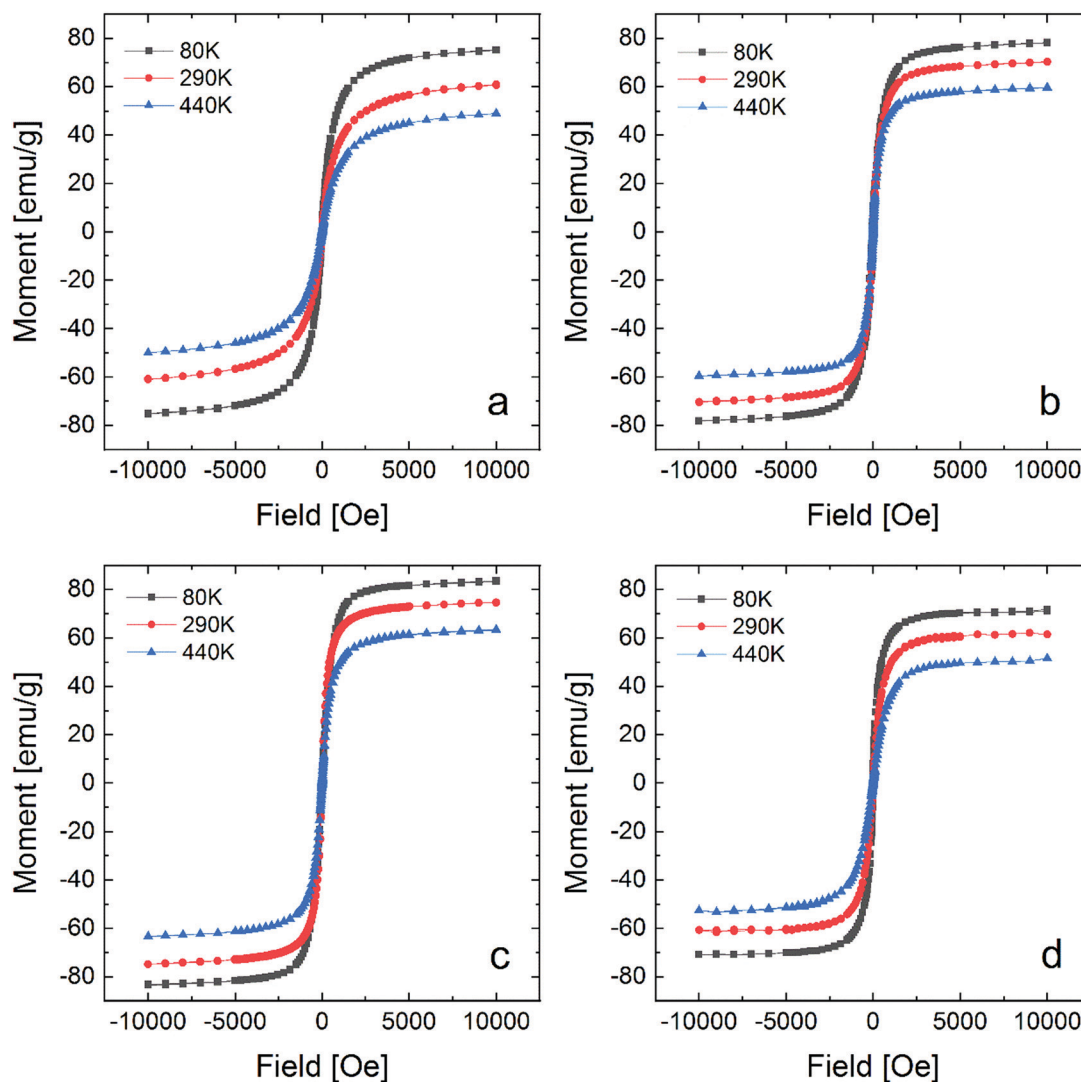


Fig. 3 Magnetization profiles for S0 (a), S1 (b), S2 (c) and S3 (d) samples.

exhibit a clear tendency to magnetic saturation, with a simultaneous lack of magnetic hysteresis at elevated temperature, which indicates a dominant superparamagnetic phase.

In addition, all the samples reach a similar value of saturation magnetization at 80 K, which is in the range of 70–85 emu g⁻¹ and decreases slightly with an increase in temperature, to reach approx. 60 emu g⁻¹ at 290 K. Specific magnetization refers to the inorganic volume of the samples studied, as derived from the TGA described in a later paragraph. At room temperature, hysteresis loop opening ($H_C = 10$ Oe) is observed in the case of S1 alone (see ESI†). This suggests that the magnetic anisotropy energy of the magnetic core of S1 is increased due to the formation of a thick Zn-rich magnetic shell and thus the total anisotropy of these particles is high enough to keep them (partially) blocked at room temperature. As expected, at a cryogenic temperature of 80 K, the larger nanoparticles exhibit discernable coercivity. This equals 9 Oe, 50 Oe, and 6 Oe, for samples S0, S1, and S2, respectively. Only sample S3 does not reveal any traces of hysteresis, which suggest that the majority of the particles forming this sample are thermally unblocked at $T = 80$ K. An accurate determination of the blocking temperature evolution is usually obtained by analysis of the temperature dependence of magnetic DC susceptibility, $\mu(T)$, upon zero-field cooling (ZFC). Provided that all the samples reveal a unimodal size distribution of similar width to mean size ratio and the dipolar magnetic interaction is negligible, the effective blocking temperature will be proportional to the temperature of the characteristic maxima in the ZFC curves, T_{\max} ,⁵¹ and thus it should correlate with the product of the magnetic volume and anisotropy of the particles. As shown in Fig. 4 and Table 2, correlation between T_{\max} and single particle diameter (d_{TEM}) is rather poor. This indicates that a Zn distribution leading to a core/shell structure enhances the magnetic anisotropy of the particles, which is demonstrated especially in the case of S1 and S2. Better correlation is observed between particle size and coercive field

Table 2 Comparison of the parameters deduced from magnetic characterization (H_C – coercive field, T_{\max} – temperature of ZFC curve maximum) and mean particle size (d_{TEM} – diameter corresponding to maximum of size distribution deduced from TEM micrographs)

Samples	H_C at 80 K [Oe]	T_{\max} [K]	d_{TEM} [nm]
S0	9	135 ± 5	28.6 ± 3.4
S1	50	115 ± 5 & 300 ± 5	22.3 ± 2.6
S2	6	180 ± 5	11.2 ± 1.4
S3	<1	<80	9.6 ± 0.9

observed at 80 K, with the exception of the S1 sample. In the latter case two maxima in the ZFC curve are discernable – at $T_{\max} \sim 115$ K and $T_{\max} \sim 300$ K, which are attributed to single particles and agglomerates of strongly interacting particles, respectively.

No traces of structural (Verwey type) phase transition in the $M(T)$ curves were observed within the temperature range probed as expected for the samples with the relative amount of Zn higher than $x > 0.035$. However, the lack of traces of such a transition in the S0 sample suggests that the magnetic core of these particles is partially oxidized toward maghemite.⁵²

Mössbauer spectroscopy

⁵⁷Fe Mössbauer spectroscopy (MS) measurements were performed in order to determine how Zn substitution influences the distribution of Fe ions in the spinel lattice and in order to search for possible traces of multiple phases due to *e.g.* particle decomposition or formation of shells. MS spectra were collected at room temperature ($T = 300$ K) and cryogenic temperature ($T = 80$ K). As shown in Fig. 5, the measurements performed at room temperature reveal significant differences between particles of different size and morphology, while only slight differences are present in the low temperature spectra. MS spectra of samples S0 and S1 collected at room temperature show a structured sextet shape, which confirms the good crystallinity of the particles.⁵³ As expected for nanoparticles larger than 20 nm in diameter, the magnetic hyperfine structure of these spectra can be well resolved. It consists of overlapping, broadened and asymmetrical lines, which demonstrate only weak traces of superparamagnetic relaxation phenomena.⁵⁴ Both spectra can be fitted using a linear combination of components characteristic of magnetite and maghemite (S0 sample) or zinc ferrite (S1 sample).

In the case of MS spectra of samples S2 and S3 probed at room temperature, strong relaxation is observed, which significantly affects spectral shape. Both spectra consist of a broad structure spanning -8 mm s⁻¹ to 8 mm s⁻¹ with a pronounced dip in the center. Such spectra are characteristic of the smallest ferrite nanoparticles. By comparing these results with the results obtained by Rebbouh *et al.*,⁵⁵ one can estimate that samples S2 and S3 are composed of ferrite nanoparticles with mean diameters of approx. 11 nm and 9 nm, respectively, which is in perfect agreement with TEM analysis.

MS spectra were also collected at cryogenic temperature. Lowering the temperature of measurement permits a reduction in the effect of thermal relaxation and, thus, it allows us to fit the spectra of the smallest particles with independent components in order to determine hyperfine interaction parameters. All the MS

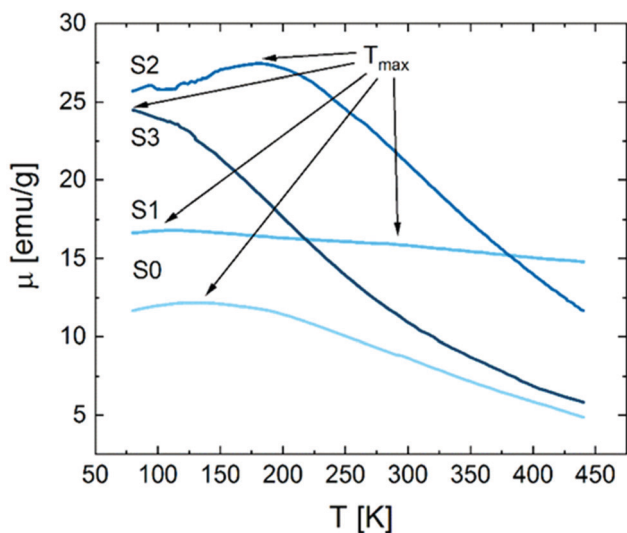


Fig. 4 ZFC temperature dependence of DC magnetic susceptibility at magnetic flux of 100 Gs.

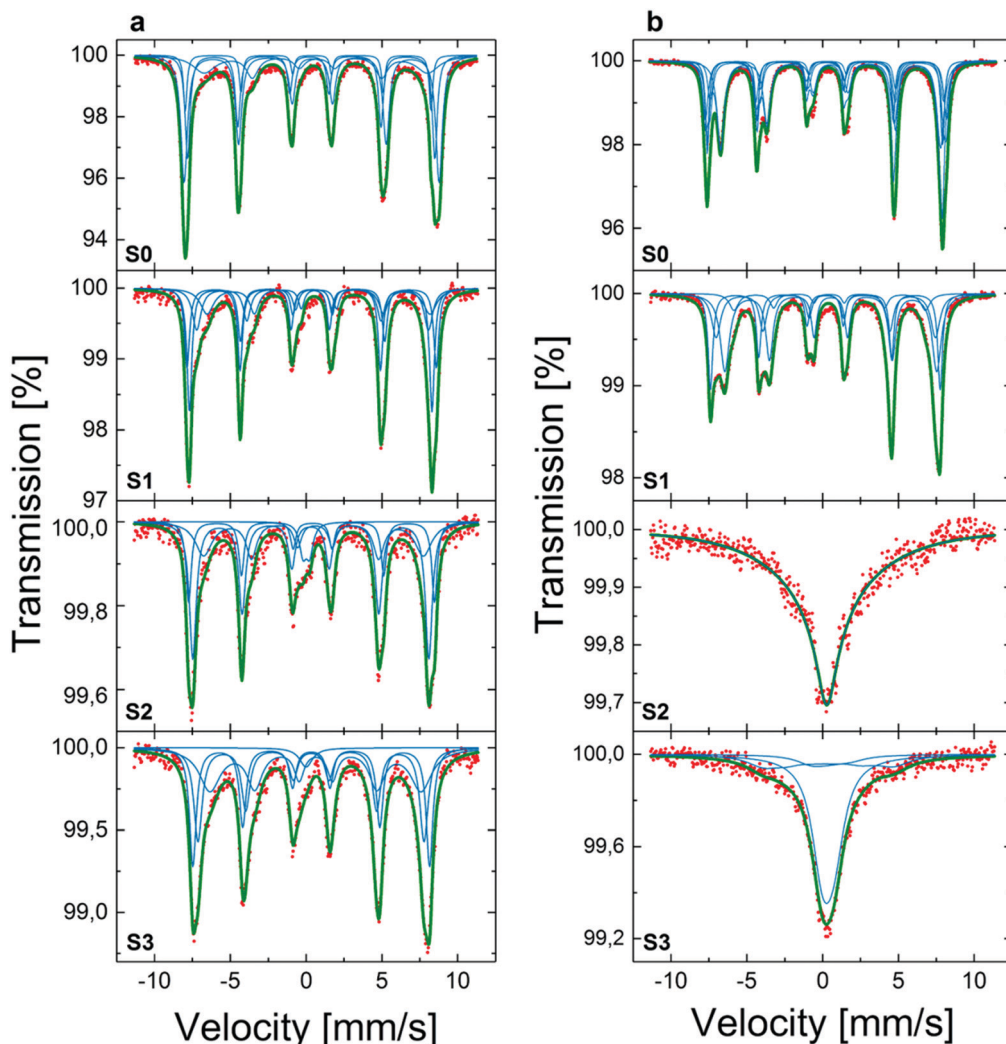


Fig. 5 ^{57}Fe Mössbauer spectra measured for all for samples at 80 K (a) and 300 K (b). Red dots represent experimental spectra, while the blue solid line is a result of the numerical fitting using individual components (green lines) corresponding to contributions described in text.

spectra collected at 80 K (Fig. 5) are primarily shaped by four overlapping sextets corresponding to distinct iron sites within the spinel structure.⁵⁶ However, in the case of samples S2 and S3, additional doublet or broad singlet lines, respectively, were added in order to correctly fit the spectra in a low velocity region. The latter are attributed to preserved relaxation profiles of the significant volumes of the smallest particles, which remain unblocked at $T = 80$ K.

Mean values of the hyperfine parameters determined from the MS spectra are shown in Table 3. The evolution of both mean isomer shift, $\langle\text{IS}\rangle$, and magnetic hyperfine field, $\langle H\rangle$, shows a similar trend at 80 K and 300 K. The mean hyperfine field increases with the mean size of the nanoparticles. This is in line with the expected single domain character, where the magnetic volume of the particles increases with their mean size. On the other hand, the values of mean isomer shift do not follow the expected stoichiometry. In spinel ferrites, the higher the mean isomer shift, the larger the amount of formal Fe^{2+} . Based on the room temperature data and thanks to a recently

Table 3 Mean $\langle\text{IS}\rangle$ and $\langle H\rangle$ values for all samples obtained at 80 K and 300 K with according to amount of zinc. $\langle\text{IS}\rangle$ is a weighted average of all the components of the spectrum, while $\langle H\rangle$ has been derived for magnetic components (sextets) alone

Samples	Determined amount of zinc	$\langle\text{IS}\rangle$ [mm s^{-1}]		$\langle H\rangle$ [kOe]	
		80 K	300 K	80 K	300 K
S0	0.00	0.402	0.348	502.7	469.4
S1	0.14	0.446	0.368	487.6	442.5
S2	0.12	0.370	0.272	453.0	406.0
S3	0.24	0.430	0.310	447.0	385.0

proposed method for determining mean iron oxidation from the MS spectra of magnetite/magnetite nanoparticles,⁵⁷ we estimate the $\text{Fe}^{2+}/\text{Fe}^{3+}$ ratio for sample S0 to be $\alpha \sim 0.15$. The larger value of the mean isomer shift of the S1 sample is attributed to a higher α value, but one significantly lower than the $\alpha \sim 0.4$ which is expected for homogeneous $\text{Zn}_{0.14}\text{Fe}_{2.86}\text{O}_4$ particles. These results confirm the non-homogeneous distribution of Zn within the particles, suggesting the possible core/shell character

of the obtained nanoparticles. In the case of S2 and S3 samples, the mean isomer shift values correspond to those observed in pure Fe³⁺ oxides. The latter can be rationalized by assuming that the iron-rich phase is built from maghemite.

Thermogravimetric analysis TGA

In order to better understand the interactions of organic medium (squalane, dodecanoic acid and dibenzyl ether) on the surface of the nanoparticles, TGA was carried out in the range from room temperature to 1100 °C (Fig. 6). Weight loss dependence on temperature shows decomposition of the organic compounds in four main distinct temperature ranges. At about 100 °C, loss of moisture was observed for all samples. At a higher temperature three steps of weight loss can be assigned to benzyl ether, dodecane and squalene, in accordance with the expected boiling points of these compounds. Within each step, the shapes of the TG curves are slightly different, depending on the sample. These can be caused by different compositions of the coating layers and interfacial interactions with nanoparticles. These also suggest that the stopping of the ongoing chemical decomposition reaction of the multicomponent layer takes place at different stages.

Total mass losses were equal to 18.2 and 17.0% for samples S0 and S1, respectively. Higher values were measured for samples S2 and S3, which contained smaller nanoparticles and they were equal to 19.6% and 20.6%, respectively (Table 4). Considering the mass of the nanoparticles and their composition appointed

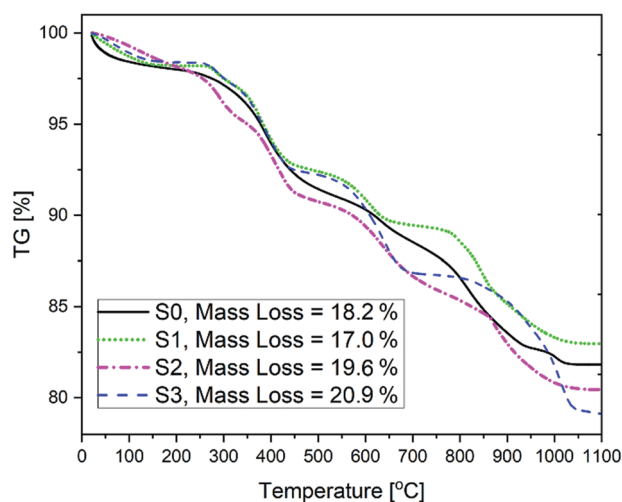


Fig. 6 The thermogravimetric (TG) curves of the as-made nanoparticles (S0–S3) at heating rate $\beta = 10 \text{ }^\circ\text{C min}^{-1}$ under an inert atmosphere.

Table 4 Summary of weight loss TGA results and particle size (d_{TEM} – diameter corresponding to maximum of size distribution deduced from TEM micrographs) of obtained nanoparticles (S0–S3) and C_L – mean carbon layer size

Samples	d_{TEM} [nm]	Wt loss TGA [%]	C_L [nm]
S0	28.6 ± 3.4	18.2	4.1
S1	22.3 ± 2.6	17.0	3.0
S2	11.2 ± 1.4	19.6	1.7
S3	9.6 ± 0.9	20.9	1.5

by ICP-OES, the average thickness of the organic layer was calculated. The results show that, although total mass losses increase with nanoparticle diameter, the thickness of the organic layer decreases with their size. The thickest layer was equal to 4.1 nm, which was calculated for nanoparticles of diameter 28.6 nm (S0), whereas the thinnest layer (1.5 nm) can be expected for the smallest nanoparticle with a diameter of 9.6 nm.

Theoretically estimated values of carbon layer thickness correspond to the data obtained from XPS measurements.

X-ray photoelectron spectroscopy (XPS)

To obtain preliminary information about the composition and potential contamination, XPS low resolution wide energy range spectra were taken (see ESI†). Spectra indicated the presence of carbon, oxygen and iron in S0, with additional zinc in the S1, S2 and S3 samples. Such results are in agreement with the EDX analysis shown in ESI.† To further exploit the structure of the nanoparticles, high resolution spectra of C 1s and Fe 2p regions were analyzed to determine the chemical states of the elements.

Fig. 7a shows a representative C 1s spectrum measured for S0 nanoparticles, after 2 minutes of argon cluster sputtering. It was fitted with three peaks with binding energies of 284.8, 286.0 and 288.5 eV. The first peak corresponds to squalane and dodecanoic acid capping of nanoparticles with residues of dibenzyl ether. The latter two lines come from dodecanoic acid (O–C=O) and dibenzyl ether (C–O), which were both used as an organic medium in synthesis.⁵⁸ These results correspond well to TGA results. S1 nanoparticles show no presence of an O–C=O line in the C1s spectrum. In S0 the O–C=O line is not as intense as in S2 and S3 (below 1% atomic concentration), which, with the TEM results, suggests that dodecanoic acid, alongside temperature, may have the biggest impact on the final size and shape of the obtained nanoparticles.

Analysis of the Fe 2p spectrum (Fig. 7b) showed the presence of Fe²⁺ and Fe³⁺ in the octahedral sites, and Fe³⁺ in the tetrahedral interstices.^{17,59,60} Similar spectra were observed for all samples. They prove that the synthesized nanoparticles were magnetite (S0) and zinc ferrite (S1, S2, S3).

The XPS information depth is about 10 nm for the organic layer and 4.5 nm for Fe₃O₄,^{61,62} which, combined with cluster sputtering, can indicate a core–shell structure of the studied nanoparticles, as was suggested on the basis of Mössbauer spectroscopy measurements. An Ar-GCIB allowed us to study subsequent layers of material without significant damage to the chemical composition, enabling elemental analysis of a core–shell structure.^{63–66}

The thickness of the organic shell on the nanoparticles represents the maximum of their values. One can expect that part of the organic compounds can form a thin layer on top of the samples, which appeared during the preparation of samples for XPS measurements. Nevertheless, the total thickness of the organic layer is thin enough to detect the inner part of the particles. This was proved by XPS measurements, in which the presence of iron was noticed for as-received (not sputtered) samples. Before sputtering, the C/Fe atomic concentration ratios increase with increasing total mass loss and decreasing

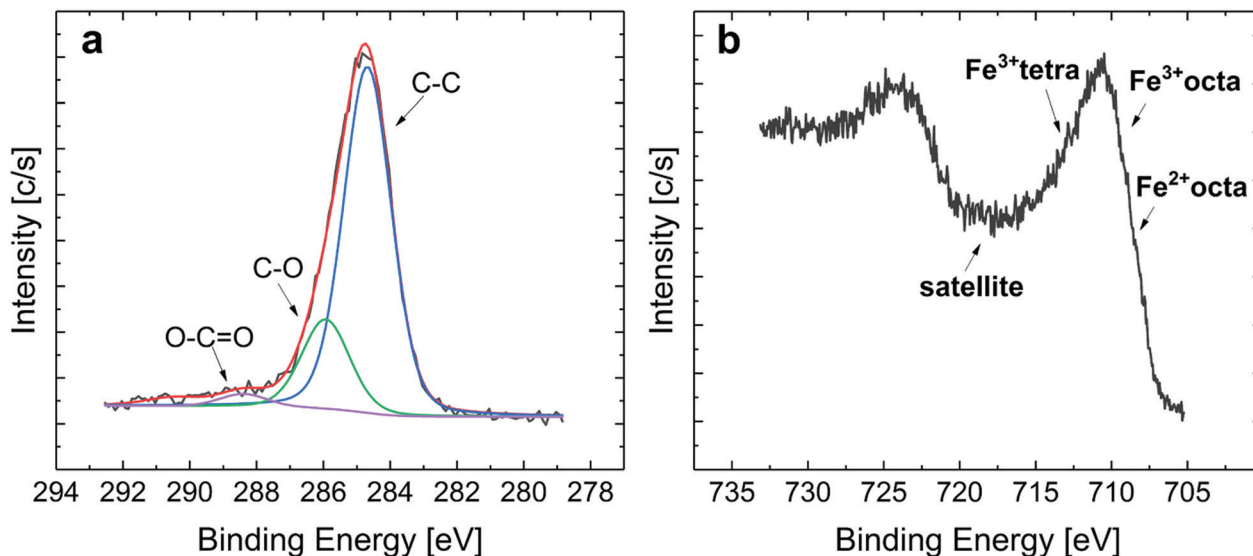


Fig. 7 XPS spectra C1s (a) and Fe2p (b) for S0 after 2 minutes of Ar-GCIB sputtering.

nanoparticle size. For the sample with the largest nanoparticles (S0) the ratio was estimated to be about 7 and it reached a value above 20 for S3, which were the smallest nanoparticles.

Sputtering depth profiles also show a visible distinction between large (S0 and S1) and small (S2 and S3) nanoparticles (Fig. 8a). For S0 the C/Fe atomic concentration ratio changed two-fold over 8 minutes of sputtering and then remained unchanged until the end of experiment. The initial carbon content in S1 was slightly higher; however, after 8 minutes of sputtering the ratio decreased two-fold and remained unchanged even after 28 minutes of sputtering, similar to the previously mentioned sample. In the case of small nanoparticles, the carbon content

exceeds that of iron by almost 20 times. For S2, the C/Fe ratio is decreasing during 24 minutes of sputtering, to finally stabilize at a ratio of 6 at the end of the measurement. A different value of the ratio is present in the S3 nanoparticles, where the carbon content decreases through the first 6 minutes to stabilize at a factor of 8 until the end of the experiment. Such a high factor derives from the carbon layer between neighboring nanoparticles. These observations display agreement between the C/Fe atomic concentration ratio and the organic content determined by TG analysis. It is also interesting to note that the relative changes in the C/Fe ratios with respect to these values measured after sputtering are very similar. For samples S1, S2 and S3 they vary

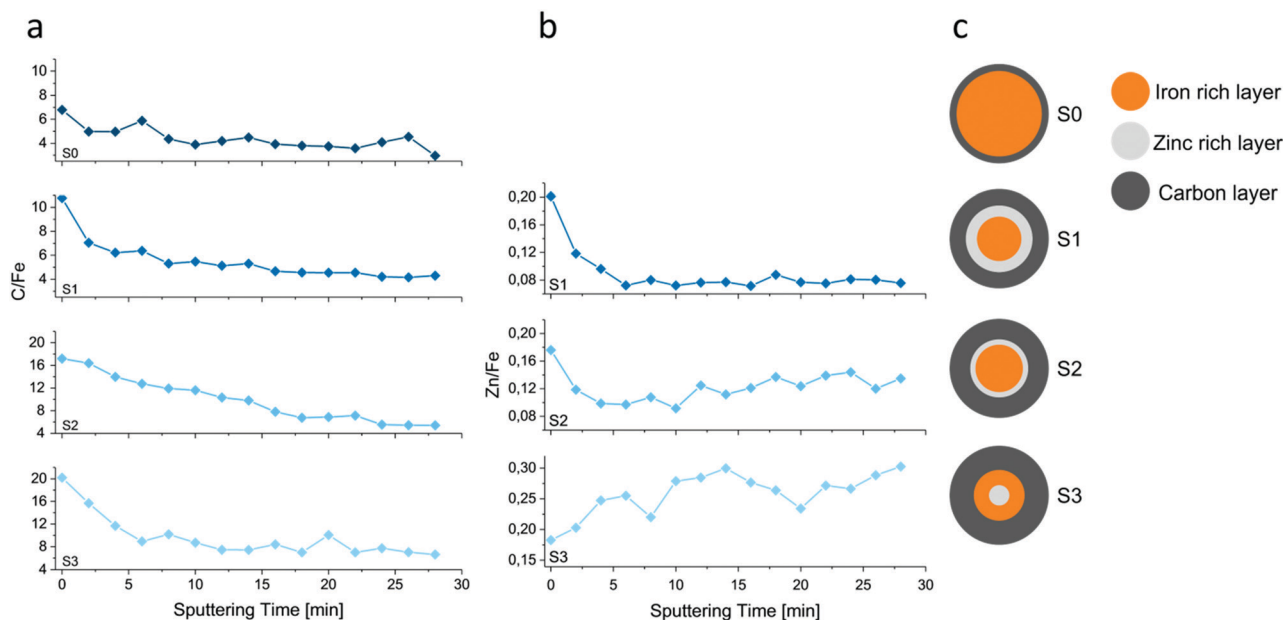


Fig. 8 In depth atomic concentration ratio of (a) C/Fe and (b) Zn/Fe determined from XPS measurements combined with Ar-GCIB sputtering with (c) core/shell model structures proposed on the basis of the obtained results.

between 2.5 and 2.8, but the value is slightly lower for S0, where it is estimated at 1.8. It can be concluded that the sample surface layer has no significant influence on the measured composition of the nanoparticles. The presence of the nanoparticle carbon shells can be considered to be confirmed by XPS.

The zinc to iron ratio in the as-received samples is roughly the same, however, after a sputtering change became noticeable (Fig. 8b). In syntheses S1 and S2, the ratio between zinc and iron behaves similarly: it significantly decreases during the first 6 minutes of sputtering. After that time, the ratio is stabilizing in S1 and slightly increases for the smaller nanoparticles of S2. On the basis of the above results, it can be concluded that zinc atoms are mostly present in the outer layer of the nanoparticles. A different type of zinc infusion is visible in S3 nanoparticles. In that case, the Zn/Fe ratio increases from 0.18 to 0.30 after 14 minutes of argon cluster sputtering, which indicates that zinc is present mostly inside the nanoparticles. The results in S3 showed that the changes in the structure of the layer could be formed at higher concentrations of zinc precursor. This increase in the concentration of zinc in the reaction mixture may affect the growth mechanism of the nanocrystallites.⁴⁵ The presented analysis of atomic concentration and ratios between C/Fe and Zn/Fe allowed us to create model structures of the synthesized nanoparticles, as depicted in Fig. 8c.

Conclusions

In this work we have developed a thermal decomposition method that allows us to obtain zinc ferrite nanoparticles with varying composition as well as defined shape and structure. The reactant mixture was composed of squalane, dodecanoic acid and dibenzyl ether acting as co-surfactants. Four sets of nanoparticles with a well-defined size exhibiting a low statistical distribution were prepared and tested using a wide spectrum of methods to verify the proposed synthesis products. Depending on the controlled variables, the diameter of the nanoparticles varies between 9.6 nm and 28.6 nm. It was found that the size decreases when the amount of zinc increases. The largest nanoparticles were obtained for undoped nanoparticles (S0). These showed hexagonal structures whereas small Zn-doped nanoparticles consist of a mixture of hexagons, squares and spheres.

In the final stage of synthesis, carbon layer shells were formed on the nanoparticles. The shells were characterized by TG analysis and XPS measurements, which allowed us to estimate their thickness, varying between 1.5 nm and 4.1 nm, and their increase with nanoparticle size. The carbon shell was enriched mainly in squalane, although, after removing the outer part of the shell by ion cluster sputtering, the concentration of dodecanoic acid and ether slightly increases for small nanoparticles (S2 and S3). This was discussed as being due to the possibility of stronger interaction of the carboxylate with the surface of iron oxide.

Magnetic characterization confirmed the single domain character of the obtained nanoparticles in all proposed compositions and proved the superparamagnetic behavior of all the samples.

Systematic studies indicated that Zn acts as a dopant to iron oxide nanoparticles. Both VSM and Mössbauer spectroscopy confirmed the non-homogeneous distribution of Zn within the particles, suggesting their core/shell character. XPS depth profiling with Ar-GCIB revealed the Zn distribution within the nanoparticles. A higher Zn concentration at the nanoparticle shell was observed for nanoparticles with lower Zn content, independently of their size (S1, S2). Inversion of the Zn distribution was observed for particles with the highest Zn content (S3). In this case, Zn concentration was lower at the surface in favor of a higher content in the core of the nanoparticle.

Conflicts of interest

There are no conflicts to declare.

Acknowledgements

The work was partly supported by the EU Project POWR.03.02.00-00-I004/16 and partly supported by the National Science Centre, Poland, grant no. 2016/23/D/ST8/00013.

References

- 1 M. Neamtu, C. Nadejde, V.-D. Hodoroaba, R. J. Schneider, L. Verestiuc and U. Panne, *Sci. Rep.*, 2018, **8**, 6278.
- 2 P. Tartaj, M. P. Morales, T. Gonzalez-Carreño, S. Veintemillas-Verdaguer and C. J. Serna, *Adv. Mater.*, 2011, **23**, 5243–5249.
- 3 Z. Zhao, Z. Zhou, J. Bao, Z. Wang, J. Hu, X. Chi, K. Ni, R. Wang, X. Chen, Z. Chen and J. Gao, *Nat. Commun.*, 2013, **4**, 2266.
- 4 S. Xia, E. Metwalli, M. Opel, P. A. Staniec, E. M. Herzig and P. Müller-Buschbaum, *ACS Appl. Mater. Interfaces*, 2018, **10**, 2982–2991.
- 5 S. Xia, L. Song, V. Körstgens, M. Opel, M. Schwartzkopf, S. V. Roth and P. Müller-Buschbaum, *Nanoscale*, 2018, **10**, 11930–11941.
- 6 K. C. Icli and M. Ozenbas, *Electrochim. Acta*, 2018, **263**, 338–345.
- 7 C. Thu, P. Ehrenreich, K. K. Wong, E. Zimmermann, J. Dorman, W. Wang, A. Fakharuddin, M. Putnik, C. Drivas, A. Koutsoubelitis, M. Vasilopoulou, L. C. Palilis, S. Kennou, J. Kalb, T. Pfadler and L. Schmidt-Mende, *Sci. Rep.*, 2018, **8**, 3559.
- 8 A. Ali, H. Zafar, M. Zia, I. Ul Haq, A. R. Phull, J. S. Ali and A. Hussain, *Nanotechnol., Sci. Appl.*, 2016, **9**, 49–67.
- 9 L. Lin, S. A. Starostin, V. Hessel and Q. Wang, *Chem. Eng. Sci.*, 2017, **168**, 360–371.
- 10 R. M. Cornell and U. Schwertmann, *The iron oxides: structure, properties, reactions, occurrences, and uses*, Wiley-VCH, 1996.
- 11 D. Bonvin, D. Alexander, A. Millán, R. Piñol, B. Sanz, G. Goya, A. Martínez, J. Bastiaansen, M. Stuber, K. Schenk, H. Hofmann and M. Mionić Ebersold, *Nanomaterials*, 2017, **7**, 225.
- 12 S. L. Easo and P. V. Mohanan, *Carbohydr. Polym.*, 2013, **92**, 726–732.

- 13 W. Wu, Z. Wu, T. Yu, C. Jiang and W. S. Kim, *Sci. Technol. Adv. Mater.*, 2015, **16**, 23501.
- 14 J. M. Byrne, V. S. Coker, E. Cespedes, P. L. Wincott, D. J. Vaughan, R. A. D. Pattrick, G. Van Der Laan, E. Arenholz, F. Tuna, M. Bencsik, J. R. Lloyd and N. D. Telling, *Adv. Funct. Mater.*, 2014, **24**, 2518–2529.
- 15 E. H. Kim, H. S. Lee, B. K. Kwak and B. K. Kim, *J. Magn. Magn. Mater.*, 2005, **289**, 328–330.
- 16 L. M. Bronstein, X. Huang, J. Retrum, A. Schmucker, M. Pink, B. D. Stein and B. Dragnea, *Chem. Mater.*, 2007, **19**, 3624–3632.
- 17 D. Wilson and M. A. Langell, *Appl. Surf. Sci.*, 2014, **303**, 6–13.
- 18 A. Szpak, G. Kania, T. Skórka, W. Tokarz, S. Zapotoczny and M. Nowakowska, *J. Nanopart. Res.*, 2013, **15**, 1372.
- 19 K. Petcharoen and A. Sirivat, *Mater. Sci. Eng., B*, 2012, **177**, 421–427.
- 20 A. Kmita, D. Lachowicz, J. Żukrowski, M. Gajewska, W. Szczerba, J. Kuciakowski, S. Zapotoczny and M. Sikora, *Materials*, 2019, **12**, 1048.
- 21 M. Wahajuddin and S. Arora, *Int. J. Nanomed.*, 2012, **7**, 3445–3471.
- 22 M. W. Freeman, A. Arrott and J. H. L. Watson, *J. Appl. Phys.*, 1960, **31**, S404–S405.
- 23 A. Tari, R. W. Chantrell, S. W. Charles and J. Popplewell, *Physica B+C*, 1979, **97**, 57–64.
- 24 D. D. Majumder, D. D. Majumder and S. Karan, *Ceramic Nanocomposites*, Elsevier, 2013, pp. 51–91.
- 25 M. Wen, Q. Li and Y. Li, *J. Electron Spectrosc. Relat. Phenom.*, 2006, **153**, 65–70.
- 26 G. Mu, X. Pan, N. Chen, C. He and M. Gu, *Appl. Surf. Sci.*, 2008, **254**, 2483–2486.
- 27 U. Klekotka, B. Piotrowska, D. Satuła and B. Kalska-Szostko, *Appl. Surf. Sci.*, 2018, **444**, 161–167.
- 28 C. M. Phan and H. M. Nguyen, *J. Phys. Chem. A*, 2017, **121**, 3213–3219.
- 29 S. Upadhyay, K. Parekh and B. Pandey, *J. Alloys Compd.*, 2016, **678**, 478–485.
- 30 Q. K. Ong, A. Wei and X. M. Lin, *Phys. Rev. B: Condens. Matter Mater. Phys.*, 2009, **80**, 134418.
- 31 P. B. Shete, R. M. Patil, N. D. Thorat, A. Prasad, R. S. Ningthoujam, S. J. Ghosh and S. H. Pawar, *Appl. Surf. Sci.*, 2014, **288**, 149–157.
- 32 K. Wang, C. Yi, C. Liu, X. Hu, S. Chuang and X. Gong, *Sci. Rep.*, 2015, **5**, 9265.
- 33 W. Zhang, N. A. Nguyen, R. Murray and M. E. Mackay, *Sol. Energy Mater. Sol. Cells*, 2017, **160**, 126–133.
- 34 J. Wu, Y. Wang, W. Jiang, S. Xu and R. Tian, *Appl. Surf. Sci.*, 2014, **321**, 43–49.
- 35 R. Hong, J. Li, S. Zhang, H. Li and Y. Zheng, *Appl. Surf. Sci.*, 2009, **255**, 3485–3492.
- 36 J. Du, Y. Ding, L. Guo, L. Wang, Z. Fu, C. Qin, F. Wang and X. Tao, *Appl. Surf. Sci.*, 2017, **425**, 164–169.
- 37 S. Bera, A. A. M. Prince, S. Velmurugan, P. S. Raghavan, R. Gopalan, G. Panneerselvam and S. V. Narasimhan, *J. Mater. Sci.*, 2001, **36**, 5379–5384.
- 38 H. Deng, X. Li, Q. Peng, X. Wang, J. Chen and Y. Li, *Angew. Chem., Int. Ed.*, 2005, **44**, 2782–2785.
- 39 P. Guardia, J. Pérez-Juste, A. Labarta, X. Batlle and L. M. Liz-Marzán, *Chem. Commun.*, 2010, **46**, 6108–6110.
- 40 D. Cabrera, A. Lak, T. Yoshida, M. E. Materia, D. Ortega, F. Ludwig, P. Guardia, A. Sathya, T. Pellegrino and F. J. Teran, *Nanoscale*, 2017, **9**, 5094–5101.
- 41 Y. Yang, X. Liu, Y. Yang, W. Xiao, Z. Li, D. Xue, F. Li and J. Ding, *J. Mater. Chem. C*, 2013, **1**, 2875.
- 42 D. Niculaes, A. Lak, G. C. Anyfantis, S. Marras, O. Laslett, S. K. Avugadda, M. Cassani, D. Serantes, O. Hovorka, R. Chantrell and T. Pellegrino, *ACS Nano*, 2017, **11**, 12121–12133.
- 43 L. T. Lu, N. T. Dung, L. D. Tung, C. T. Thanh, O. K. Quy, N. V. Chuc, S. Maenosono and N. T. K. K. Thanh, *Nanoscale*, 2015, **7**, 19596–19610.
- 44 J. Lohr, A. A. de Almeida, M. S. Moreno, H. Troiani, G. F. Goya, T. E. T. Molina, R. Fernandez-Pacheco, E. L. Winkler, M. V. Mansilla, R. Cohen, L. C. C. M. Nagamine, L. M. Rodríguez, D. E. Fregenal, R. D. Zysler and J. Enio Lima, *J. Phys. Chem. C*, 2019, **123**(2), 1444–1453.
- 45 E. C. Vreeland, J. Watt, G. B. Schober, B. G. Hance, M. J. Austin, A. D. Price, B. D. Fellows, T. C. Monson, N. S. Hudak, L. Maldonado-Camargo, A. C. Bohorquez, C. Rinaldi, D. L. Huber and J. Crayton Pruitt, *Chem. Mater.*, 2015, **27**(17), 6059–6066.
- 46 S. Belaïd, D. Stanicki, L. Vander Elst, R. N. Muller and S. Laurent, *Nanotechnology*, 2018, **29**, 165603.
- 47 M. Unni, A. M. Uhl, S. Savliwala, B. H. Savitzky, R. Dhavalikar, N. Garraud, D. P. Arnold, L. F. Kourkoutis, J. S. Andrew and C. Rinaldi, *ACS Nano*, 2017, **11**, 2284–2303.
- 48 X. Liu, J. Liu, S. Zhang, Z. Nan and Q. Shi, *J. Phys. Chem. C*, 2016, **120**(2), 1328–1341.
- 49 W. Szczerba, J. Żukrowski, M. Przybylski, M. Sikora, O. Safonova, A. Shmeliov, V. Nicolosi, M. Schneider, T. Granath, M. Oppmann, M. Straßer and K. Mandel, *Phys. Chem. Chem. Phys.*, 2016, **18**, 25221–25229.
- 50 S. Bégin-Colin, O. Ersen, S. Moldovan, C. Kiefer, C. Blanco-Andujar, D. Ihiawakrim, F. Pertont, G. Cotin, B. Pichon, C. Lefevre and D. Mertz, *Nanomaterials*, 2018, **8**, 881.
- 51 S. H. Masunaga, R. F. Jardim, M. J. Correia and W. Figueiredo, *J. Phys. Chem. C*, 2016, **120**, 765–770.
- 52 R. Aragón, D. J. Buttrey, J. P. Shepherd and J. M. Honig, *Phys. Rev. B: Condens. Matter Mater. Phys.*, 1985, **31**, 430–436.
- 53 N. Viart, G. Pourroy and J.-M. Greneche, *Eur. Phys. J.: Appl. Phys.*, 2002, **18**, 33–40.
- 54 J. S. Salazar, L. Perez, O. De Abril, L. T. Phuoc, D. Ihiawakrim, M. Vazquez, J. Greneche, S. Begin-colin and G. Pourroy, *Chem. Mater.*, 2011, **23**, 1379–1386.
- 55 L. Rebbouh, R. P. Hermann, F. Grandjean, T. Hyeon, K. An, A. Amato and G. J. Long, *Phys. Rev. B: Condens. Matter Mater. Phys.*, 2007, **76**, 1–12.
- 56 V. Chlan, J. Żukrowski, A. Bosak, Z. Kąkol, A. Kozłowski, Z. Tarnawski, R. Řezníček, H. Štěpánková, P. Novák, I. Bialo and J. M. Honig, *Phys. Rev. B*, 2018, **98**, 125138.
- 57 J. Fock, L. K. Bogart, D. González-Alonso, J. I. Espeso, M. F. Hansen, M. Varón, C. Frandsen and Q. A. Pankhurst, *J. Phys. D: Appl. Phys.*, 2017, **50**, 265005.

- 58 E. Johansson and L. Nyborg, *Surf. Interface Anal.*, 2003, **35**, 375–381.
- 59 T. Radu, C. Iacovita, D. Benea and R. Turcu, *Appl. Surf. Sci.*, 2017, **405**, 337–343.
- 60 F. Han, L. Ma, Q. Sun, C. Lei and A. Lu, *Nano Res.*, 2014, **7**, 1706–1717.
- 61 Z. Beji, M. Sun, L. S. Smiri, F. Herbst, C. Mangeney and S. Ammar, *RSC Adv.*, 2015, **5**, 65010–65022.
- 62 S. T. H. Shinotsuka, C. J. Powell and D. R. Penn, *Surf. Interface Anal.*, 2015, **47**, 871–888.
- 63 P. J. Cumpson, J. F. Portoles, A. J. Barlow and M. Birch, *Surf. Interface Anal.*, 2013, **45**, 1859–1868.
- 64 S. H. Kim, S. Heo, S.-G. Ihn, S. Yun, J. H. Park, Y. Chung, E. Lee, G. Park and D.-J. Yun, *Appl. Phys. Lett.*, 2014, **104**, 243303.
- 65 M. Gosecka, J. Raczowska, J. Haberko, K. Awsiuk, J. Rysz, A. Budkowski, M. M. Marzec, A. Bernasik and T. Basinska, *Colloids Surf., A*, 2016, **507**, 200–209.
- 66 A. Bernasik, J. Haberko, M. M. Marzec, J. Rysz, W. Łuźny and A. Budkowski, *J. Vac. Sci. Technol., B: Nanotechnol. Microelectron.: Mater., Process., Meas., Phenom.*, 2016, **34**, 030604.

Electronic Supplementary Material (ESI) for Physical Chemistry Chemical Physics.
This journal is © the Owner Societies 20XX

Supporting Information

Gradient of zinc content in the core-shell zinc ferrites nanoparticles - precise study on composition and magnetic properties

Dorota Lachowicz^{a‡}, Roma Wirecka^{b‡}, Weronika Górka-Kumik^d, Mateusz Marek Marzec^a, Marta Gajewska^a, Angelika Kmita^a, Jan Żukrowski^a, Marcin Sikora^a, Szczepan Zapotoczny^c, Andrzej Bernasik^{b*}

^aAGH University of Science and Technology, Academic Centre for Materials and Nanotechnology, al. A. Mickiewicza 30, 30-059 Krakow, Poland

^bAGH University of Science and Technology, Faculty of Physics and Applied Computer Science, al. A. Mickiewicza 30, 30-059 Krakow, Poland

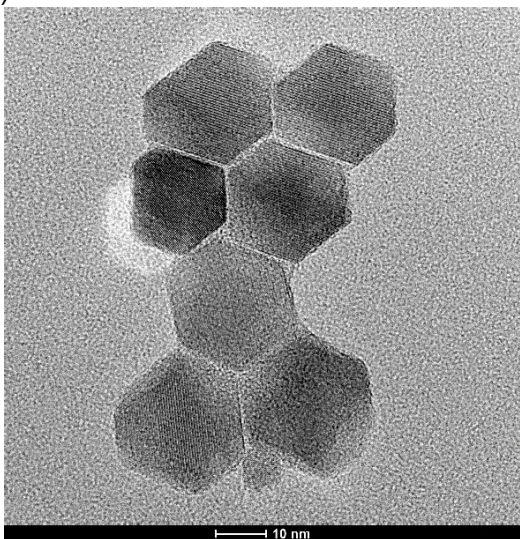
^cFaculty of Chemistry, Jagiellonian University, Gronostajowa 2, 30-387 Krakow, Poland

^dFaculty of Physics, Astronomy and Applied Computer Science, Jagiellonian University, prof. Stanisława Łojasiewicza 11, 30-348 Krakow, Poland

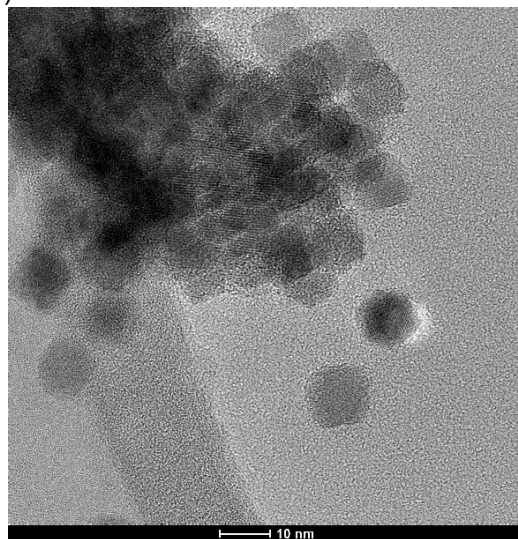
[‡] These authors equally contributed to the manuscript

^{*}Corresponding author, e-mail: bernasik@agh.edu.pl

A.)



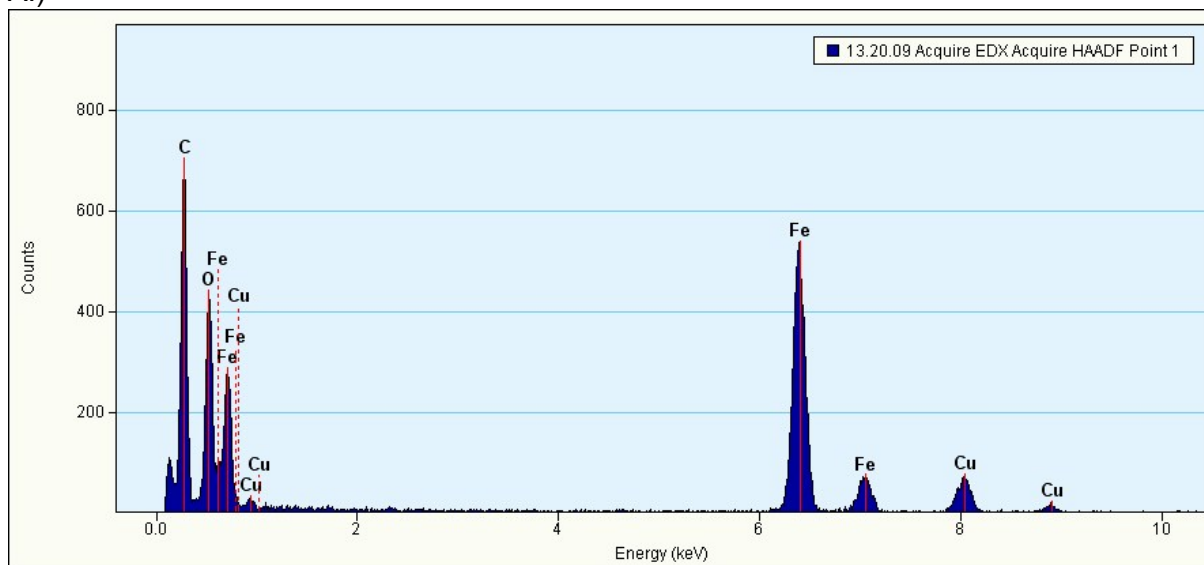
B.)



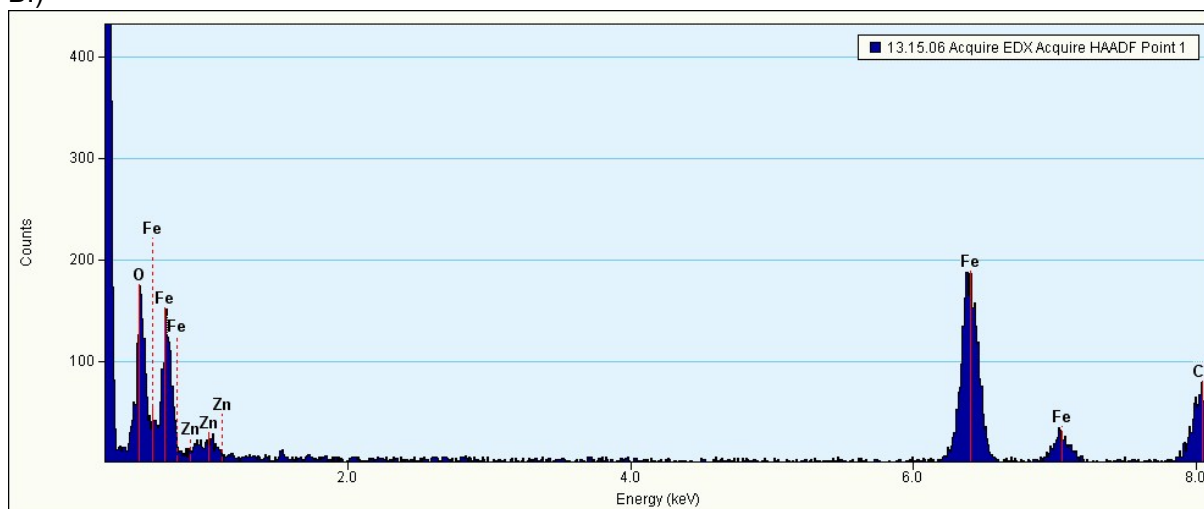
C.)

Figure. S1. HR-TEM pictures of S1(a), S2(b), S3(c) nanoparticles

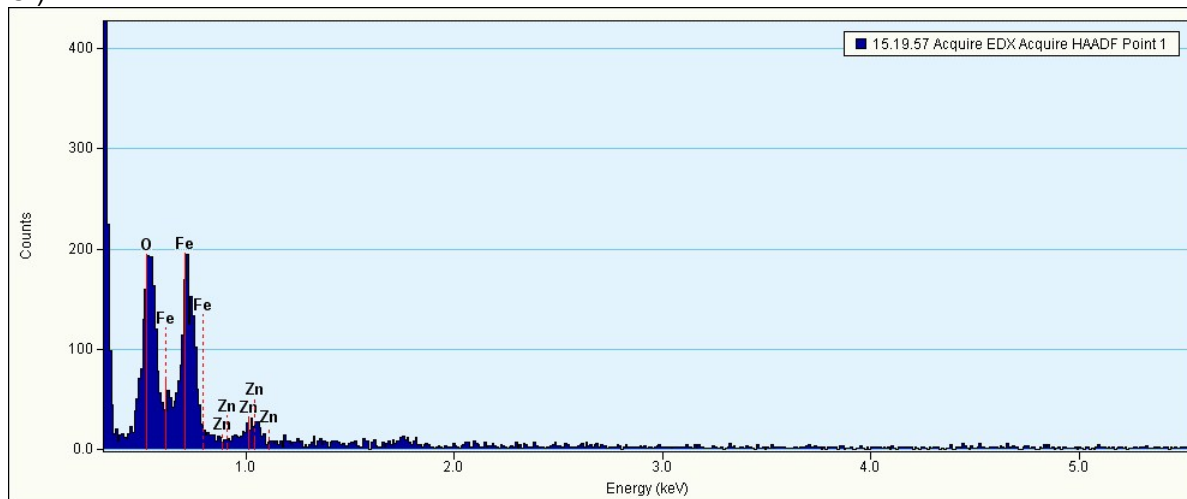
A.)



B.)



C.)



D.)

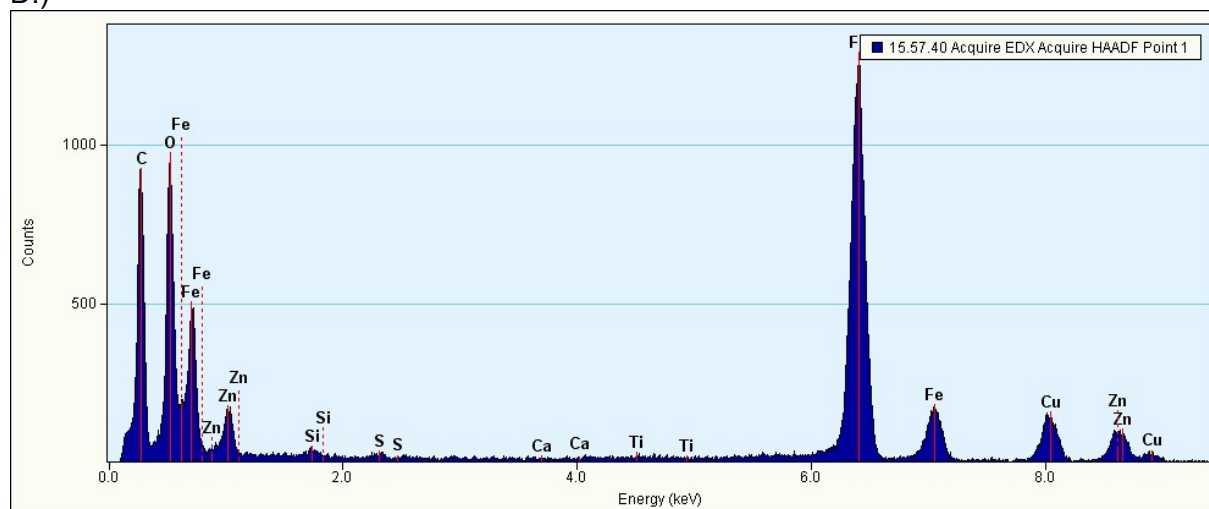


Figure. S2. EDX analysis of S0 (a), S1 (b), S2 (c), S3 (d) nanoparticles

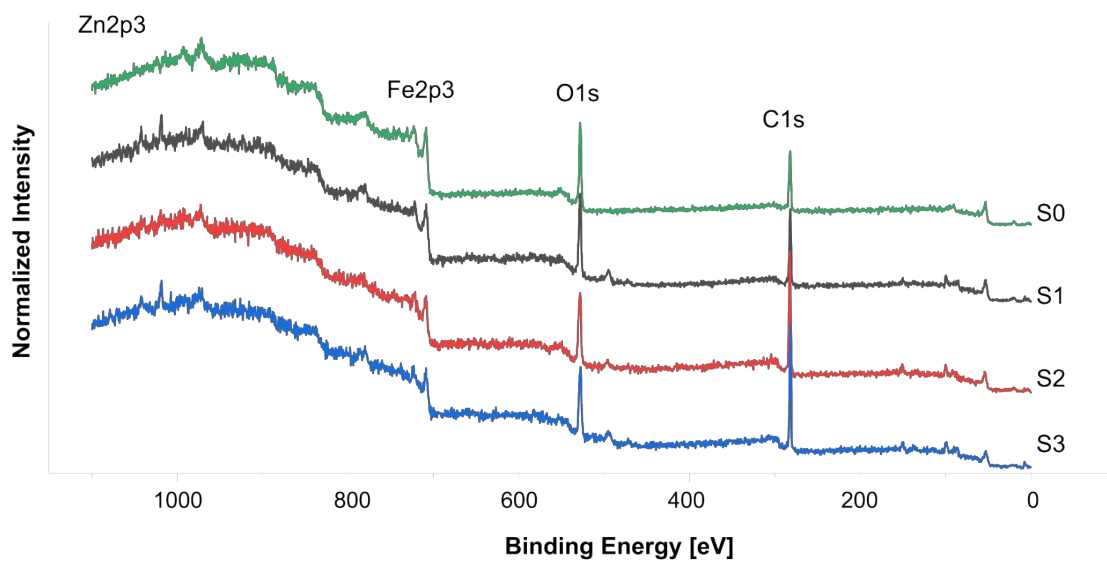


Figure. S3 Survey XPS spectra of magnetite and zinc ferrite nanoparticles

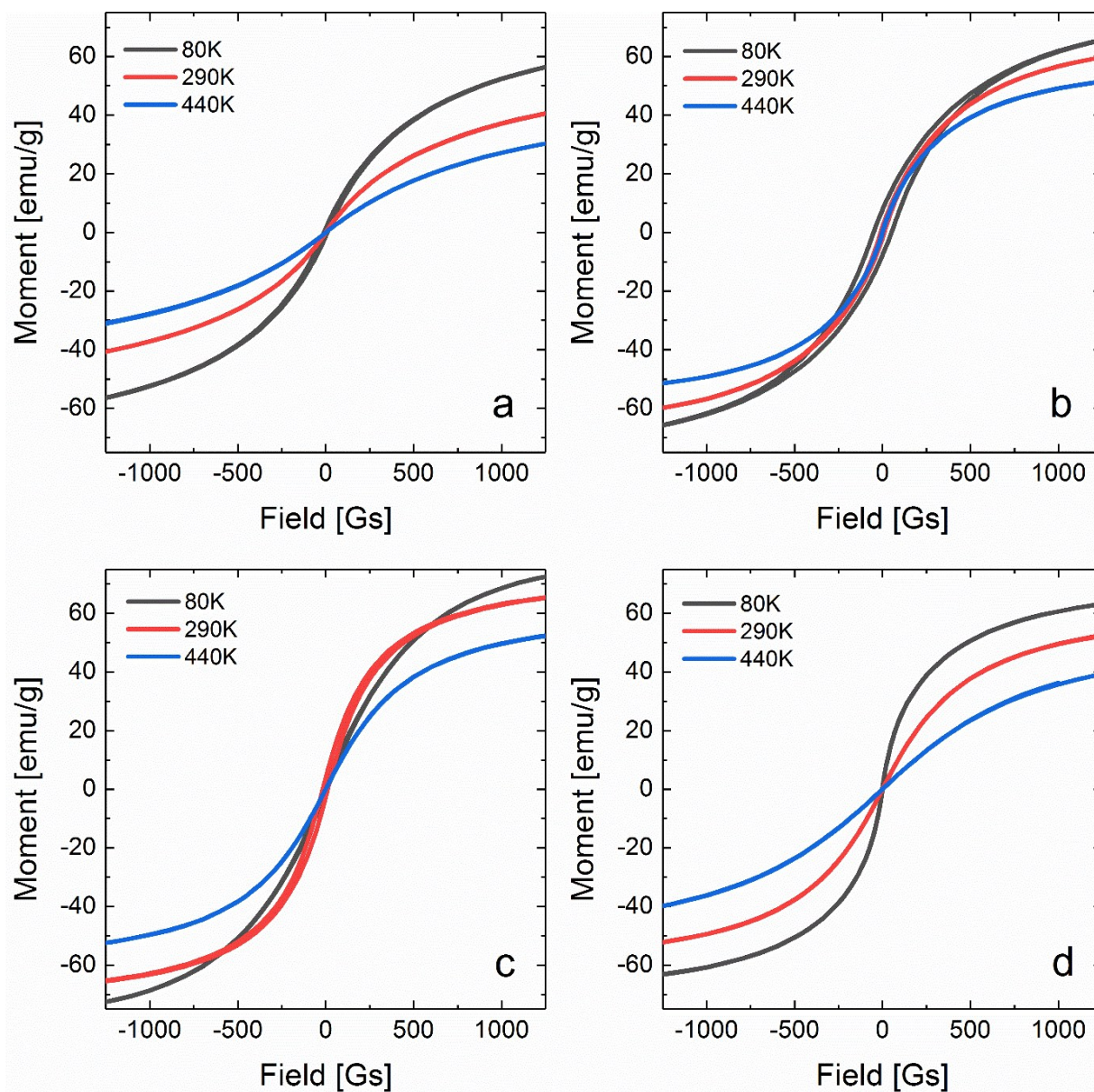


Figure. S4. Hysteresis loops for S0 (a), S1 (b), S2 (c), S3 (d).

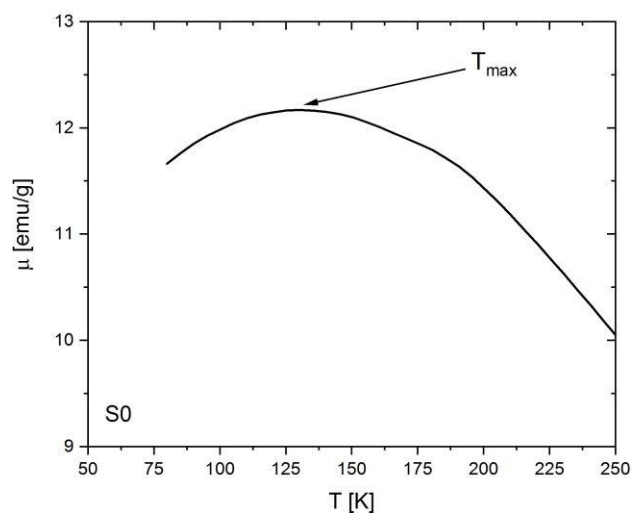


Figure S5. ZFC temperature dependence of DC magnetic susceptibility at magnetic flux of 100Gs for sample S0.

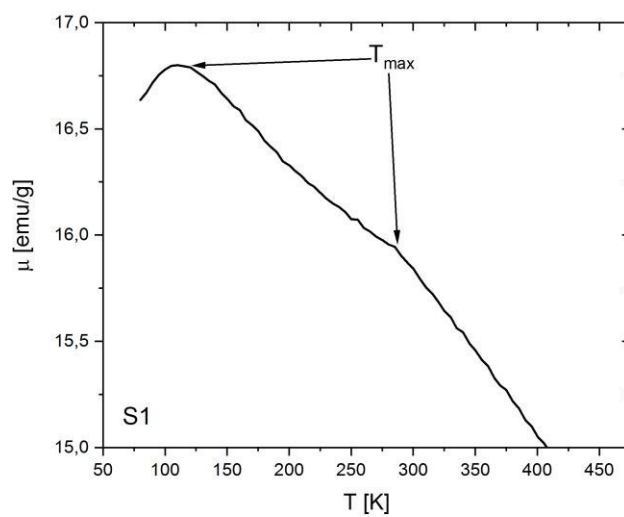
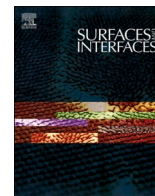


Figure S6. ZFC temperature dependence of DC magnetic susceptibility at magnetic flux of 100Gs for sample S1.



Ion distribution in iron oxide, zinc and manganese ferrite nanoparticles studied by XPS combined with argon gas cluster ion beam sputtering

R. Wirecka^{a,b,*}, D. Lachowicz^b, K. Berent^b, M.M. Marzec^b, A. Bernasik^{a,b}

^a Faculty of Physics and Applied Computer Science, AGH University of Science and Technology, A. Mickiewicza Av. 30, 30-059 Cracow, Poland

^b Academic Centre for Materials and Nanotechnology, AGH University of Science and Technology, A. Mickiewicza Av. 30, 30-059 Cracow, Poland

ARTICLE INFO

Keywords:

Monoatomic argon ion beam
Argon gas cluster ion beam
Nanoparticles
iron oxide
XPS

ABSTRACT

In this work, the influence of X-ray irradiation and two types of surface sputtering methods is thoroughly studied. The first one, monoatomic sputtering, resulted in the reduction of iron oxide to the metallic iron in a short time of sputtering. The second studied technique is argon cluster sputtering, which uses lower energies per atom, hence the modification of the structure of the samples is greatly reduced. Based on the XPS characterization of Fe₃O₄ single crystal the fitting procedure for the Fe 2p spectra for nanoparticles is established. The preliminary results showed that X-rays combined with cluster sputtering resulted in alteration of the morphology and solidification of the surface of the samples. In the response to the morphology modification, the Spot-by-Spot Cluster Procedure is proposed. It allows to thoroughly characterize the layer-by-layer structure of the nanoparticles, without changing it. The Procedure was used to determine the structure of zinc, manganese and zinc-manganese ferrite nanoparticles. Finally, the results show, that depending on the used dopant, its incorporation and the state of iron are changed.

1. Introduction

Ferrite nanoparticles are a group of materials in which some of the iron atoms are substituted with other metals, such as zinc, manganese, cobalt, nickel, and others. Even with the small alteration of the stoichiometry, tremendous changes in the biocompatibility [1], magnetic response [2–4], electrical properties [5], or thermal conductivity [6] of the material can be seen. Such a broad spectrum of possibilities, paved the way for numerous applications in different fields like catalysis [7], hyperthermia [8], electrical technologies [9], magnetic aerogel materials [10], or even water splitting [11]. However, the understanding of the structure, hence the different properties may be a challenge.

Since the distribution of cation dopants has a significant impact on the final properties of the material, knowledge of how different dopants incorporate into the structure is of high importance in the field of materials engineering [12,13]. Up till now, one of the methods used for such analysis was X-ray photoelectron spectroscopy (XPS) which could reveal only the surface composition and chemical state at the surface of the material, unless combined with synchrotron radiation [13–15]. To obtain information about subsequent layers of the material the depth profiling technique must be applied, which can be achieved by

combining XPS with ion sputtering [16,17]. Unfortunately, studies show that monoatomic ion sputtering tends to alter the structure of the material because of the preferential sputtering and other phenomena like interlayer mixing which is a result of high kinetic energy influencing small part of the material [18,19]. Another approach allowing to reveal subsequent layers of the materials is ion gas cluster sputtering. This technique is characterized by the bombardment of the surface with clusters of atoms, in which final energy delivered per atom to the sample is much lower, hence the risk of structural alteration is greatly reduced [20,21]. An additional advantage of the large cluster sputtering is the reduction of ion mixing, interlayer mixing and preferential sputtering which consequently leads to better depth profiling resolution in comparison to the monoatomic one [22–24].

In this study, a thorough analysis of the influence of X-ray photon beam and two different types of argon sputtering is presented. Firstly, monoatomic sputtering characterized with the high energy of sputtering is used to examine the iron oxide single crystal. Secondly, as an alternative, argon cluster sputtering is proposed. It is a gentler technique with the incident energy per atom of single electronvolts, which allows observing the subsequent layers of the material. Finally, a fitting procedure with additional suggestions on how to distinguish different types

* Corresponding author.

E-mail address: roma.wirecka@fis.agh.edu.pl (R. Wirecka).

of iron species that may be present in the XPS Fe 2p spectra is proposed. The procedure based on the macroscopic magnetite crystal is tested on the four types of iron oxide nanoparticles as a way to study the incorporation of the different dopants in the structure of the nanoparticles.

2. Experimental

2.1. Materials

Fe(acac)₃ (acac = acetylacetonate) (97%), Zn(acac)₂ (≥95%), Mn(acac)₂ (≥95%), dibenzyl ether (≥98%), squalane (≥95%), dodecanoic acid (≥98%) were purchased from Sigma Aldrich. Al reagents were of analytical grade and were used without any purification.

2.2. Synthesis of the nanoparticles

Synthesis of the nanoparticles was performed following the procedure described elsewhere [25]. Briefly, for the iron oxide and ferrite nanoparticles (Fe₃O₄ (Fe(Sq)), Zn_xFe_{3-x}O₄ (Zn(Sq)), Mn_xFe_{3-x}O₄ (Mn(Sq)) or Mn_xZn_yFe_{3-x-y}O₄ (MnZn(Sq))), 0.8 mmol Fe(acac)₃, 0.2 mmol M(acac)₂ (M = Zn, Mn or (0.5Zn+0.5Mn)), 3 mmol of dibenzyl ether, 10 mL of squalane and 15 mL of dodecanoic acid were mixed in a glass flask. For the Fe(Sq) nanoparticles 1.0 mmol of Fe(acac)₃ was used. The mixture was heated to 80°C and kept for 90 minutes. Subsequently, the mixture was heated to 200°C and kept for 90 minutes and finally, flask was heated to 280°C and the temperature was maintained for 60 minutes. The final product was let to cool down to the room temperature, cleaned in the acetone and suspended in the chloroform. To prepare the samples for the spectroscopy measurements, the suspension was drop-casted onto previously cleaned silica substrate and left to dry. Such parameters allowed obtaining nanoparticles with similar diameter of 10 nm.

2.3. X-ray Photoelectron Spectroscopy (XPS)

The XPS measurements were carried out on PHI 5000 VersaProbe II spectrometer with an Al K α monochromatic x-ray beam. The X-ray source was operated at 25 W and 15 kV beam voltage. The incident angle was set to 45°. To avoid any kind of charge deposition, samples were neutralized by low energy electron beam and monoatomic argon beam (Ar⁺). The pass energy was set to 23.5 eV (for iron) or 46.95 eV (for other elements). The Argon Gas Cluster Ion Beam (Ar-GCIB) sputtering parameters were set to 10 kV beam voltage and 35 nA current with approx. 4000 atoms per cluster. The size of the sputtered area was set to 4 × 4 mm and spectra were collected from its center. During the sputtering Zalar rotation was applied. The main oxygen line, with the binding energy of 529.8 eV, was used as the charge shift correction. This value was applied as a result of the previous experiments [25]. For background subtraction, the Iterated Shirley method was applied.

In order to establish the influence of the X-ray beam and the type of the sputtering (Ar⁺ for monoatomic or Ar-GCIB for cluster) on the iron oxide crystallite, three different procedures for the XPS measurements were performed: Single-Spot Procedure, Spot-by-Spot Monoatomic Procedure and Spot-by-Spot Cluster Procedure. For both Spot-by-Spot procedures, spectra were collected from the neighboring spots separated by 100 μ m from each other (Figure 1).

The X-ray influence

In this procedure, all of the spectra were collected from one spot at the surface of the crystal. Before the first spectrum acquisition, Ar-GCIB sputtering was performed for 2 minutes to eliminate surface impurities. Afterward, no further sputtering was performed. Seventeen collections were taken with total irradiation time being approx. 170 minutes.

Single-Spot Procedure

The influence of Ar-GCIB and X-ray on the ferrite nanoparticles was

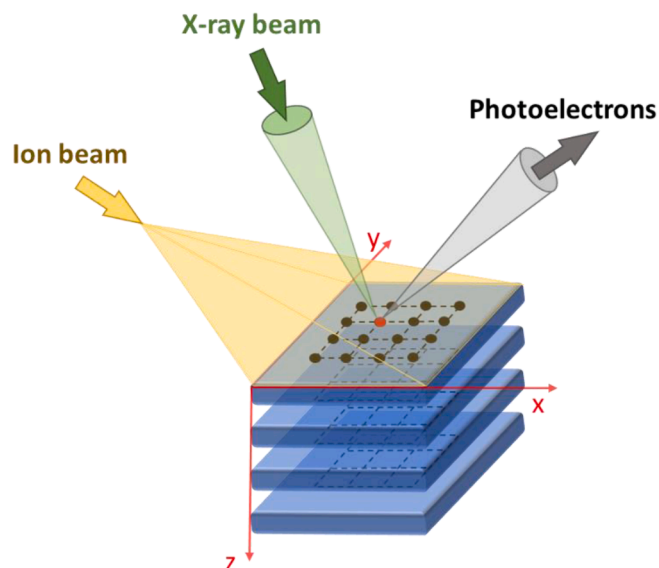


Figure 1. Schematic view of the procedure of sputtering and spectra acquisition in the Spot-by-Spot Procedures. Each dot represents spot of 100 μ m in diameter which was irradiated by the X-ray beam.

established by taking succeeding acquisitions in one spot of 400 μ m. Before every acquisition, Ar-GCIB sputtering was performed for 2 minutes. After the measurement of zinc ferrite nanoparticles, the protocol was modified. Since then, spectra were collected using the Spot-by-Spot Cluster Procedure (see section 0).

The monoatomic sputtering (Spot-by-Spot Monoatomic Procedure)

In this case, before each spectra acquisition, Ar⁺ sputtering was performed for 1 minute (with Zalar rotation) with 2 kV beam voltage and 2 μ A current.

The sputtering rate for Ar⁺ sputtering with presented parameters (current density equals 0.13 μ A/mm²) was 2 nm/min of sputtering determined by the stylus profilometer DektakXT on the silica oxide substrate and similar results were reported [26].

The Gas Cluster Ion Beam sputtering (Spot-by-Spot Cluster Procedure)

In the last proposed approach, the first measurement was made with as received sample but before following measurements, Ar-GCIB sputtering was performed for 2 minutes. Such procedure was established to avoid repetitive X-ray irradiation of the same area more than once.

The sputtering rate for Ar-GCIB on the silica oxide substrate with chosen parameters was lower than the detection limit of the stylus profilometer DektakXT.

3. Results and discussion

As a result of the spin-orbit splitting in 3d transition metals, the Fe 2p spectrum is divided into two regions – Fe 2p_{3/2} and Fe 2p_{1/2}. Fe₃O₄ crystallizes in a cubic inverse spinel structure. It consists of iron in two different oxidation states and in two different crystallographic structures: Fe²⁺ in octahedral sites (Fe²⁺_{octa}) and Fe³⁺ in octahedral (Fe³⁺_{octa}) and tetrahedral sites (Fe³⁺_{tetra}) [27]. Those three species with the addition of the Fe_{def} line, are present in Fe 2p_{3/2} region. Additionally, both oxidation states have ascribed satellites shifted approximately 6-8 eV to the corresponding mainline [28,29]. Fe_{def} line is typically connected with defected structures [30], and examined Fe₃O₄ crystallite may have some surface and lattice defects, which have an impact onto the iron chemical state. As a result of smaller intensity of Fe 2p_{1/2} region and errors that can occur in the higher binding energy range, the analysis will be based only on Fe 2p_{3/2} region [31].

3.1. Fe_3O_4 crystal and the influence of the X-ray beam on the iron oxide

To study the influence of the X-ray beam, on the magnetite, one spot at the surface of Fe_3O_4 single crystal was chosen and 17 subsequent measurements were performed. Every acquisition was done in the same area. During the measurement, the Fe 2p spectra were not changing which showed, that X-ray used in the XPS does not have a measurable influence on the iron oxide (Figure 2a).

3.2. The influence of the method of the sputtering on the iron oxide

One of the most commonly used methods of sputtering in XPS is Ar^+ ion sputtering, which can cause sample modification even with possible damage [2]. To establish the difference between the two types of sputtering, two different measurements were made. Firstly, the Fe_3O_4 single crystal was sputtered with the Ar^+ beam using Spot-by-Spot Monoatomic Procedure. Another measurement was based on the Spot-by-Spot Cluster Procedure made in a different place of the sample.

As it can be seen in the Figure 2b and e, an alteration occurs in the Fe 2p spectra, depending on the applied method of sputtering. After 7 minutes of Ar^+ sputtering, Fe^0 line appears at the binding energy of 706.4 ± 0.1 eV which corresponds well with the literature [32]. It indicates that a monoatomic argon beam can reduce the oxidation state of the iron. Analysis of the atomic concentration showed that, while Fe^0 concentration rises, the concentration of other iron species present in the measured sample, decreases. Worth emphasizing observation is that the sample sputtered with Ar-GCIB has no reduced iron in its structure (Figure 2d).

The second visible alteration of the Fe 2p spectra occurs in the satellite region (712-720 eV). Before sputtering, the line ascribed to the Fe^{3+} satellite has a higher intensity which indicates the presence of α -, γ - Fe_2O_3 at the surface of the sample [29,33]. After sputtering, Fe^{2+} satellite line increases drastically when sputtered with Ar^+ , however only slight and steadily progressing changes are visible after Ar-GCIB sputtering (shown in the Figure 2e). Additionally, right to the Fe^{2+} satellite line, Fe_{def} line can be placed. Looking at the drastic increase of

the intensity of the lines in the Ar^+ sputtering, there is a possibility, that not only Fe^{2+} satellite increases, but also the concentration of the defects.

Knowing the differences in the impact of both Ar^+ and argon cluster sputtering, the results obtained with the Ar-GCIB were used to create the fitting procedure for Fe 2p region, which after small adjustments is useful for spectra analysis of the nanoparticles. Fitting was based on the spectra collected after every two minutes of sputtering which showed, that the topmost layer of the crystal is made of Fe_2O_3 which after layer-by-layer removal by argon clusters, changes to the Fe_3O_4 with the 1:1:1 ratio of the iron species ($\text{Fe}^{2+}_{\text{octa}}$: $\text{Fe}^{3+}_{\text{octa}}$: $\text{Fe}^{3+}_{\text{tetra}}$). Additionally, before sputtering, the peak attributed to $\text{Fe}^{2+}_{\text{satellite}}$, is not visible, though after sputtering its intensity is increasing (Figure 2c,d), and both satellite lines can be properly fitted with binding energies of 715.6 ± 0.2 and 718.7 ± 0.2 eV for Fe^{2+} and Fe^{3+} satellite, respectively.

3.3. Influence of Ar-GCIB and X-ray on the Zn(Sq) nanoparticles

During the Fe_3O_4 single crystal measurements, it became clear, that the impact of the monoatomic Ar^+ beam onto the structure of the sample may be too high to perform a reliable nanoparticles structure study with the Spot-by-Spot Monoatomic Procedure. As a result, another approach was chosen. All acquisitions were made in one spot and before each, 2 minutes of Ar-GCIB sputtering was performed. The goal was to remove the carbon layer present at the surface of the nanoparticles, as the post-synthesis drawback, and with little to no alterations in the structure and morphology of the nanoparticles [25].

Spectrum acquisition following the Single-Spot Procedure resulted in the removal of most of the carbon layer, made of capping agents from the synthesis. The atomic concentration of carbon decreased from 41% to 5% during 14 minutes of sputtering. On the other hand, the concentration of iron increased from 14.2% to 34.3%. The amount of zinc in the structure was stable with a value of 1.8%. The table with all concentrations can be found in the ESI as a Table S1. After the XPS measurement (14 minutes of sputtering) and removing the sample, there was a visible $400 \mu\text{m} \times 400 \mu\text{m}$ square left, possibly made of unsputtered

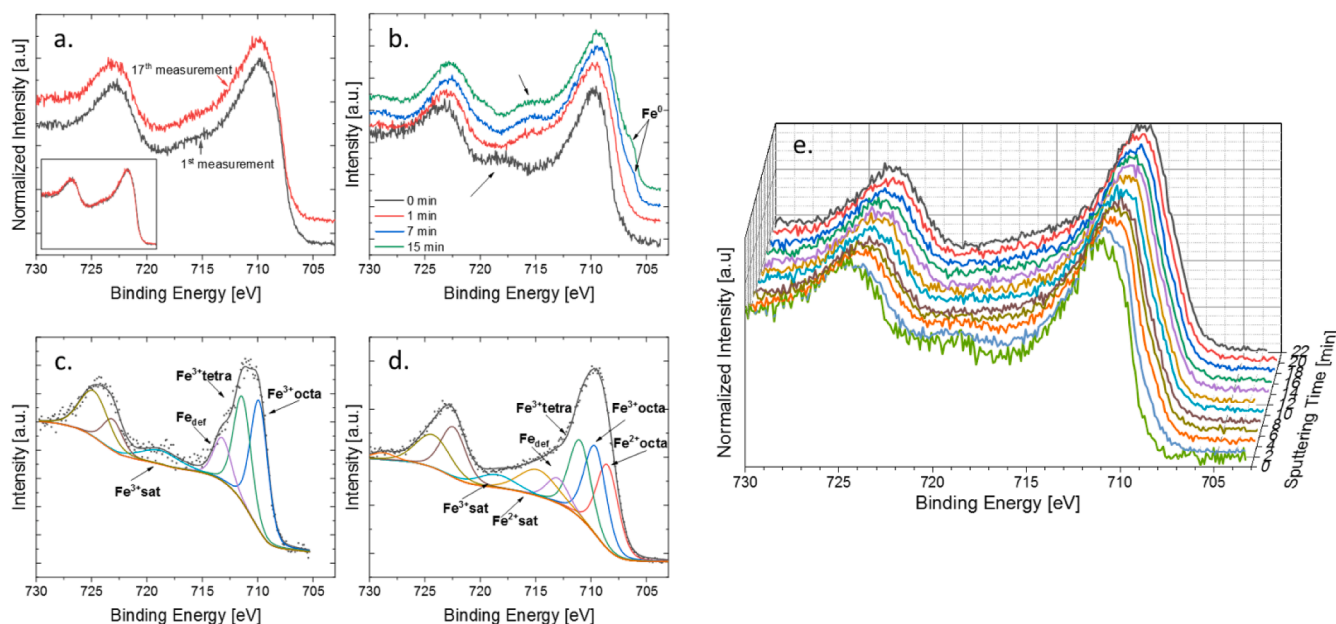


Figure 2. Selected XPS spectra for the Fe_3O_4 single crystal showing the impact of X-ray, Ar^+ , and Ar-GCIB sputtering on the iron oxide structure; (a) two XPS Fe 2p spectra of first and seventeenth measurement made in one spot, presenting nondestructive impact of the X-ray on the Fe_3O_4 structure even after approx. 170 min of irradiation. The inset presenting both spectra normalized and overlapping showing no differences between two spectra; (b) XPS results for the Fe 2p region measured after four different times of Ar^+ sputtering, presenting the impact of sputtering on the iron oxide structure, with arrows pointing alterations resulting from the Ar^+ sputtering; (c) XPS spectra for Fe_3O_4 crystal before Ar-GCIB and (d) after 22 minutes of Ar-GCIB sputtering, with fitted lines showing changes in the line intensities and the crystal structure; (e) all Fe 2p spectra made after every two minutes of Ar-GCIB sputtering.

nanoparticles (Figure 3a). SEM image of the remaining part of the sample was taken, which showed that nanoparticles free from carbon layer, connect so strongly that it is not possible to remove them with the use of the low energetic Ar-GCIB. Additionally, energy delivered with the X-ray beam locally sinter zinc ferrite nanoparticles. Before sputtering, Zn(Sq) nanoparticles create visible steps of layers on the SEM images (Figure 3c and d). After the XPS measurement, no regular lines are visible (Figure 3e). These results show, that taking multiple spectra acquisition in one spot results in the alteration of the morphology of the sample possibly by combining the energy of the argon clusters and the X-ray. Thorough structure study for the Zn(Sq) (results published in the [25]) state that iron-rich phase in such nanoparticles is made from maghemite which is in contradiction to the results obtained after 14 minutes of the single-spot sputtering. Hence, to ensure the lack of the influence of the applied methodology of the XPS measurement on the results, another approach for the nanoparticles is necessary - the Spot-by-Spot Cluster Procedure.

The XPS spectra comparing both proposed procedures are shown in the Figure 3f and Figure 3g, for the Single-Spot and the Spot-by-Spot Cluster Procedure, respectively.

3.4. Comparison of the Fe 2p region in the Fe(Sq), Mn(Sq), Zn(Sq) and MnZn(Sq) nanoparticles

The Fe 2p spectra for all studied ferrite nanoparticles are presented in the Figure 4. On the left side are presented spectra before Ar-GCIB sputtering, while on the right side - after 30 minutes of cluster sputtering following the Spot-by-Spot Cluster Procedure. All of that results concern nanoparticles with similar morphology and diameter. Additionally, detailed changes of concentrations in the iron species with the dopant concentrations alterations are presented in the Figure 5. Fitting parameters for all four types of nanoparticles can be found in the Table S2 and Table S3 in the ESI for Fe 2p and Zn 2p with Mn 2p, respectively.

In case of the pure iron oxide nanoparticles (Fe(Sq), Figure 4 a, b),

before sputtering the intensity ratio of iron lines is 0.5:1:1 ($\text{Fe}^{2+}_{\text{octa}}:\text{Fe}^{3+}_{\text{octa}}:\text{Fe}^{3+}_{\text{tetra}}$), suggesting that the nonstoichiometric structure creates the surface of the nanoparticle. After 10 minutes of sputtering, most of the carbon layer is removed and the ratio of iron lines reaches almost 1:1:1 (Figure 5 a) – the theoretical value for the structure of magnetite (Fe_3O_4). One should acknowledge, that the Fe_{def} line is not taken into account while establishing $\text{Fe}^{2+}/\text{Fe}^{3+}$ ratio. The ratio is stable during the rest of the sputtering. Additionally, the satellite area (712-720 eV) changes during the measurement suggesting, that the surface of the nanoparticle is mostly made of α - or γ - Fe_2O_3 with the Fe_3O_4 in the core (drastic rise of the intensity in the $\text{Fe}^{2+}_{\text{sat}}$ line).

Similar changes in the iron species ratio can be found in the manganese ferrite (Mn(Sq), Figure 4 c, d). At the surface, the $\text{Fe}^{2+}_{\text{octa}}$ line is of low intensity (the ratio of iron lines being 0.3:1:0.8), and the proportion of the manganese ions to iron is high. After 6 to 8 minutes of sputtering, the iron line ratio changes, to reach the 1:1:1 with additional decrease of the manganese to iron ratio from 0.6 to 0.14 (Figure 5 c). Moreover, the FWHM (full width at half maximum) for all of the iron lines decreases during sputtering by the 0.2 eV. Such observations suggest that some additional states of iron, possibly connected to the manganese atoms in the structure, are removed with the decrease of the manganese in the core. Knowing that it can be proposed that at the surface of the nanoparticle manganese replaces the $\text{Fe}^{2+}_{\text{octa}}$ atoms. During the substitution of the iron by the manganese, the structure tends to change from inverse to the mixed spinel, hence it can be stated that the Mn(Sq) sample is made of the mixed spinel. Additionally, the Mn 2p XPS spectrum analysis confirms that the manganese is present in two states in the sample: Mn^{2+} (640.6 ± 0.2 eV) and Mn^{3+} (642.4 ± 0.2 eV) (spectra can be found in the Figure S1 in the ESI). The ($\text{Mn}^{2+}:\text{Mn}^{3+}$) ratio of the lines decreases during the sputtering from 2:1 to 1.7:1, which proves small alterations in the Mn(Sq) nanoparticles in the subsequent layers of the sample. Because the ion sputtering tends to reduce the oxidation state of metal ions in the sample, results in which the exact opposite is happening proves, that the established Spot-by-Spot Cluster Procedure is a suitable and effective choice for the characterization of

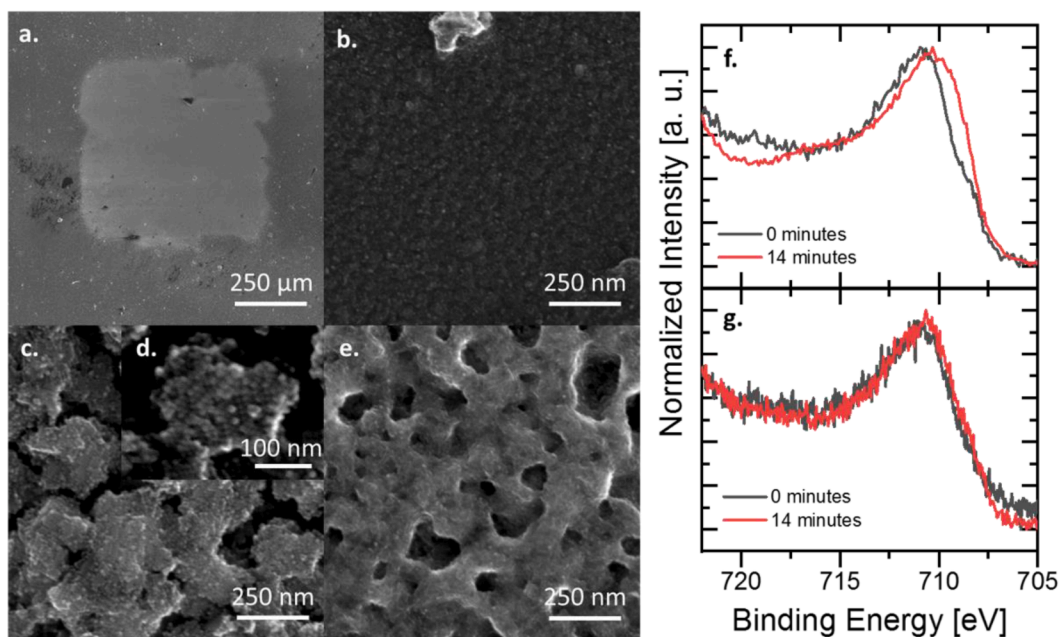


Figure 3. SEM pictures of the Zn(Sq) nanoparticles after acquisitions made in one spot with multiple Ar-GCIB sputtering with corresponding XPS results. (a) sputtered area, with the square of $400 \mu\text{m}$ by $400 \mu\text{m}$ showing the area where X-ray beam was directed; (b) Ar-GCIB sputtered area without the measurement taken (no X-ray acting onto the nanoparticles); (c) nanoparticles before sputtering with visible layers made of the nanoparticles (inset d); (e) nanoparticles after sputtering and the X-ray radiation affecting them, without visible rows of the nanoparticles; (f) Normalized Fe 2p XPS spectra for Zn(Sq) nanoparticles not sputtered and after 14 minutes of sputtering in the Single-Spot Procedure (corresponding to the c. and e. pictures, respectively); (g) Normalized Fe 2p XPS spectra for Zn(Sq) nanoparticles sputtered following the Spot-by-Spot Cluster Procedure.

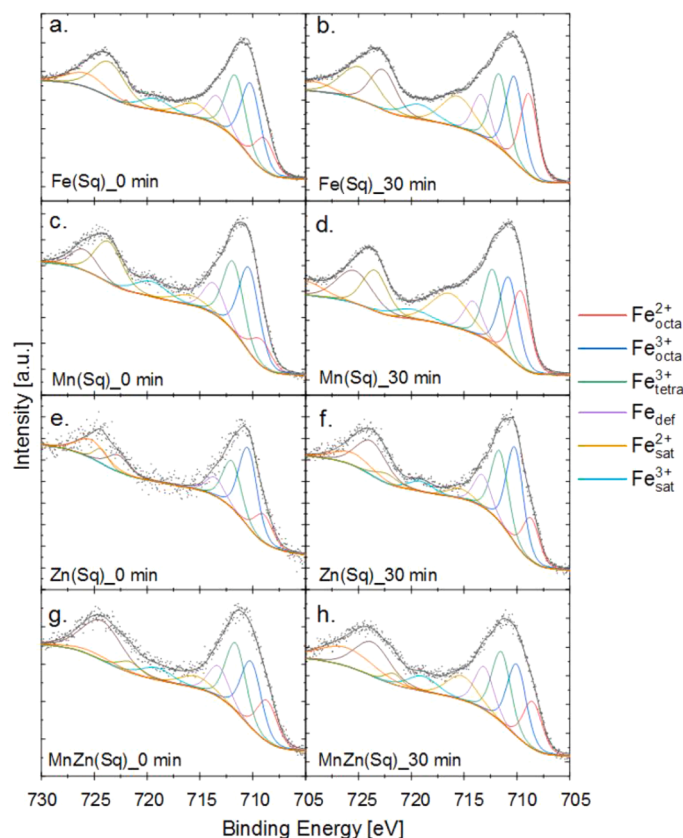


Figure 4. The XPS spectra of Fe 2p regions before and after sputtering (left and right side, respectively) with Ar-GCIB for Fe(Sq) and three other ferrites.

the metal oxide nanoparticles.

On the other hand, the Zn(Sq) nanoparticles (Figure 4 e, f) show differences in the comparison to the Fe(Sq) and Mn(Sq). Zn^{2+} ions tend to occupy the tetrahedral interstices and change the spinel structure from inverse to normal [27]. In the Zn(Sq) the content of zinc atoms is deficient to obtain stoichiometric zinc ferrite with normal spinel structure, hence a mixed structure should be observed. Here, the Zn^{2+} is believed to occupy the tetrahedral interstices with the $\text{Fe}^{2+}_{\text{octa}}$ line still present, though with very little intensity. The difference between Fe(Sq) or Mn(Sq) and Zn(Sq) is the little to no sign of the feature characteristic for the magnetite: no difference in the intensities of the lines in the satellite region is observed during cluster sputtering. This implies that the iron-rich phase is made mostly of maghemite or hematite. All of the presented results, with the addition of only small alterations in the Zn and Fe content during sputtering (Figure 5 d, e) imply that the presence of the zinc atoms in the structure allows obtaining a homogenous product with unchanging structure throughout the nanoparticle.

The last type of analyzed nanoparticles is mixed ferrite of manganese and zinc (MnZn(Sq), Figure 4 g, h), which both act as the dopants to the iron oxide. The spectrum shows similarities to both zinc and manganese ferrite samples. The overall content of dopants in the nanoparticles (4% and 6.5% for zinc and manganese, respectively) and the ratio of iron species, stays the same regardless of sputtering (Figure 5 f, g). On the other hand, the iron content increase from 7.3 to 11.0% and the shape of the Fe 2p spectrum alters during the cluster sputtering. The FWHMs and the binding energies for manganese lines are the same for Mn(Sq) and MnZn(Sq), same as FWHM for zinc when comparing to Zn(Sq). The main difference is the presence of additional low-intensity line in the Zn 2p spectrum suggesting that manganese occupy the same interstices for both types of nanoparticles while zinc is in more than one state when other dopants are added to the structure of the nanoparticles (Figure S3 and S4 in ESI).

4. Conclusions

In the presented study, a thorough analysis of the impact of X-ray radiation and the two different types of sputtering on the iron oxide and three different ferrites was conducted. The X-ray radiation does not have any measurable influence on the macroscopic iron oxide single crystal, but if the sample is made of the nanoparticles and the gas cluster sputtering is used some alterations of the structure are visible. Additionally, the use of monoatomic sputtering results in the reduction of the iron oxidation state and the alteration of the oxide structure even in the macroscopic single crystal. As a result of these observations, the original technique is proposed to ensure no damage to the sample's structure. Moreover, we proved, that depending on the substituting ion, the structure of the ferrite nanoparticle alters significantly. The doping with zinc results in the mixed spinel structure almost without Fe^{2+} . When manganese is used as the dopant, it is present in at least two states, with a decreasing amount of manganese in the core of the nanoparticles. Finally, when both proposed elements are introduced into the structure zinc behaves differently, and occupies more than one state. Those findings are a result of the usage of gas cluster ion sputtering combined with the X-ray Spot-by-Spot Cluster Procedure, which ensures very low impact to the structure, with the delicate removal of the subsequent layers of the sample.

CRedit authorship contribution statement

R. Wirecka: Conceptualization, Methodology, Resources, Investigation, Data curation, Writing – original draft, Visualization, Project administration. **D. Lachowicz:** Methodology, Resources, Writing – review & editing. **K. Berent:** Formal analysis. **M.M. Marzec:** Conceptualization, Writing – review & editing. **A. Bernasik:** Conceptualization, Writing – review & editing, Supervision.

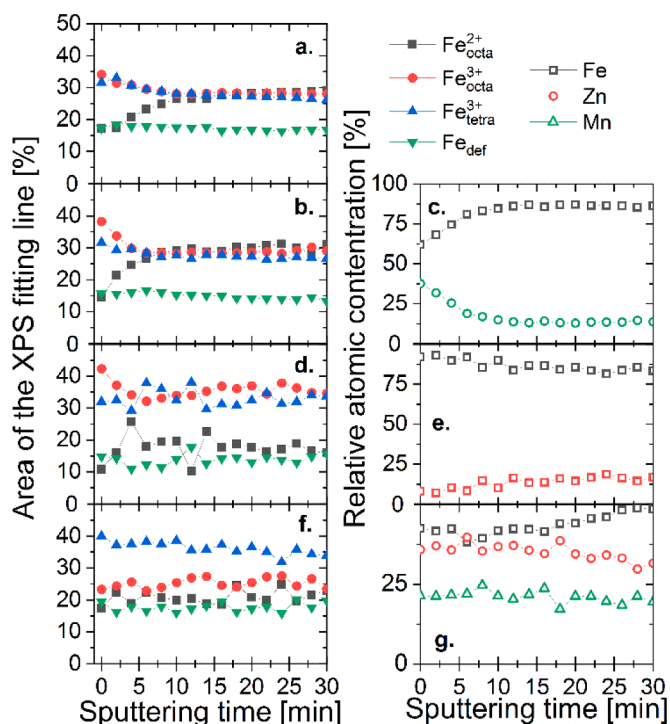


Figure 5. Graphs representing the differences in the areas of the lines after fitting of the XPS spectra with corresponding atomic concentration for the iron and the dopants in the nanoparticles; areas are normalized to the sum of four lines equivalent to 100%; (a.) results of the Fe(Sq) fitting, showing almost ideal 1:1:1 ratio of the $\text{Fe}^{2+}_{\text{octa}}:\text{Fe}^{3+}_{\text{octa}}:\text{Fe}^{3+}_{\text{tetra}}$ lines; (b. and c.) results for the Mn (Sq) nanoparticles, showing similarities with the Fe(Sq) nanoparticles in the areas of the fitted lines, additionally, (c) shows the stabilization in the concentration of the dopant after 10 minutes of Ar-GCIB sputtering; (d. and e.) data concerning Zn(Sq) showing lower intensity of the $\text{Fe}^{2+}_{\text{octa}}$ line suggesting the normal or mixed spinel structure of the nanoparticles; (f. and g.) percentages related to MnZn(Sq) showing the highest intensity for the $\text{Fe}^{3+}_{\text{tetra}}$ line and almost stable concentration of the dopants irrespective to the time of sputtering.

Declaration of Competing Interest

The authors declare that they have no known competing financial interests or personal relationships that could have appeared to influence the work reported in this paper.

Acknowledgments

This research and RW were partly supported by the EU Project POWR.03.02.00-00-1004/16.

Supplementary materials

Supplementary material associated with this article can be found, in the online version, at [doi:10.1016/j.surfin.2022.101865](https://doi.org/10.1016/j.surfin.2022.101865).

References

- D. Lachowicz, W. Górka, A. Kmita, A. Bernasik, J. Żukrowski, W. Szczerba, M. Sikora, C. Kapusta, S. Zapotoczny, Enhanced hyperthermic properties of biocompatible zinc ferrite nanoparticles with a charged polysaccharide coating, *J. Mater. Chem. B* 7 (2019) 2962–2973, <https://doi.org/10.1039/C9TB00029A>.
- S. Rasheed, R.A. Khan, F. Shah, B. Ismail, J. Nisar, S.M. Shah, A. Rahim, A.R. Khan, Enhancement of electrical and magnetic properties of cobalt ferrite nanoparticles by co-substitution of Li-Cd ions, *J. Magn. Magn. Mater.* 471 (2019) 236–241, <https://doi.org/10.1016/J.JMMM.2018.09.073>.
- M. Rivero, A. del Campo, A. Mayoral, E. Mazarío, J. Sánchez-Marcos, A. Muñoz-Bonilla, Synthesis and structural characterization of $\text{Zn}_x\text{Fe}_{3-x}\text{O}_4$ ferrite nanoparticles obtained by an electrochemical method, *RSC Adv* 6 (2016) 40067–40076, <https://doi.org/10.1039/C6RA04145K>.
- R. Sagayaraj, S. Aravazhi, C. Selva kumar, S. Senthil kumar, G. Chandrasekaran, Tuning of ferrites ($\text{Co}_x\text{Fe}_{3-x}\text{O}_4$) nanoparticles by co-precipitation technique, *SN Appl. Sci.* 2019 13 (1) (2019) 1–11, <https://doi.org/10.1007/S42452-019-0244-7>.
- L. Ajroudi, N. Mliki, L. Bessais, V. Madigou, S. Villain, C. Leroux, Magnetic, electric and thermal properties of cobalt ferrite nanoparticles, *Mater. Res. Bull.* 59 (2014) 49–58, <https://doi.org/10.1016/j.materresbull.2014.06.029>.
- W. Zhao, Z. Liu, P. Wei, Q. Zhang, W. Zhu, X. Su, X. Tang, J. Yang, Y. Liu, J. Shi, Y. Chao, S. Lin, Y. Pei, Magnetolectric interaction and transport behaviours in magnetic nanocomposite thermoelectric materials, *Nat. Nanotechnol.* 12 (2017) 55–60, <https://doi.org/10.1038/nnano.2016.182>.
- S. Akbayrak, S. Özkaz, Cobalt ferrite supported platinum nanoparticles: Superb catalytic activity and outstanding reusability in hydrogen generation from the hydrolysis of ammonia borane, *J. Colloid Interface Sci.* 596 (2021) 100–107, <https://doi.org/10.1016/J.JCIS.2021.03.039>.
- S. Shatooti, M. Mozaffari, G. Reiter, D. Zahn, S. Dutz, Heat dissipation in Sm^{3+} and Zn^{2+} co-substituted magnetite ($\text{Zn}_{0.1}\text{Sm}_x\text{Fe}_{2.9-x}\text{O}_4$) nanoparticles coated with citric acid and pluronic F127 for hyperthermia application, *Sci. Rep.* 11 (2021) 1–14, <https://doi.org/10.1038/s41598-021-96238-2>.
- J.M. Silveyra, E. Ferrara, D.L. Huber, T.C. Monson, Soft magnetic materials for a sustainable and electrified world, *Science* 362 (80-) (2018) 1–9, <https://doi.org/10.1126/science.aao0195>.
- N. Shah, T. Rehan, X. Li, H. Tetik, G. Yang, K. Zhao, D. Lin, Magnetic aerogel: an advanced material of high importance, *RSC Adv* 11 (2021) 7187–7204, <https://doi.org/10.1039/d0ra10275j>.
- F.A. Garcés-Pineda, M. Blasco-Ahicart, D. Nieto-Castro, N. López, J.R. Galán-Mascarós, Direct magnetic enhancement of electrocatalytic water oxidation in alkaline media, *Nat. Energy* 4 (2019) 519–525, <https://doi.org/10.1038/s41560-019-0404-4>.
- S. Chakrabarty, A. Dutta, M. Pal, Enhanced magnetic properties of doped cobalt ferrite nanoparticles by virtue of cation distribution, *J. Alloys Compd.* 625 (2015) 216–223, <https://doi.org/10.1016/j.jallcom.2014.10.179>.
- C. Zou, C. Hu, H. Zhou, S. Li, X. Luo, J. He, C. Yuan, Structure Modulation in Confined Nanoparticles: The Role of the Strain Gradient, *J. Phys. Chem. C* 124 (2020) 21810–21817, <https://doi.org/10.1021/acs.jpcc.0c06516>.
- C. Dong, J. Pichaandi, T. Regier, F.C.J.M. Van Veggel, Nonstatistical Dopant Distribution of Ln 3+-Doped NaGdF 4 Nanoparticles, *J. Phys. Chem. C* 115 (2011) 15950–15958, <https://doi.org/10.1021/jp206441u>.
- X. Xu, C. Clarke, C. Ma, G. Casillas, M. Das, M. Guan, D. Liu, L. Wang, A. Tadich, Y. Du, C. Ton-That, D. Jin, Depth-profiling of Yb3+ sensitizer ions in NaYF4 upconversion nanoparticles, *Nanoscale* 9 (2017) 7719–7726, <https://doi.org/10.1039/c7nr01456b>.
- W. Yuan, Z. Lu, H. Wang, C.M. Li, Sacrificial polymer thin-film template with tunability to construct high-density Au nanoparticle arrays and their refractive index sensing, *Phys. Chem. Chem. Phys.* 15 (2013) 15499–15507, <https://doi.org/10.1039/c3cp25816b>.
- K. Ridier, D. Aureau, B. Bérini, Y. Dumont, N. Keller, J. Vigneron, A. Etcheberry, A. Fouchet, Enhanced Depth Profiling of Perovskite Oxide: Low Defect Levels Induced in SrTiO3 by Argon Cluster Sputtering, *J. Phys. Chem. C* 120 (2016) 21358–21363, <https://doi.org/10.1021/acs.jpcc.6b04007>.
- Z. Postawa, B. Czerwinski, M. Szczyzyk, E.J. Smiley, N. Winograd, B.J. Garrison, Microscopic Insights into the Sputtering of Ag(111) Induced by C 60 and Ga Bombardment, (2004). doi:10.1021/jp049936a.
- R. Grilli, R. Simpson, C.F. Mallinson, M.A. Baker, Comparison of Ar+ Monoatomic and Cluster Ion Sputtering of Ta2O5 at Different Ion Energies, by XPS: Part 1 - Monoatomic Ions, *Surf. Sci. Spectra* 21 (2014) 50–67, <https://doi.org/10.1116/11.20140701>.
- R. Grilli, R. Simpson, C.F. Mallinson, M.A. Baker, Comparison of Ar+ Monoatomic and Cluster Ion Sputtering of Ta2O5 at Different Ion Energies, by XPS: Part 2 - Cluster Ions, *Surf. Sci. Spectra* 21 (2014) 68–83, <https://doi.org/10.1116/11.20140702>.
- D. Aureau, K. Ridier, B. Bérini, Y. Dumont, N. Keller, J. Vigneron, M. Bouttemy, A. Etcheberry, A. Fouchet, Advanced analysis tool for X-ray photoelectron spectroscopy profiling: Cleaning of perovskite SrTiO3 oxide surface using argon cluster ion source, *Thin Solid Films* 601 (2016) 89–92, <https://doi.org/10.1016/j.tsf.2015.11.017>.
- Z. Postawa, L. Rzeznik, R. Paruch, M.F. Russo, N. Winograd, B.J. Garrison, Depth profiling by cluster projectiles as seen by computer simulations, *Surf. Interface Anal.* 43 (2011) 12–15, <https://doi.org/10.1002/SIA.3417>.
- Z. Postawa, R. Paruch, L. Rzeznik, B.J. Garrison, Dynamics of large Ar cluster bombardment of organic solids, *Surf. Interface Anal.* 45 (2013) 35–38, <https://doi.org/10.1002/SIA.4927>.
- T. Conard, C. Fleischmann, R. Havelund, A. Franquet, C. Poleunis, A. Delcorte, W. Vandervorst, Inorganic material profiling using Ar n+ cluster: Can we achieve high quality profiles? *Appl. Surf. Sci.* 444 (2018) 633–641, <https://doi.org/10.1016/j.apsusc.2018.02.159>.
- D. Lachowicz, R. Wirecka, W. Górka-Kumik, M.M. Marzec, M. Gajewska, A. Kmita, J. Żukrowski, M. Sikora, S. Zapotoczny, A. Bernasik, Gradient of zinc content in core-shell zinc ferrite nanoparticles-precise study on composition and magnetic properties, *Phys. Chem. Chem. Phys.* 21 (2019) 23473–23484, <https://doi.org/10.1039/c9cp03591e>.
- D. Baer, M. Engelhard, D. Gaspar, Challenges in Applying Surface Analysis Methods to Nanoparticles and Nanostructured Materials, *J. Surf. Anal.* 12 (2005) 101–108.
- M. Wen, Q. Li, Y. Li, Magnetic, electronic and structural properties of $\text{Zn}_x\text{Fe}_{3-x}\text{O}_4$, *J. Electron Spectros. Relat. Phenomena* 153 (2006) 65–70, <https://doi.org/10.1016/j.jespec.2006.06.002>.

- [28] D.D. Hawn, B.M. DeKoven, Deconvolution as a correction for photoelectron inelastic energy losses in the core level XPS spectra of iron oxides, *Surf. Interface Anal.* 10 (1987) 63–74, <https://doi.org/10.1002/sia.740100203>.
- [29] P. Mills, J.L. Sullivan, A study of the core level electrons in iron and its three oxides by means of x-ray photoelectron spectroscopy, *J. Phys. D Appl. Phys.* 16 (1983) 723–732, <https://doi.org/10.1088/0022-3727/16/5/005>.
- [30] A.P. Grosvenor, B.A. Kobe, M.C. Biesinger, N.S. McIntyre, Investigation of multiplet splitting of Fe 2p XPS spectra and bonding in iron compounds, *Surf. Interface Anal.* 36 (2004) 1564–1574, <https://doi.org/10.1002/sia.1984>.
- [31] D. Wilson, M.A. Langell, XPS analysis of oleylamine/oleic acid capped Fe₃O₄ nanoparticles as a function of temperature, *Appl. Surf. Sci.* 303 (2014) 6–13, <https://doi.org/10.1016/j.apsusc.2014.02.006>.
- [32] M.C. Biesinger, B.P. Payne, A.P. Grosvenor, L.W.M. Lau, A.R. Gerson, R.S.C. Smart, Resolving surface chemical states in XPS analysis of first row transition metals, oxides and hydroxides: Cr, Mn, Fe, Co and Ni, *Appl. Surf. Sci.* 257 (2011) 2717–2730, <https://doi.org/10.1016/j.apsusc.2010.10.051>.
- [33] T. Radu, C. Iacovita, D. Benea, R. Turcu, X-Ray Photoelectron Spectroscopic Characterization of Iron Oxide Nanoparticles, *Appl. Surf. Sci.* 405 (2017) 337–343, <https://doi.org/10.1016/j.apsusc.2017.02.002>.

Electronic Supplementary Information

Ion distribution in Iron Oxide, Zinc and Manganese Ferrite nanoparticles studied by XPS combined with Argon Gas Cluster Ion Beam sputtering

R. Wirecka^{a,b*}, D. Lachowicz^b, K. Berent^b, M. M. Marzec^b, A. Bernasik^{a,b}

^a Faculty of Physics and Applied Computer Science, AGH University of Science and Technology, A. Mickiewicza Av. 30, 30-059 Cracow, Poland

^b Academic Centre for Materials and Nanotechnology, AGH University of Science and Technology, A. Mickiewicza Av. 30, 30-059 Cracow, Poland

*Corresponding author e-mail address: roma.wirecka@fis.agh.edu.pl

Table S1. Atomic concentration for the Zn(Sq) sample following Single-Spot Procedure

Sputtering time [min]	Atomic concentration [%]				
	C 1s	O 1s	Fe 2p	Zn 2p	Si 2p
0	41.0	39.8	14.2	1.8	3.2
2	38.2	41.4	16.0	1.7	2.7
4	26.5	46.6	21.9	1.8	3.2
6	13.5	51.8	27.7	1.7	5.3
8	7.1	53.5	32.2	1.7	5.5
10	7.3	53.5	31.8	1.7	5.7
12	6.2	52.2	34.2	1.7	5.7
14	5.0	54.8	34.3	1.8	4.2

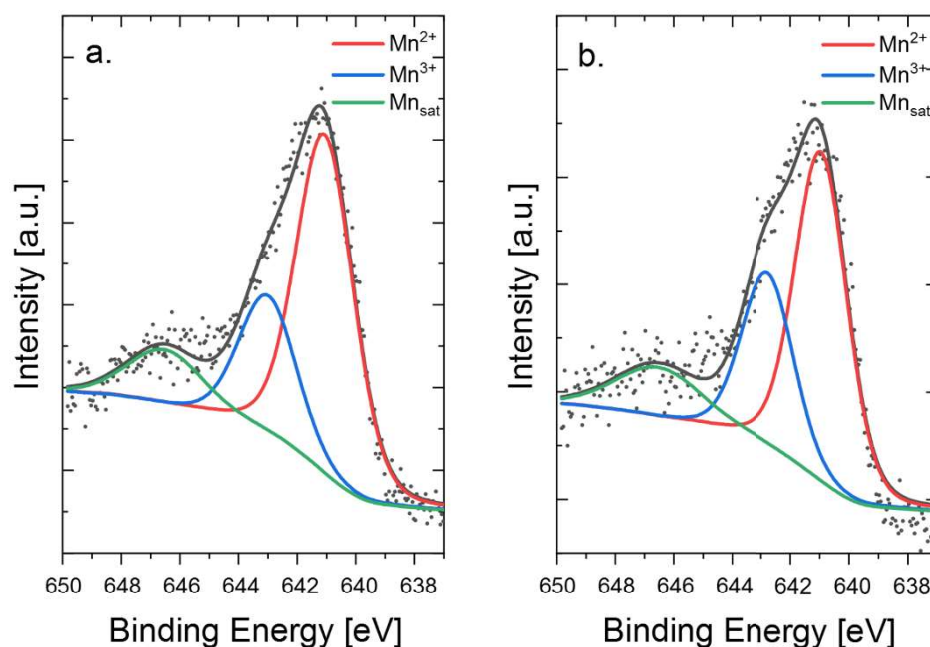


Figure S1. Mn $2p_{3/2}$ XPS spectra for the Mn(Sq) nanoparticles before sputtering (a) and after 30 minutes of sputtering (b) following the Spot-by-Spot Cluster Procedure.

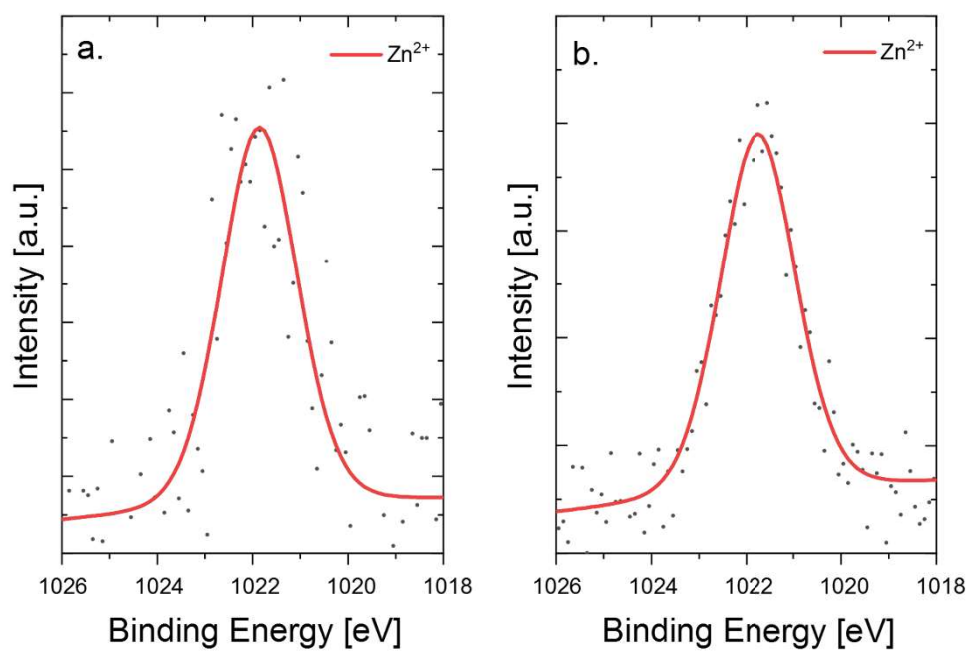


Figure S2. Zn 2p XPS spectra for Zn(Sq) nanoparticles before sputtering (a) and after 30 minutes of sputtering (b) following the Spot-by-Spot Cluster Procedure.

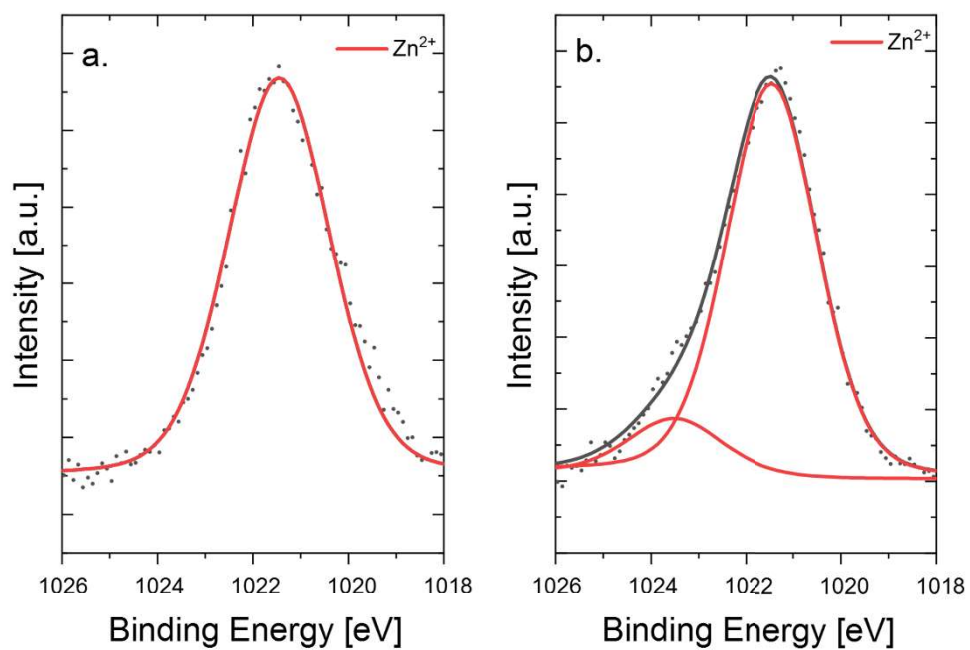


Figure S3. Zn 2p XPS spectra for MnZn(Sq) nanoparticles before sputtering (a) and after 30 minutes of sputtering (b) following the Spot-by-Spot Cluster Procedure.

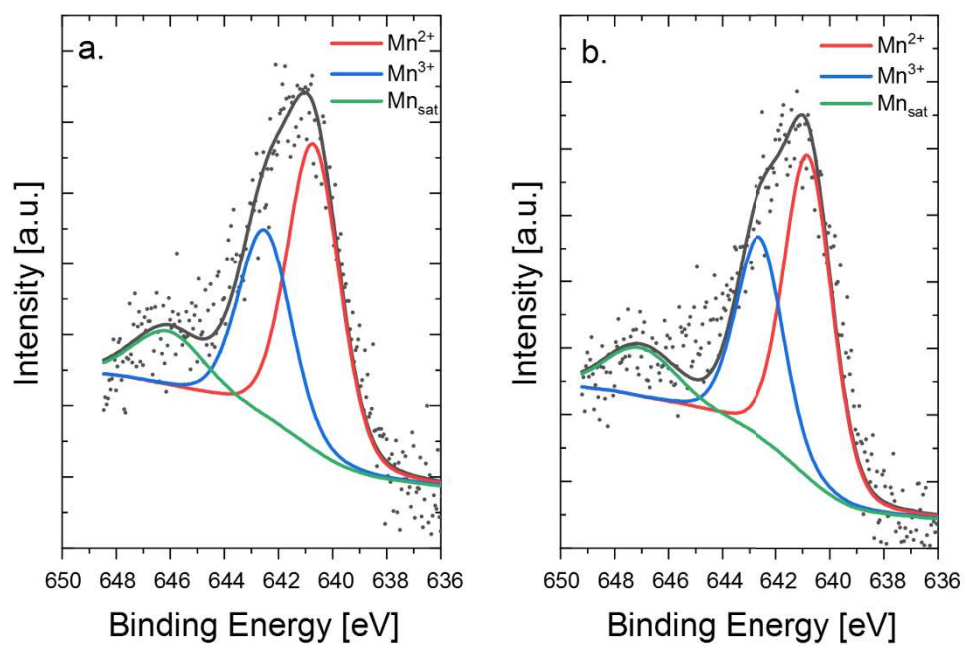


Figure S4. Mn 2p_{3/2} XPS spectra for the MnZn(Sq) nanoparticles before sputtering (a) and after 30 minutes of sputtering (b) following the Spot-by-Spot Cluster Procedure.

Table S2. Summary of the fitting parameters for Fe 2p spectra for all measured nanoparticles before and after 30 minutes of sputtering following Spot-by-Spot Procedure

Sample	Line	Sputtering time 0 min			Sputtering time 30 min		
		Binding energy [eV]	FWHM [eV]	%Area	Binding energy [eV]	FWHM [eV]	%Area
Fe(Sq)	Fe ²⁺ _{octa}	708.9	2.1	10.6	708.9	2.0	17.9
	Fe ³⁺ _{octa}	710.2	2.1	21.2	710.2	2.0	17.3
	Fe ³⁺ _{tetra}	711.5	2.1	19.6	711.5	2.0	16.1
	Fe _{def}	713.2	2.1	10.8	713.2	2.0	10.4
	Fe ²⁺ _{sat}	715.7	3.1	6.5	715.7	3.4	9.5
	Fe ³⁺ _{sat}	719.4	3.1	4.9	719.4	3.4	3.2
Zn(Sq)	Fe ²⁺ _{octa}	709.0	2.4	7.9	708.8	2.3	10.7
	Fe ³⁺ _{octa}	710.2	2.4	30.7	710.1	2.3	23.3
	Fe ³⁺ _{tetra}	711.6	2.4	23.2	711.4	2.3	22.6
	Fe _{def}	713.4	2.4	10.8	713.3	2.3	10.6
	Fe ²⁺ _{sat}	-	-	0.0	715.5	2.9	2.6
	Fe ³⁺ _{sat}	-	-	0.0	719.2	2.9	3.7
Mn(Sq)	Fe ²⁺ _{octa}	709.0	2.2	9.2	708.7	2.1	16.9
	Fe ³⁺ _{octa}	710.1	2.2	24.5	709.9	2.1	15.8
	Fe ³⁺ _{tetra}	711.6	2.2	20.2	711.3	2.1	14.5
	Fe _{def}	713.5	2.2	10.1	713.1	2.1	7.2
	Fe ²⁺ _{sat}	715.7	3.3	4.6	715.4	4.1	13.2
	Fe ³⁺ _{sat}	719.4	3.3	6.6	719.1	4.1	3.6
MnZn (Sq)	Fe ²⁺ _{octa}	708.6	2.3	10.4	708.7	2.3	14.1
	Fe ³⁺ _{octa}	709.9	2.3	14.0	710.0	2.3	14.5
	Fe ³⁺ _{tetra}	711.2	2.3	24.0	711.3	2.3	20.9
	Fe _{def}	713.1	2.3	11.7	713.2	2.3	12.2
	Fe ²⁺ _{sat}	715.3	3.8	6.5	715.4	3.3	6.8
	Fe ³⁺ _{sat}	719.0	3.8	4.6	719.1	3.3	4.5

Table S3. Summary of the fitting parameters for zinc and manganese in the Zn(Sq), Mn(Sq) and MnZn(Sq) samples

Sample	Line	Sputtering Time 0 min			Sputtering Time 30 min		
		Binding Energy [eV]	FWHM [eV]	%Area	Binding Energy [eV]	FWHM [eV]	%Area
Zn(Sq)	Zn ²⁺	1021.8	1.9	100	1021.8	1.9	100
MnZn(Sq)	Zn ²⁺	1021.5	2.5	100	1021.5	2.3	88.0
					1023.5	2.3	12.0
Mn(Sq)	Mn ²⁺	641.1	2.3	61.8	641.0	2.1	56.1
	Mn ³⁺	643.0	2.3	25.1	642.8	2.1	29.6
	Mn _{sat}	646.5	3.0	13.1	646.5	3.5	14.3
MnZn(Sq)	Mn ²⁺	640.7	2.3	53.7	640.8	2.1	53.9
	Mn ³⁺	642.5	2.3	33.0	642.6	2.1	33.5
	Mn _{sat}	646.1	3.1	13.3	647.0	3.1	12.5

Cite this: *J. Mater. Chem. C*, 2021,
9, 10453

The effect of shell modification in iron oxide nanoparticles on electrical conductivity in polythiophene-based nanocomposites†

Roma Wirecka,^a Mateusz M. Marzec,^b Marianna Marciszko-Wiąckowska,^b Maria Lis,^b Marta Gajewska,^b Elżbieta Trynkiewicz,^b Dorota Lachowicz^b and Andrzej Bernasik^{a,b}

In the field of organic electronics, the energy level alignment between the components of a device is crucial for its final performance. Improvement in the final properties can be achieved using hybrids made of organic and inorganic materials. In highly defected systems, like polymers or nanoparticles, every charge carrier matters, and the potential barriers or possible defects must be considered when designing a hybrid consisting of such components. However, the difference in the interface modification in such materials and its influence on final conductivity were never studied before. This paper shows how modification of the medium in iron oxide nanoparticle synthesis can increase the hole transportation efficiency without altering the morphology, magnetic properties, and chemical composition of the obtained nanoparticles. We found that a six-time increase of conductivity can be achieved, mainly due to the shift in the hole injection barrier which was reduced from 1.7 eV for pristine P3HT to 1 eV for materials made of nanoparticles and P3HT, and also by lack of the diffusion barrier between the nanoparticles and conducting polymer. Until now, research on such systems has mainly focused on the dispersity and stability of nanoparticles, which led to the isolation of components in the final product caused by capping agents at the surface of the additive. Our results demonstrate how surface functionalization of iron oxide nanoparticles can reduce the barrier at the nanoparticle/polythiophene interface and influence the energy level alignment, hence improving the electrical conductivity of the final material.

Received 24th June 2021,
Accepted 3rd July 2021

DOI: 10.1039/d1tc02949e

rsc.li/materials-c

Introduction

Composites based on magnetic oxide nanoparticles and conducting polymers are in demand for potential applications as microwave absorbers,^{1,2} electromagnetic shielding materials,³ or as a part of organic solar cells.^{4,5} Additionally, due to the semiconducting properties of some metal oxides, they can potentially contribute to the overall electrical properties of hybrid materials, providing basics for thin, flexible, and cheap organic electronic devices.^{6–8}

Hybrid materials consisting of nanoparticles and conducting polymers can be obtained in four different ways: mixing polymer and nanoparticles,^{9,10} *in situ* synthesis of nanoparticles in the

polymer solution,¹¹ *in situ* polymerization in the presence of nanoparticles¹² and synthesis of polymer and nanoparticles simultaneously.¹³ The first two proposed methods allow studying the changes of electrical properties in the obtained materials induced by the alteration of the interface between the polymer and nanoparticles, while the two latter methods allow the enhancement of polymer properties by control over the length and polydispersity of polymers and the overall architecture of the final composite.

The interface and energy level alignment plays a crucial role in the final performance of organic electronic devices.^{14–16} By adjusting the energy levels of the subsequent layers of the device, the efficiency of charge injection and collection can be significantly enhanced, while geminate charge recombination may potentially be reduced.¹⁷ One way of modifying, hence, adjusting the energy level alignment, is through the use of metal and metal oxide nanoparticles.^{5,18,19} Additionally, by creating a conduction path directly in the active layer by nanoparticles, improvement of conductivity of the electronic device can be obtained directly.²⁰ Within the conduction path

^a AGH University of Science and Technology, Faculty of Physics and Applied Computer Science, al. A. Mickiewicza 30, 30-059 Cracow, Poland.

E-mail: roma.wirecka@fis.agh.edu.pl

^b AGH University of Science and Technology, Academic Centre for Materials and Nanotechnology, al. A. Mickiewicza 30, 30-059 Cracow, Poland

† Electronic supplementary information (ESI) available. See DOI: 10.1039/d1tc02949e

and subsequent energy level alignment lies the interface of the nanoparticles and polymer matrix; this can be seen as the most important part for the successful fabrication of composites with enhanced conduction properties. The synthesis of nanoparticles ends with the obtainment of a core-shell type structure in which the core (nanoparticle) is covered with a capping agent typically made of large organic molecules.^{21–23} This architecture prevents undesirable aggregation of nanoparticles but on the other hand introduces a few nanometer-thick insulating layer between the polymer matrix and nanoparticles which in turn blocks the undisturbed electron/hole flow.²⁴

This study presents the synthesis of iron oxide nanoparticles covered with two different shells: an insulating shell made of a capping agent and a conducting shell made of poly(3-hexylthiophene) (P3HT). Second, we propose two hybrid materials made of nanoparticles mixed with P3HT. In the final part of this study, an electrical conductivity model based on chemical characterization of the obtained materials, conductivity measurements and energy level alignment of the created materials is proposed.

Results and discussion

Morphology and crystallographic structure

The morphology with the corresponding histograms of the synthesized nanoparticles is presented in Fig. 1. Both types of synthesized nanoparticles show aggregation, and a similar diameter of around 10 nm with low polydispersity. It is possible that even though the capping agent was used to stabilize SPION(Sq), the magnetic interactions between the particles were higher than the stabilizing factor. Due to the lack of a capping agent in SPION(P3HT) synthesis, the obtained nanoparticles are of irregular shape and have a lower degree of crystallinity, compared to the particles synthesized with squelane in the reactive mixture.

To learn more about the crystallographic structure of the nanoparticles, XRD analysis was conducted. Observed peak broadening can be ascribed to the small crystallite size of the nanoparticles. Both types of synthesized nanoparticles possess a cubic inverse spinel structure, $Fd\bar{3}m$ group (JCPDS no. 98-015-8741). On the basis of the Rietveld refinement, the lattice constant of

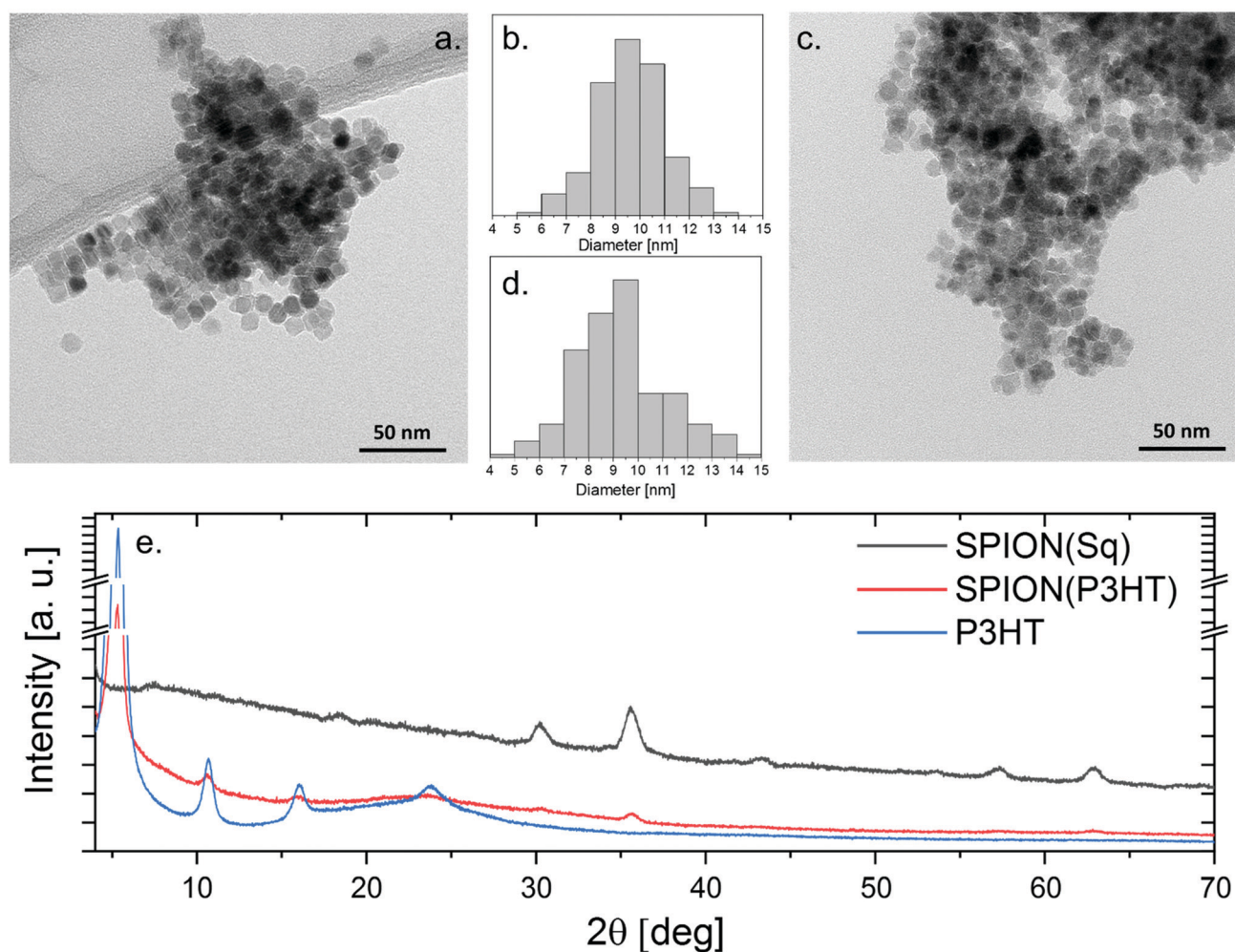


Fig. 1 TEM micrographs of the synthesized nanoparticles with the corresponding histograms are presented. For SPION(Sq) (a and b), the average diameter was calculated to be 9.3 ± 1.9 nm and for SPION(P3HT) (c and d) 9.6 ± 1.4 nm. At the bottom (e), XRD pattern for both types of nanoparticles can be found, showing characteristic peaks for the cubic inverse structure $Fd\bar{3}m$ group, with an additional diffractogram for pure P3HT.

SPION(Sq) is 8.34 Å, though in the case of SPION(P3HT) the intensity and the number of profound XRD peaks corresponding to Fe₃O₄ were not high enough for reliable Rietveld refinement. However, the lattice constant of SPION(P3HT) was calculated to be approx. 8.36 Å. Both values correspond well with the bulk lattice constant of 8.39 Å.²⁵ The average crystallite size was calculated using the Scherrer formula for the (113) crystalline plane and it was found to be 10.7 (FWHM = 0.933°) and 12.9 nm (FWHM = 0.785°) for SPION(Sq) and SPION(P3HT), respectively. This, combined with the TEM results, proves that nanoparticles are of single crystalline character.

Additional analysis was conducted for thin polymer films made from pure P3HT. The diffraction peaks at 5.5°, 10.7°, 16.0° and 23.8° were observed and ascribed to crystalline P3HT (100), (200), (300) and (010) planes, respectively.^{26,27} Furthermore, the same diffraction peaks were found in the diffractogram of SPION(P3HT), proving the presence of the polymer around the synthesized nanoparticles.

Magnetic properties

The magnetic behavior of SPION(P3HT), SPION(Sq) nanoparticles and unmodified P3HT was investigated using a vibrating sample magnetometer. The samples were measured as dried powders. Fig. 2a shows the *M*-*H* hysteresis loops of the three materials, which were recorded at 80 K using a field sweep rate of 1 mT s⁻¹. To study the changes in the magnetic properties of nanoparticles, additional *M*-*H* loops were recorded for 290 K and 440 K. Multiple factors determining the magnetic properties such as coercivity (*H*_c), saturation magnetization (*M*_s), remanence ratio (*M*_r/*M*_s), and blocking temperature (*T*_B) are shown in Table 1. Both nanoparticle samples depict open loops at a very low temperature, 80 K, with a slightly higher coercivity for SPION(P3HT) than SPION(Sq), which is equal to 32 mT and 20 mT, respectively. The existence of a polymer on the surface of magnetic oxide

Table 1 Summary of the magnetic characterization: coercivity (*H*_c), saturation magnetization (*M*_s) and remanence ratio (*M*_r/*M*_s)

	<i>H</i> _c [mT]	<i>M</i> _s [Am ² kg ⁻¹]			<i>M</i> _r / <i>M</i> _s [%]	<i>T</i> _B [K]
		80 K	290 K	440 K		
SPION(P3HT)	32	77.8	67.9	56.2	7.9	<80, 300, 320
SPION(Sq)	20	67.5	62.6	52.3	3.6	<80, 270

nanoparticles can possibly change the surface magnetic anisotropy leading to the enhancement of the surface spin disorientation.²⁸ However, despite this fact the saturation magnetization of SPION(P3HT) is noticeably higher compared to that of SPION(Sq). For P3HT powder, no magnetic response was observed, which is possibly limited by the apparatus resolution, but the weak ferromagnetic properties of P3HT were proven by Majumdar *et al.*²⁹ Such properties can possibly enhance the magnetic response of SPION(P3HT) which is visible as a higher *M*_s of the material. At higher temperatures (290 K, 440 K), the nature of magnetization of both the samples is typical for an ensemble of superparamagnetic nanoparticles, as evidenced by negligible coercivity and remanence (hysteresis loops can be found in ESI in Fig. S1†).

Fig. 2b shows the temperature dependence of magnetization, which is probed using the magnetic flux of 10 mT after zero field cooling (ZFC) and field cooling (FC). Both samples were measured under identical conditions. The temperature shift in the ZFC curve reveals that the blocking temperature of SPION(P3HT) is significantly higher than that of SPION(Sq). The blocking temperature allows determining the regime above which the ferromagnetic response is destroyed since the magnetic anisotropy energy barrier of single domain nanoparticles is overcome by thermal activation energy, leading to the fluctuation of magnetization typical for paramagnets. A flat maximum of ZFC and non-monotonic difference between FC and ZFC dependences suggest that some volumes of both the systems have several blocking temperatures.³⁰ Indeed, the plot of the temperature derivative of the difference between FC and ZFC profiles shows the maximum at approx. 270 K for SPION(Sq) as well as approx. 300 K and approx. 370 K for SPION(P3HT). These are attributed to the strongly coupled nanoparticles in the forms of nanoflower multicore particles.

Chemical structures

The first method applied to study the chemical structure of SPION(P3HT) was FT-IR spectroscopy (Fig. 3a). It allowed confirming the presence of both polythiophene and iron oxide in the final product. Peaks located at 2962, 2933 and 2853 cm⁻¹ can be ascribed to CH₂ out-of-plane mode, CH₂ in-plane mode and CH₃ asymmetry mode, respectively.^{31,32} Additionally, four peaks around 1410 cm⁻¹ belong to the vibration of a thiophene ring, which can be observed for both SPION(P3HT) and pure P3HT samples. The additional line at 560 cm⁻¹ in the SPION(P3HT) and SPION(Sq) spectra can be ascribed to the stretching vibration mode of O-Fe bonds in magnetic nanoparticles.³³ Such FT-IR results confirm the presence of iron oxide nanoparticles in the polymer matrix.

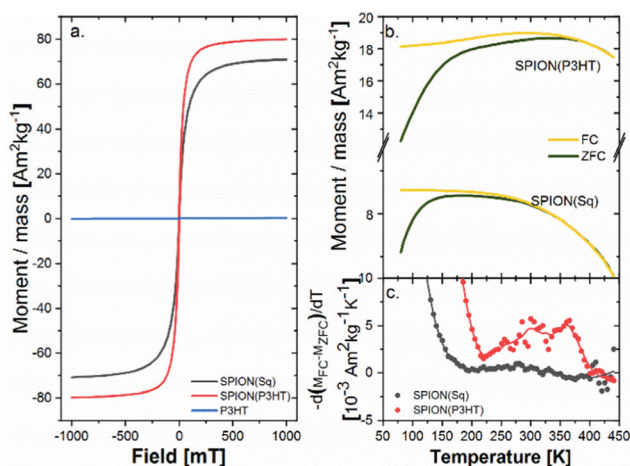


Fig. 2 (a) Magnetic hysteresis cycles for P3HT, SPION(P3HT) and SPION(Sq) measured at 80 K, (b) zero field cooled (ZFC) and field cooled (FC) magnetization curves as a function of temperature taken in an external magnetic field of 10 mT, (c) derivative of the difference between FC and ZFC as a function of temperature.

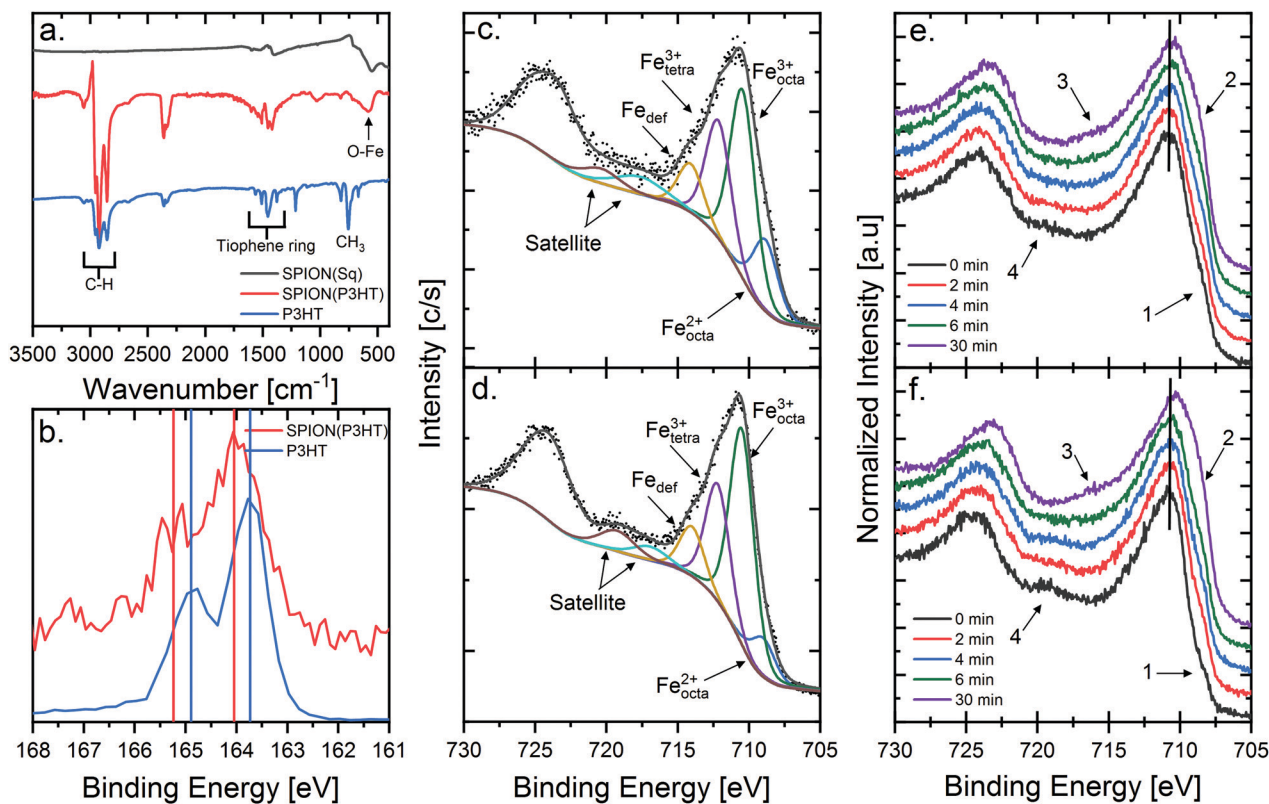


Fig. 3 (a) FT-IR spectra showing the presence of the polymer in SPION(P3HT) and iron oxide in both nanoparticle samples, (b) XPS S 2p spectra for SPION(P3HT) and pristine polymer showing a shift of 0.3 eV and suggesting coordinate bonding between iron and sulphur, (c and e) XPS Fe 2p spectra for SPION(Sq) before sputtering and after different times of Ar-GCIB sputtering, with characteristic features depicted in the figure, (d and f) XPS Fe 2p spectra for SPION(P3HT) before and after different times of Ar-GCIB sputtering.

To further analyze the structure of the obtained nanoparticles and their possible core-shell structure, XPS analysis of nanoparticles and the pristine polymer was conducted. The analysis of C 1s and S 2p regions allowed the investigation of possible changes in the polymer chemical structure and a thorough analysis of the Fe 2p region allowed checking how different synthesis media, thus nanoparticle coating, influence iron oxide formation.

The S 2p region in the SPION(P3HT) spectrum consists of two lines at 164.0 and 165.2 eV for S 2p_{3/2} and S 2p_{1/2}, respectively. In the case of P3HT, two peaks can be ascribed to sulphur with energies of 163.7 and 164.9 eV (Fig. 3b). The chemical shift between these two sulphur spectra implies that the coordinate bonding between iron atoms and sulphur from the thiophene ring may take place,³⁴ but no oxidation or other forms of degradation of the thiophene ring, as a result of synthesis, are observed. For the Fe 2p region, it was possible to distinguish six lines from which three were ascribed to Fe²⁺, Fe³⁺ in octahedral, and Fe³⁺ in the tetrahedral interstices, one to defected iron atoms which are mostly located at the surface of nanoparticles and two satellite peaks were ascribed to Fe²⁺ and Fe³⁺ (Fig. 3c and d).

The second part of XPS measurements was based on XPS analysis combined with argon gas cluster ion beam sputtering (Ar-GCIB). It allowed studying how different coatings of

nanoparticles influence iron oxide formation by observing the spectra in the subsequent layers of both types of synthesized nanoparticles. Ar-GCIB sputtering is characterized by meager energy impact on every atom (in this case 4 eV per atom) in the measured sample, which limits chemical state alterations.^{35,36} One thing that was shown in the Fe 2p region was the core-shell character of the obtained nanoparticles. Measurements were taken after every 2 minutes of cluster sputtering. To show the possible changes in the chemical state of iron atoms with in-depth analysis of the samples, five different spectra were chosen: after 0, 2, 4, 6 and 30 minutes of sputtering (Fig. 3e and f). There were 3 characteristic features in the Fe 2p spectra that were observed during sputtering that proved the variation in the structure of nanoparticles.³⁷ First, at the early stages of sputtering (up to 6 minutes), the intensity of Fe²⁺ lines in octahedral interstices is very low which suggests the hematite or maghemite shell of nanoparticles, and although when its intensity gradually increases, it shows that the core of nanoparticles consists mainly of magnetite. The second change occurs for satellite peaks. There is an increase of satellite peak related to Fe²⁺ which is a characteristic of magnetite. Additionally, the maximum of the Fe 2p_{3/2} peak shifts towards lower energies after every 2 minutes of sputtering, which shows that the iron oxide structure in nanoparticles shifts from α -, γ -Fe₂O₃ to Fe₃O₄.

When comparing the XPS spectra of iron, the change in the iron state in SPION(P3HT) is more prominent. The characteristic line of Fe^{2+} in octahedral interstices (709.0 eV) has a very low intensity in the non-sputtered sample, but after 30 minutes of cluster sputtering, the intensity of that line severely increases. This may come from a thick polymer shell which covers the nanoparticles, so before sputtering, the XPS spectrum of iron comes from the outermost layer of nanoparticles in comparison to that of the SPION(Sq) sample.

Analysis of the C 1s region confirmed the presence of squalane and dodecanoic acid in SPION(Sq) and the presence of the polymer shell in SPION(P3HT) samples. In the case of the SPION(Sq) sample, the carbon content decreased during sputtering from 25% to 4.3% atomic concentration. The most visible change occurred between 0 and 6 minutes of sputtering, when the concentration decreases to 8% and after that steadily decreases to 4.3%. The reason why it is not reaching 0% lays in the carbon shell, not only at the top of the nanoparticles, but also between adjacent nanospheres. In the case of the SPION(P3HT) sample, the carbon content reaches almost 50% before sputtering and decreases to 12% steadily for 30 minutes of sputtering (XPS spectra for the C 1s region and carbon content data are presented in the ESI† in Fig. S2 and S3, respectively). Such a high amount of carbon in the sample may come from a thick polymer layer surrounding the nanoparticles in the sample which proves the statement made in the previous paragraph. Additionally, the carbon layer indirectly protects the iron core of the studied nanoparticles from a possible negative impact of irradiation during sputtering and measurement itself, therefore more prominent change of the iron state in the SPION(P3HT) sample should not be connected to the degradation of the chemical structure during XPS measurements, but only as a result of different environments during synthesis.

Conductivity and UPS measurements

Fig. 4 presents three different I - V characteristics observed for P3HT, SPION(Sq) and SPION(P3HT). Measurements were conducted either under dark conditions (Fig. 4a) or illumination (Fig. 4b). It is clearly visible that nanoparticles covered with the capping agent cannot conduct electricity, but when squalane is replaced by a thin polymer shell, the conductivity in the dark increases dramatically in comparison to pure P3HT. The increase of conductivity in the SPION(P3HT) sample, in comparison to that of the pristine polymer, can be explained by the possible p-type of semiconductivity of magnetic nanoparticles.³⁸ Semiconductivity may originate from iron deficiency in octahedral interstices which was suggested by XPS and XRD measurements. In the measured films, p-type nanoparticles are connected directly to the p-type polymer, which in this example is P3HT, resulting in the increase of the number of charge carriers (holes) and overall growth of the hybrid conductivity. Lack of electrical conductivity in the SPION(Sq) sample may be explained by an insulating shell made of squalane and dodecanoic acid which was shown in XPS results.

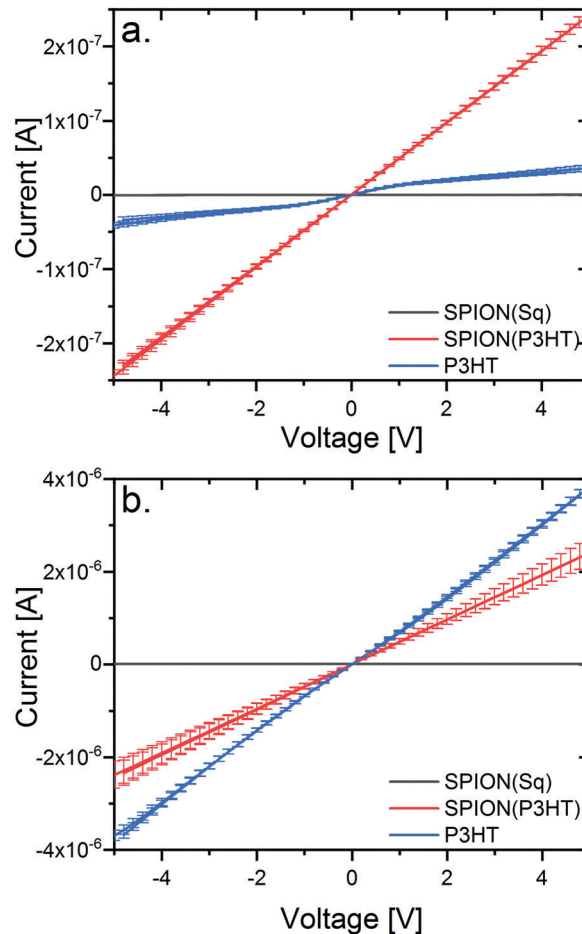


Fig. 4 I - V characteristics for pristine P3HT, SPION(Sq) and SPION(P3HT) in the dark (a) and under illumination (b), showing lack of conductivity in the SPION(Sq) nanoparticles, and a significant impact of illumination on the conductivity of pure polymer and SPION(P3HT) nanoparticles.

Additional attention was paid to the influence of light on the conductivity of composites consisting of either SPION(Sq) or SPION(P3HT) and P3HT. To study the influence of the carbon shell on the conductivity of the proposed materials, a high amount (30% wt) of nanoparticles was mixed with P3HT. As depicted in Fig. 5a, the most significant change in the dark can be seen for hybrids consisting of nanoparticles covered with the polymer and mixed with pure P3HT (six-time increase). For nanoparticles covered with capping agents (squalane and dodecanoic acid), only a minor impact on the sample's conductivity is observed (three-time increase), which may originate from the doping of the polymer by dodecanoic acid.³⁹ These results are in line with the UPS measurements of the valence state region shown in Fig. 5b. For the pristine P3HT the hole injection barrier height between the HOMO and Fermi-edge is the largest and is equal to 1.7 eV, whereas the addition of 30% SPION(Sq) to P3HT lowers this value to 1.4 eV, possibly due to the doping of the polymer by the capping agent. The lowest barrier (1 eV) is found for 30% SPION(P3HT) in the P3HT composite which explains its increase in conductivity compared to pristine P3HT.

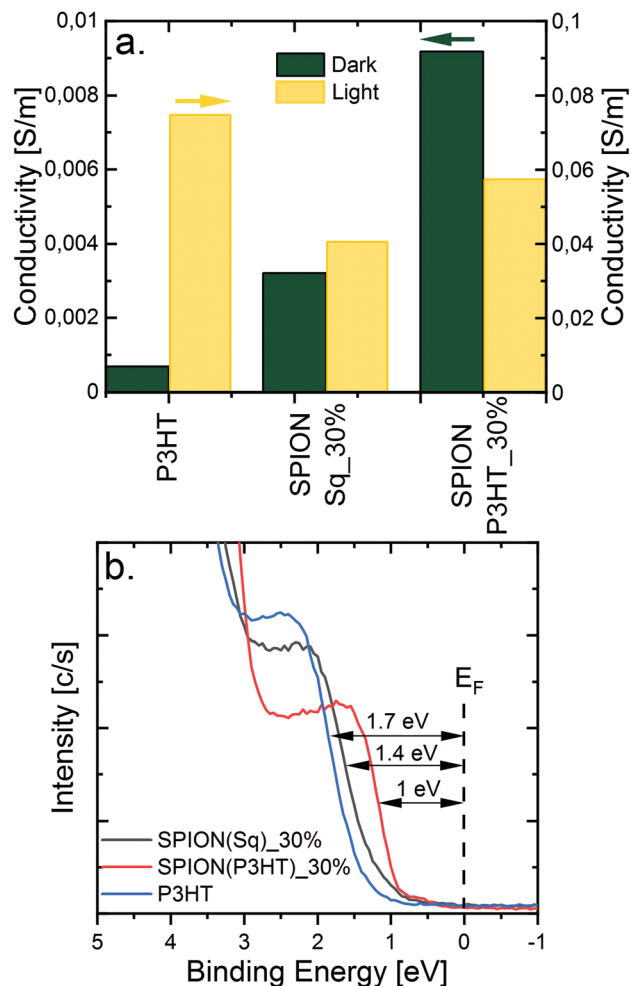


Fig. 5 (a) Conductivity values measured for the pure polymer, nanoparticles covered with capping agents and nanoparticles covered with P3HT. Under dark conditions, nanoparticles covered with squalane do not influence the conductivity of the polymer film, whereas nanoparticles synthesized *in situ* polymer matrix are enhancing conductivity over 9 times. (b) UPS measurements of valence states showing the HOMO edge shift for the pristine P3HT sample and 30% SPION(P3HT) and 30% SPION(Sq) in P3HT composites. It can be stated that the HOMO-Fermi edge barrier decreases from 1.7 eV for pristine P3HT to 1 eV for the composite made of 30% SPION(P3HT) in P3HT.

Under illumination the best performance is observed for pristine P3HT, but the trend for composites remains; higher conductivity is found for 30% SPION(P3HT) in the P3HT composite. The decrease of conductivity of 30% SPION(Sq) composite in relation to pristine P3HT can be explained by the fact that the addition of insulating nanoparticles decreases the P3HT content and thus, with the same volume, there is less material capable of conduction. However, it can be stated that under illumination the dominant influence on the conductivity is driven by P3HT.

Conclusions

Magnetic nanoparticles of two different shells, electrically insulating and conducting, were successfully created using the thermal decomposition method. The influence of the

created shell on the morphology, crystallographic structure, magnetic properties and conductivity of the proposed materials was thoroughly studied.

Both types of synthesized nanoparticles are single crystalline with a diameter of 10 nm. The alteration of the surface magnetic anisotropy made by the P3HT shell leads to the enhancement of surface spin disorientation, and additionally in the second prepared material, the decrease of magnetization is observed due to the carbon shell made of squalane and dodecanoic acid. Chemical characterization, based on FT-IR and XPS results, confirmed the presence of unmodified P3HT covering of magnetic nanoparticles with coordinate bonding between iron atoms and sulphur from the thiophene ring. Additionally, no negative alteration of sulphur, such as oxidation of the thiophene ring during synthesis, was observed.

In this study, we showed that stabilization of nanoparticles achieved by capping agents (such as squalane or dodecanoic acid) separates two elements of hybrid devices which results in a decrease of electrical performance. Nanoparticles synthesized directly in the polymer matrix are characterized by higher aggregation in the final polymer film, but the overall conductivity is enhanced significantly. These results show that hybrid devices consisting of magnetic nanoparticles and conducting polymers can possibly achieve even better results than those reported till now by designing the interface between the components of electronic devices.

Experimental

Materials

Fe(acac)₃ (acac = acetylacetonate) (97%), dibenzyl ether (≥98%), squalane (≥95%), dodecanoic acid (≥98%) and anhydrous dichlorobenzene were purchased from Sigma Aldrich. Poly(3-hexylthiophene-2,5-diyl) (P3HT) 51 000 molecular weight and over 90% regioregularity was purchased from Rieke Metals. All reagents were used as received.

As substrates for conductivity measurements, the Interdigitated ITO Substrates for OFET and Sensing (Ossila Ltd) were used.

Synthesis of Fe₃O₄ nanoparticles capped with P3HT (SPION(P3HT))

Magnetite nanoparticles were synthesized using the thermal decomposition method of iron acetylacetonate under an argon atmosphere. First, 60 mg of P3HT were dissolved in 45 ml of dibenzyl ether at 100 °C and kept in the dark for 12 hours. In the next step, the hot mixture was added to 15 ml of dibenzyl ether and 353 mg (1 mmol) of Fe(acac)₃ and was heated to around 200 °C and held for 90 minutes under a controlled continuous argon gas flow in a three-neck round-bottom flask. This step allowed complete dissolution and degassing of the mixture. In the last step of synthesis, the mixture was heated to over 280 °C and maintained at the same temperature for 60 minutes to allow particle formation.

The solution was left in argon overnight to cool down to room temperature. Then, the nanoparticles were cleaned using acetone by centrifugation (10 min, 10 000 rpm). The final product was suspended in dichlorobenzene and stored at 4 °C in the dark.

Synthesis of Fe₃O₄ nanoparticles capped with squalane (SPION(Sq))

Magnetite nanoparticles were synthesized using a thermal decomposition method of iron acetylacetonate under an argon atmosphere. The entire procedure was described previously in ref. 40. Briefly, 1 mmol of Fe(acac)₃, 3 mmol of dodecanoic acid, 15 ml of dibenzyl ether and 10 ml of squalane were mixed in a three-neck round-bottom flask under a continuous argon gas flow. First, the mixture was heated up to around 80 °C, and maintained for 60 minutes to assure complete dissolution of reagents. Second, the flask was heated up to around 200 °C and maintained for 60 minutes to assure good degassing of the solution. In the last step, the mixture was heated up to over 280 °C to reach the decomposition temperature of iron acetylacetonate and to allow nanoparticle formation.

As in the previous synthesis, the solution was left in argon for several hours to cool down to room temperature. After reaching around 20 °C, the nanoparticles were cleaned with acetone by centrifugation (10 min, 10 000 rpm). The final product was suspended in dichlorobenzene and stored at 4 °C in the dark.

Thin-film fabrication

The pre-patterned ITO substrates (Ossila Ltd.) with the overall channel dimensions of 30 mm × 50 μm with a 100 nm thickness of the ITO layer and a roughness of 1.8 nm RMS (data supported by Ossila Ltd) were used. Before the thin-film preparation, the substrates were ultrasonically cleaned in three steps: cleaning in 1% Hellmanex solution, deionized water and pure methanol. Each step took approximately 20 minutes. Additionally, two different solutions of nanoparticles, either covered with squalane or the polymer, were placed in the sonication bath for an hour prior to the thin film preparation process. Both, substrates and solutions, were transferred to an argon-filled glovebox (O₂ ≤ 0.1 ppm and H₂O ≤ 0.1 ppm).

For the conductivity measurements of pure nanoparticles and the polymer, the concentrated nanoparticle solutions were drop cast onto pre-patterned ITO substrates and annealed at 130 °C for 15 minutes. After that time, the contact pads were carefully cleaned with a cleanroom swab dipped in chloroform. All samples were left overnight in the glovebox to assure complete evaporation of dichlorobenzene and stabilization of the sample temperature.

In the case of thin-films for conductance measurements, an appropriate amount of nanoparticle solution was mixed with the polymer powder to obtain a final concentration of 30% weight content of nanoparticles in relation to 14 mg ml⁻¹ final concentration of P3HT. Such solutions were kept at 70 °C for 12 h in the glovebox to ensure full dissolution of the polymer without oxygen contamination. Later, the solutions were

transferred to the sonication bath for an hour and transferred back to the glovebox. Thin films were made on the spin coater with a speed of 1300 rpm for 60 s. After that time, the samples were annealed for 15 minutes at 130 °C and left overnight to ensure complete evaporation of the organic solvent and the stabilization of the samples' temperature.

Conductivity measurements

The *I-V* characteristics of thin films were determined with a Keithley model 2400 source meter and illumination generated with an AM1.5 solar simulator with an irradiation intensity of 100 mW cm⁻². To ensure that oxygen and humidity do not have an influence on the conductivity results, measurements were made in an argon-filled glovebox (O₂ ≤ 0.1 ppm and H₂O ≤ 0.1 ppm). All measurements were made using the two point probe method in the voltage range of -5 V to 5 V. All of the samples were prepared using the Interdigitated ITO Substrates for OFET and Sensing by Ossila Ltd.

Nanoparticle characterization techniques

To investigate the size and shape regularity of nanoparticles of both types, transmission electron microscopy (TEM) was employed. The preparation of samples consisted of dropwise addition of diluted nanoparticle solution onto a carbon coated copper grid and letting the solvent to evaporate overnight. Bright field images were taken using a Tecnai TF 20 X-TWIN (FEI). The crystalline structure of the obtained nanoparticles was examined using a PanAnalytical Empyrean diffractometer (Cu Kα = 1.5406 Å) in Bragg-Brentano mode using parallel beam geometry.

A vibrating sample magnetometer (VSM), type 7407 Lake-Shore Inc., was used to determine the magnetic properties of the obtained nanoparticles. Prior to the measurement, the nanoparticles suspended in dichlorobenzene were dried, and as a powder transferred to the apparatus in a Teflon vessel. Measurements were carried out at three different temperatures, 80 K, 290 K and 440 K, in an external magnetic field ranging from -1000 to 1000 mT. Additionally, to determine the blocking temperature evolution, zero field cooled (ZFC) and field cooled (FC) characteristics were determined at 10 mT.

To observe the influence of high temperature synthesis on the polymer chain, Fourier transform infrared spectroscopy (FTIR) was employed. Measurements of the dried samples were carried out using a Tensor II Spectrometer, Bruker, with a single reflection diamond ATR. A further study of changes in the chemical structure of nanoparticles was carried by X-ray photoelectron spectroscopy (XPS) combined with argon gas cluster ion beams (AR-GCIBs). A PHI 5000 VersaProbe II spectrometer with an Al Kα monochromatic X-ray beam with an X-ray source operating at 25 W and 15 kV beam voltages was employed. To avoid changes in the sample surface potential, dual beam compensation was applied - with 7 eV Ar⁺ ions and 1 eV electrons. Additionally, argon gas cluster ion beam sputtering of samples was carried out with approximately 4000 atoms per cluster which resulted in an energy of 4 eV per atom. The sputter area was set to 5 × 5 mm² with

Zalar rotation during sputtering. All spectra were charge corrected to the main carbon line at 284.8 eV.

Ultraviolet photoelectron spectroscopy (UPS) measurements were performed using PHI VersaProbe II apparatus (ULVAC-PHI, Chigasaki, Japan) using He I line (21.22 eV) from an UHV gas discharge lamp. Each sample was set to an acceleration potential of -5 V leading to a much more pronounced secondary electron cut off (SE cut-off). The work function (measured as the difference between the photon energy and SE cut-off position) and hole injection barrier (given by the difference of the substrate Fermi level to the HOMO onset of the material) were measured by UPS. For each UPS spectrum, the emission features due to the secondary line excitation of the He-I gas discharge are subtracted. Since the actual relative intensities of the satellite excitation depend on the He discharge pressure, the secondary line subspectra were adjusted marginally in intensity to the measured UPS spectrum and subtracted incrementally starting with the highest photon energy satellite. The measurement times were kept as short as possible to avoid UV degradation damage of the examined materials.

Conflicts of interest

There are no conflicts to declare.

Acknowledgements

The authors would like to thank Marcin Sikora and Juliusz Kuciakowski for discussing the magnetic properties of nanoparticles. This research was partly supported by the EU Project POWR.03.02.00-00-I004/16.

References

- 1 L. Wang, X. Li, X. Shi, M. Huang, X. Li, Q. Zeng and R. Che, *Nanoscale*, 2021, **13**, 2136–2156.
- 2 M. S. S. Dorraji, M. H. Rasoulifard, M. H. Khodabandloo, M. Rastgouy-Houjaghan and H. K. Zarajabad, *Appl. Surf. Sci.*, 2016, **366**, 210–218.
- 3 H. Zhang, G. Zhang, J. Li, X. Fan, Z. Jing, J. Li and X. Shi, *Composites, Part A*, 2017, **100**, 128–138.
- 4 J. Jaramillo, B. W. Boudouris, C. A. Barrero and F. Jaramillo, *ACS Appl. Mater. Interfaces*, 2015, **7**, 25061–25068.
- 5 K. Wang, C. Yi, X. Hu, C. Liu, Y. Sun, J. Hou, Y. Li, J. Zheng, S. Chuang and A. Karim, *ACS Appl. Mater. Interfaces*, 2014, **6**, 13201–13208.
- 6 J. Liang, C. Jiang and W. Wu, *Nanoscale*, 2019, **11**, 7041–7061.
- 7 M. T. Rahman, M. Asadul Hoque, G. T. Rahman, M. A. Gafur, R. A. Khan and M. K. Hossain, *Results Phys.*, 2019, **13**, 102264.
- 8 B. Yan, Y. Wang, X. Jiang, K. Liu and L. Guo, *ACS Appl. Mater. Interfaces*, 2017, **9**, 29113–29119.
- 9 K. Wang, C. Yi, C. Liu, X. Hu, S. Chuang and X. Gong, *Sci. Rep.*, 2015, **5**, 9265.
- 10 M. Romero, R. Faccio, M. A. Tumelero, A. A. Pasa and A. W. Mombrú, *J. Mater. Chem. C*, 2017, **5**, 3779–3787.
- 11 Y. N. Liang, K. Yu, Q. Yan and X. Hu, *ACS Appl. Mater. Interfaces*, 2013, **5**, 4100–4106.
- 12 W. Jaimes, G. Alvarado-Tenorio, C. Martínez-Alonso, A. Quevedo-López, H. Hu and M. E. Nicho, *Mater. Sci. Semicond. Process.*, 2015, **37**, 259–265.
- 13 S. E. Jacobo, J. C. Apesteguy, R. Lopez Anton, N. N. Schegoleva and G. V. Kurlyandskaya, *Eur. Polym. J.*, 2007, **43**, 1333–1346.
- 14 C. Barraud, P. Seneor, R. Mattana, S. Fusil, K. Bouzehouane, C. Deranlot, P. Graziosi, L. Hueso, I. Bergenti, V. Dediu, F. Petroff and A. Fert, *Nat. Phys.*, 2010, **6**, 615–620.
- 15 Q. Bao, S. Braun, C. Wang, X. Liu and M. Fahlman, *Adv. Mater. Interfaces*, 2019, **6**, 1–15.
- 16 M. Fahlman, S. Fabiano, V. Gueskine, D. Simon, M. Berggren and X. Crispin, *Nat. Rev. Mater.*, 2019, **4**, 627–650.
- 17 R. Pfattner, C. Rovira and M. Mas-Torrent, *Phys. Chem. Chem. Phys.*, 2014, **17**, 26545–26552.
- 18 S. A. Moiz, A. N. M. Alahmadi and K. S. Karimov, *Solid-State Electron*, 2020, **163**, 107658.
- 19 K. X. Steirer, G. A. Macdonald, S. Olthof, J. Gantz, E. L. Ratcliff, A. Kahn and N. R. Armstrong, *J. Phys. Chem. C*, 2013, **117**, 22331–22340.
- 20 Y. Kim, J. Zhu, B. Yeom, M. Di Prima, X. Su, J. G. Kim, S. J. Yoo, C. Uher and N. A. Kotov, *Nature*, 2013, **500**, 59–63.
- 21 D. Wilson and M. A. Langell, *Appl. Surf. Sci.*, 2014, **303**, 6–13.
- 22 T. Yang, Y. Shi, A. Janssen and Y. Xia, *Angew. Chem., Int. Ed.*, 2020, **59**, 15378–15401.
- 23 A. Lassenberger, T. A. Grünwald, P. D. J. Van Oostrum, H. Renhoffer, H. Amenitsch, R. Zirbs, H. C. Lichtenegger and E. Reimhult, *Chem. Mater.*, 2017, **29**, 4511–4522.
- 24 A. Heuer-Jungemann, N. Feliu, I. Bakaimi, M. Hamaly, A. Alkilany, I. Chakraborty, A. Masood, M. F. Casula, A. Kostopoulou, E. Oh, K. Susumu, M. H. Stewart, I. L. Medintz, E. Stratakis, W. J. Parak and A. G. Kanaras, *Chem. Rev.*, 2019, **119**, 4819–4880.
- 25 J. A. Cuenca, K. Bugler, S. Taylor, D. Morgan, P. Williams, J. Bauer and A. Porch, *J. Phys.: Condens. Matter*, 2016, **28**(10), 106002.
- 26 N. Seidler, G. M. Lazzarini, G. L. Destri, G. Marletta and F. Cacialli, *J. Mater. Chem. C*, 2013, **1**, 7748–7757.
- 27 W. Wang, C. Chen, C. Tollan, F. Yang, Y. Qin and M. Knez, *J. Mater. Chem. C*, 2017, **5**, 2686–2694.
- 28 Y. Ge, Y. Zhang, J. Xia, M. Ma, S. He, F. Nie and N. Gu, *Colloids Surf., B*, 2009, **73**, 294–301.
- 29 S. Majumdar, J. O. Lill, J. Rajander and H. Majumdar, *Org. Electron.*, 2015, **21**, 66–72.
- 30 I. J. Bruvera, P. Mendoza Zélis, M. Pilar Calatayud, G. F. Goya and F. H. Sánchez, *J. Appl. Phys.*, 2015, **118**, 184304.
- 31 H. D. Jin, F. Zheng, W. L. Xu, W. H. Yuan, M. Q. Zhu and X. T. Hao, *J. Phys. D: Appl. Phys.*, 2014, **47**, 3–9.
- 32 R. D. K. Misra, D. Depan, V. S. A. Challa and J. S. Shah, *Phys. Chem. Chem. Phys.*, 2014, **16**, 19122–19129.

- 33 A. H. Rezayan, M. Mosavi, S. Kheirjou, G. Amoabediny, M. S. Ardestani and J. Mohammadnejad, *J. Magn. Magn. Mater.*, 2016, **420**, 210–217.
- 34 Y. P. Lee, C. J. Chiang, P. C. Jen, B. T. Chou, L. Wang, Y. Y. Cheng, Y. H. Lee, Y. F. Chen, C. C. Hsieh and C. A. Dai, *ACS Appl. Energy Mater.*, 2018, **1**, 1930–1941.
- 35 P. J. Cumpson, J. F. Portoles, A. J. Barlow and M. Birch, *Surf. Interface Anal.*, 2013, 1859–1868.
- 36 M. Gosecka, J. Raczowska, J. Haberkowicz, K. Awsiuk, J. Rysz, A. Budkowski, M. M. Marzec, A. Bernasik and T. Basinska, *Colloids Surf., A*, 2016, **507**, 200–209.
- 37 T. Radu, C. Iacovita, D. Benea and R. Turcu, *Appl. Surf. Sci.*, 2017, **405**, 337–343.
- 38 R. M. Cornell and U. Schwertmann, *The iron oxides: structure, properties, reactions, occurrences, and uses*, Wiley-VCH, 1996.
- 39 Y. Wu, Y. Li and B. S. Ong, *J. Am. Chem. Soc.*, 2006, **128**, 4202–4203.
- 40 D. Lachowicz, R. Wirecka, W. Górka-Kumik, M. M. Marzec, M. Gajewska, A. Kmita, J. Żukrowski, M. Sikora, S. Zapotoczny and A. Bernasik, *Phys. Chem. Chem. Phys.*, 2019, **21**, 23473–23484.

Electronic Supplementary Information

The effect of shell modification in iron oxide nanoparticles on electrical conductivity in polythiophene-based nanocomposite

Roma Wirecka,^{*a,b} Mateusz M. Marzec,^b Marianna Marciszko-Wiąckowska,^b Maria Lis,^b Marta Gajewska,^b Elżbieta Trynkiewicz,^b Dorota Lachowicz,^b Andrzej Beransik^{a,b}

^a AGH University of Science and Technology, Faculty of Physics and Applied Computer Science, A. Mickiewicza Av. 30, 30-059 Cracow, Poland. E-mail: roma.wirecka@fis.agh.edu.pl

^b AGH University of Science and Technology, Academic Centre for Materials and Nanotechnology, A. Mickiewicza Av. 30, 30-059 Cracow, Poland.

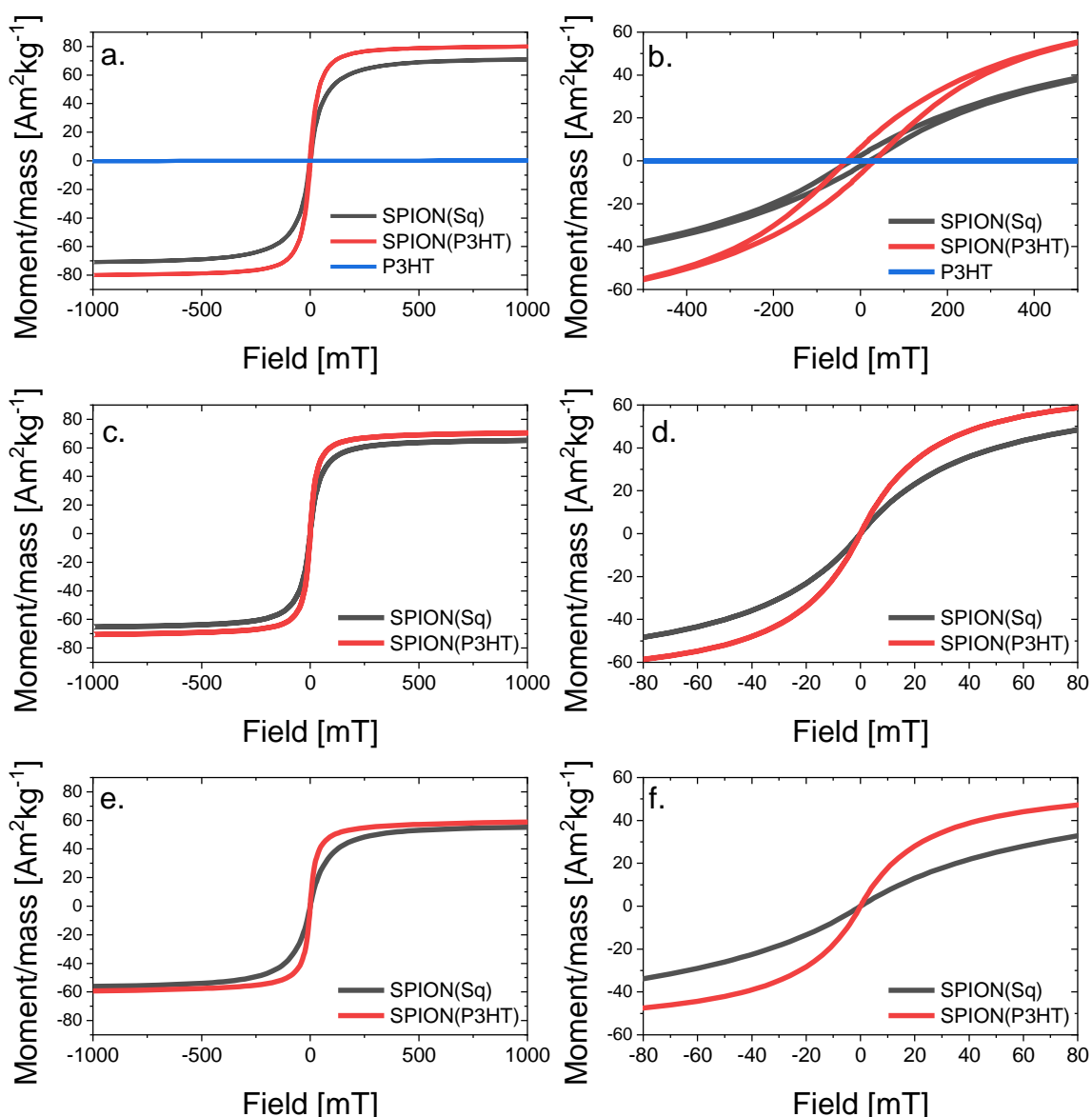


Figure 1. M-H loops for powder samples of P3HT, SPION(P3HT) and SPION(Sq) in three different temperatures, namely: (a, b) 80 K, (c, d) 290 K, (e, f) 440 K

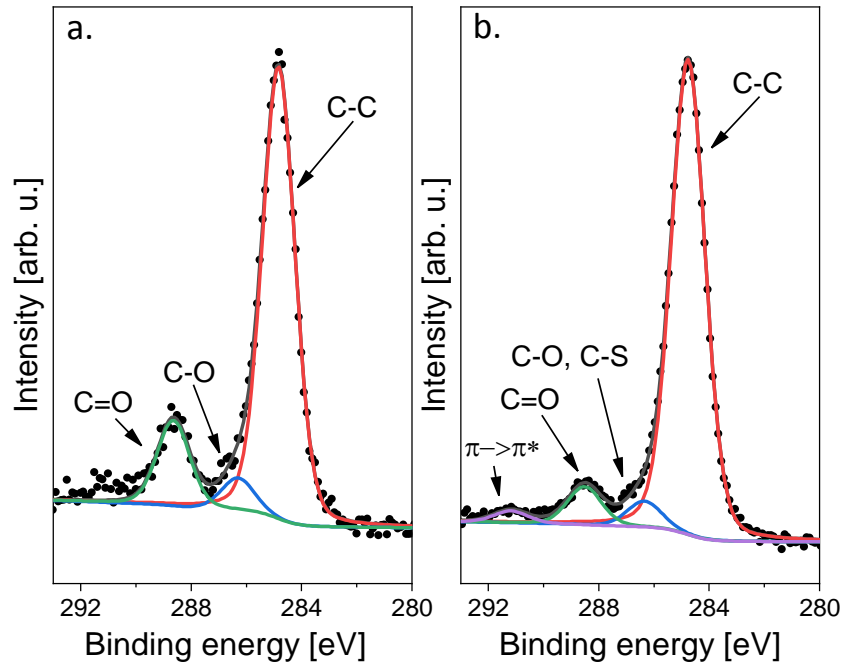


Figure 2. XPS spectra of C 1s region acquired for (a) SPION(Sq) and (b) SPION(P3HT)

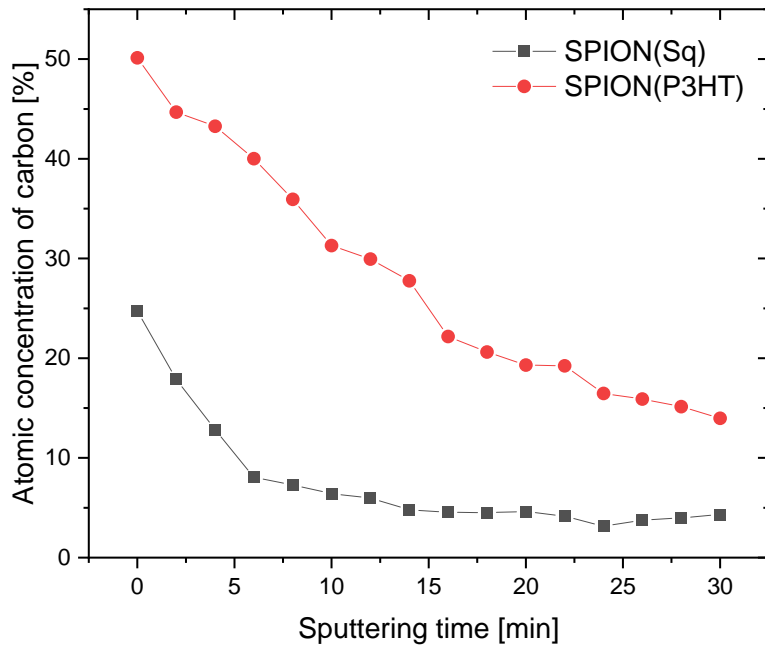


Figure 3. XPS derived changes of atomic concentration in SPION(Sq) and SPION(P3HT) samples during Ar-GCIB sputtering



Article

Magnetoresistive Properties of Nanocomposites Based on Ferrite Nanoparticles and Polythiophene

Roma Wirecka ^{1,2,*} , Krzysztof Maćkosz ^{1,2,3} , Antoni Żywczak ² , Mateusz Marek Marzec ² ,
Szczepan Zapotoczny ^{2,4} and Andrzej Bernasik ^{1,2}

- ¹ Faculty of Physics and Applied Computer Science, AGH University of Science and Technology, al. Adama Mickiewicza 30, 30-059 Krakow, Poland
- ² Academic Centre for Materials and Nanotechnology, AGH University of Science and Technology, al. Adama Mickiewicza 30, 30-059 Krakow, Poland
- ³ Empa-Swiss Federal Laboratories for Materials Science and Technology, Laboratory for Mechanics of Materials and Nanostructures, Feuerwerkerstrasse 39, CH-3602 Thun, Switzerland
- ⁴ Faculty of Chemistry, Jagiellonian University, ul. Gronostajowa 2, 30-387 Krakow, Poland
- * Correspondence: roma.wirecka@fis.agh.edu.pl

Abstract: In the presented study, we have synthesized six nanocomposites based on various magnetic nanoparticles and a conducting polymer, poly(3-hexylthiophene-2,5-diyl) (P3HT). Nanoparticles were either coated with squalene and dodecanoic acid or with P3HT. The cores of the nanoparticles were made of one of three different ferrites: nickel ferrite, cobalt ferrite, or magnetite. All synthesized nanoparticles had average diameters below 10 nm, with magnetic saturation at 300 K varying between 20 to 80 emu/g, depending on the used material. Different magnetic fillers allowed for exploring their impact on the conducting properties of the materials, and most importantly, allowed for studying the influence of the shell on the final electromagnetic properties of the nanocomposite. The conduction mechanism was well defined with the help of the variable range hopping model, and a possible mechanism of electrical conduction was proposed. Finally, the observed negative magnetoresistance of up to 5.5% at 180 K, and up to 1.6% at room temperature, was measured and discussed. Thoroughly described results show the role of the interface in the complex materials, as well as clarify room for improvement of the well-known magnetoelectric materials.

Keywords: magnetic nanoparticles; magnetoresistance; magnetic nanocomposites



Citation: Wirecka, R.; Maćkosz, K.; Żywczak, A.; Marzec, M.M.; Zapotoczny, S.; Bernasik, A. Magnetoresistive Properties of Nanocomposites Based on Ferrite Nanoparticles and Polythiophene. *Nanomaterials* **2023**, *13*, 879. <https://doi.org/10.3390/nano13050879>

Academic Editor: Zhidong Zhang

Received: 8 February 2023

Revised: 22 February 2023

Accepted: 23 February 2023

Published: 26 February 2023



Copyright: © 2023 by the authors. Licensee MDPI, Basel, Switzerland. This article is an open access article distributed under the terms and conditions of the Creative Commons Attribution (CC BY) license (<https://creativecommons.org/licenses/by/4.0/>).

1. Introduction

Having both electrical properties and magnetic response, with addition of possible flexibility and ease of synthesis, nanocomposites based on conducting polymers and magnetic nanoparticles are of high interest both in the scientific and commercial worlds [1,2]. Continuous studies aiming at a better understanding of their electrical properties, the influence of the filler, and the interface between components, on the final properties of the nanocomposite materials resulted in numerous reports showing new methods for their synthesis and potential applications [3–8].

Among many interesting and adjustable properties of such composite materials, the alteration of their properties under the influence of the magnetic field (magnetic field effects—MFE) is of high interest. The influence of the magnetic field was observed to have an impact on the photocurrent (magneto-photocurrent) [9,10], electroluminescence (magneto-electroluminescence) [11,12], electrical current (magneto-electrical current, magnetoresistance, magnetoconductance) [13,14], and other properties [15]. All those properties mainly originate from three phenomena: carrier recombination, exciton dissociation, and electric polarization. As the external magnetic field introduces coherent and incoherent spin precessions, the spin of the electron may be affected. As a result, it can remain unchanged or it can alter its orientation, which leads to positive or negative MFEs, respectively [16].

Among other MFEs, one that is constantly drawing attention to the polymer-magnetic nanoparticle composites is magnetoresistance (MR). It is described as the alteration of the electrical resistivity (R) of the material in the external magnetic field (H).

$$\%MR = \frac{R_H - R_0}{R_0} \times 100\% \quad (1)$$

The positive MR is seen as the increase, while the negative MR results in the decrease of the resistivity in the external magnetic field. The use of magnetic semiconducting nanoparticles allows for tuning the conductivity of the material [17,18]. Thanks to the magnetic properties of the filler, the magnetic response can be modified, and the MR can be amplified [19].

This study presents the synthesis of six different core-shell nanoparticles which are later suspended in the electrically conductive polymer matrix to obtain nanocomposites with magnetoelectric properties. The shell of the nanoparticle, made of either insulating material (squalene and dodecanoic acid) or conducting material (poly(3-hexylthiophene-2,5-diyl)), covers a magnetic core made of one of three different ferrites. The morphology and magnetic properties of the nanoparticles are thoroughly analyzed to help understand the differences between the obtained nanoparticles. Finally, the electrical and magnetoresistive properties of thin composite films made of nanoparticles suspended in P3HT are carefully studied to establish the influence of the shell-covering nanoparticle on the conductivity mechanism.

2. Materials and Methods

2.1. Materials

$\text{Fe}(\text{acac})_3$ (acac = acetylacetonate) (97%), $\text{Ni}(\text{acac})_2$ (97%), $\text{Co}(\text{acac})_2$ (97%), dibenzyl ether (98%), squalene (95%), dodecanoic acid (98%), and anhydrous dichlorobenzene were purchased from Sigma Aldrich. Poly(3-hexylthiophene-2,5-diyl) (P3HT) $M_w = 51,000$ u and over 90% regioregularity was purchased from Rieke Metals. All reagents were used as received.

2.2. Synthesis of Nanoparticles Capped with Squalene

The synthesis of the Fe_3O_4 nanoparticles (Fe(Sq)) was based on the thermal decomposition of the acetylacetonates in a controlled argon gas atmosphere, thoroughly described in our previous work [20]. The synthesis of cobalt (Co(Sq)) and nickel ferrites (Ni(Sq)) followed the same protocol, but the molar ratio of iron to dopant was chosen to be 2/1. The synthesis consisted of three stages: dissolving of the solution (at 80 °C for one hour), degassing (at 200 °C for one hour), and the formation of nanoparticles from decomposed metal acetylacetonates (at 280 °C for one hour). After this time the content of the flask is left overnight to cool down and then cleaned with acetone by centrifugation (10 min, 10,000 rpm) at least three times. Afterward, the nanoparticles are suspended in the dichlorobenzene and stored in the dark at 4 °C.

2.3. Synthesis of Nanoparticles Capped with P3HT

The synthesis of magnetite nanoparticles capped with P3HT (Fe(P3HT)) was already described in our previous work [20]. The synthesis of nickel (Ni(P3HT)) or cobalt (Co(P3HT)) ferrite follows the same procedure with the molar ratio of iron to the chosen dopant being 2/1. Briefly, the synthesis consists of three steps. Firstly, a flask containing P3HT and dibenzyl ether is kept at 100 °C for 12 h in dark to assure good dissolution of the polymer. Then, the solution is transferred to the pre-heated (200 °C) flask containing dibenzyl ether and the proper amount of metal acetylacetonate and kept for 90 min. The final stage, in which the decomposition of the acetylacetonate and nanoparticles' formation takes place, lasts 60 min at 280 °C. After the synthesis, the mixture is kept in argon gas for 12 h to cool down, then is cleaned with acetone by centrifugation (10 min, 10,000 rpm). Cleaned nanoparticles are suspended in the dichlorobenzene and kept in the dark at 4 °C.

2.4. Nanocomposite Preparation

Nanoparticles obtained following the previously described procedures (NP(Sq) for nanoparticles capped with squalene and NP(P3HT) for nanoparticles covered with P3HT) were suspended in P3HT dissolved in dichlorobenzene. The concentration of polymer was set to 14 mg/mL and nanoparticles to 10 mg/mL. The solutions were put in the ultrasonic bath for one hour to ensure good distribution of the nanoparticles in the polymer solution. Six different prepared solutions were further used to obtain nanocomposite films.

2.5. Vibrating Sample Magnetometry

For the magnetic characterization of obtained nanoparticles, a vibrating sample magnetometer (VSM), type 7407 Lake Shore Cryotronics, Inc., (Westerville, OH, USA) was chosen. Before the measurement, the nanoparticles were dried, and as a powder transferred to the apparatus in a Teflon vessel. All measurements were conducted at three temperatures: low (80 or 100 K), nearly room temperature (290 or 300 K), and high (440 K), in an external magnetic field ranging from -1500 mT to 1500 mT.

2.6. Conductivity Measurements of Nanocomposites

Substrates for the conductivity measurements were custom made. They consisted of two 100 nm thick gold electrodes evaporated on top of the SiO_2 wafer/substrate. The distance between electrodes was set to 75 μm .

Nanocomposite solutions were drop cast on the described substrates in the argon-filled glovebox ($\text{O}_2 \leq 0.1$ ppm and $\text{H}_2\text{O} \leq 0.1$ ppm). The samples were annealed at 130 $^\circ\text{C}$ for 15 min and left overnight to cool down. Afterward, the contact pads were cleaned with a cleanroom swab dipped in dichlorobenzene. Samples were transferred in the isolated sample holder to the VSM apparatus equipped with a conductivity measurement holder. The continuous nitrogen gas flow in the apparatus ensured the elimination of the oxygen and humidity in the vicinity of the sample. Conductivity measurements were carried out using the two-point method with a Keithley 2400 source meter. The distance between the electrodes was set to 75 μm . The $R(T)$ characteristics were collected at different temperatures ranging from 200 K to 400 K.

2.7. Conductivity Measurements of Nanocomposites in the External Magnetic Field

Samples were prepared in the same manner as for $R(T)$ measurements. The external magnetic field was applied parallel to the sample's surface. The magnetic field was applied in the sequence starting at 0 mT, then increasing to 1500 mT, and then changing to -1500 mT, and finishing at 0 mT with the 10 mT/s step and 5 V applied to the sample to measure the magnetoconductivity of the sample. The same measurements were conducted in the temperature regime ranging from 300 K to 200 K, all with the same sequence.

3. Results

3.1. Morphology of the Nanoparticles

The morphology with the corresponding histograms of all six types of obtained nanoparticles is presented in Figure 1. The Fe(Sq) and Co(Sq) samples are characterized by regular cubic and hexagonal shapes with ~ 10 nm diameter, while Fe(P3HT) samples have the same mean diameter (~ 10 nm) but their dispersity of size is higher. The Co(P3HT) particles are slightly smaller (~ 7 nm) and irregular, similar to Fe(P3HT). The most regular shapes, hence least defected structures, were obtained from the pure Fe_3O_4 and nanoparticles doped with cobalt in the presence of surface agents—squalene and dodecanoic acid. There is a visible distinction between nanoparticles synthesized directly in the polymer matrix and the surface agent—nanoparticles in the presence of polymer become more irregular and smaller. The aggregation of nickel and cobalt ferrite nanoparticles is similar, but pure Fe_3O_4 nanoparticles synthesized in the presence of polymer are not aggregated at all. A possible explanation is that the magnetic interactions between the particles are much smaller in comparison to the Fe(Sq) or Co(Sq), which can be established during the VSM

measurement. Secondly, there is a possibility the polymer coverage is stabilizing small nanoparticles. The dispersity of sizes between NP(Sq) and NP(P3HT) is similar in two out of three types of nanoparticles, which is surprising and shows that the use of size- and shape-controlling mediums during the synthesis, such as squalene and dodecanoic acid, has little effect on the distribution of sizes, but affects the regularity of obtained shapes.

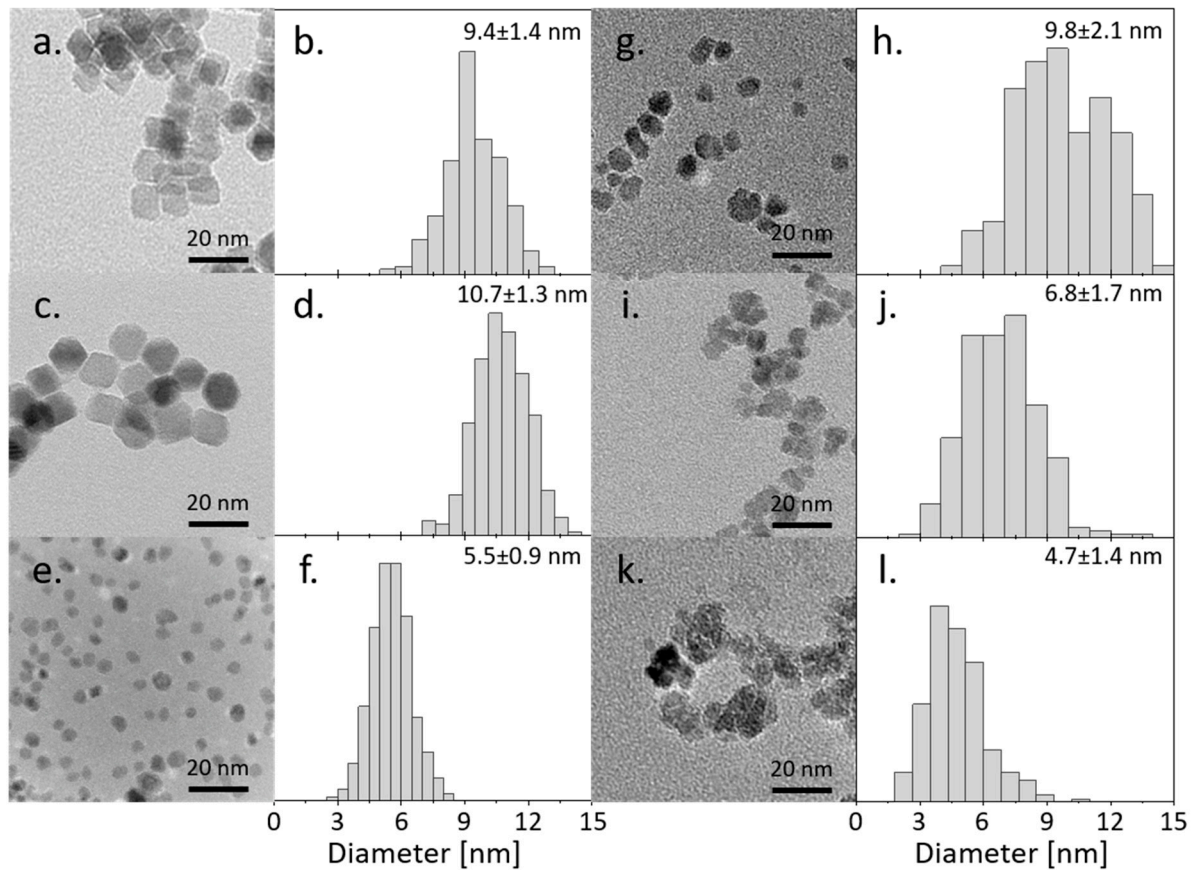


Figure 1. TEM micrograph with corresponding histograms of synthesized nanoparticles: (a,b) Fe(Sq); (c,d) Co(Sq); (e,f) Ni(Sq); (g,h) Fe(P3HT); (i,j) Co(P3HT); (k,l) Ni(P3HT).

3.2. Magnetic Characterization

The magnetic hysteresis loops of as-received nanoparticles at three different temperatures are presented in Figure 2. The saturation magnetization (M_s) of all synthesized nanoparticles with corresponding bulk values taken from the literature are presented in Table 1. The M_s is a characteristic value of the field that aligns all of the magnetic moments in the sample. The comparison of alterations of values between the bulk and the nanoparticles allows making some assumptions about the magnetic dead layer (MDL) [19] and the influence of the synthesis on the magnetic properties and structure. The largest difference between the bulk value and the M_s of the nanoparticle is observed for Co(P3HT) and Ni(Sq) nanoparticles, which is probably caused by the structural distortions present at the surface of the nanoparticles in the samples. Additionally, almost no difference of M_s is observed for magnetite nanoparticles, showing that the magnetic properties are similar regardless of the less regular size of Fe(P3HT) and different outer layers. The M_s of nickel nanoparticles is four times smaller than magnetite (and two times smaller than cobalt ferrite nanoparticles), which is a result of the highest proportion between the surface and the core. Since the surface may be treated as a defected structure, the MDL will have the biggest impact on the magnetic properties when the nanoparticles' size is decreasing. The results for Co(P3HT) nanoparticles support this hypothesis: Co(Sq)'s M_s and the nanoparticle's diameter are two times bigger than those of Co(P3HT). Worth pointing out is the lack of (or very low)

coercivity in almost all samples (Co(Sq) in 100 K being one exception), which shows that the addition of polymer to the nanoparticles does not have a negative, insulating impact on the magnetic properties of the composite, which was observed for a similar P(VDF-HFP)/Cobalt ferrite nanocomposite [21].

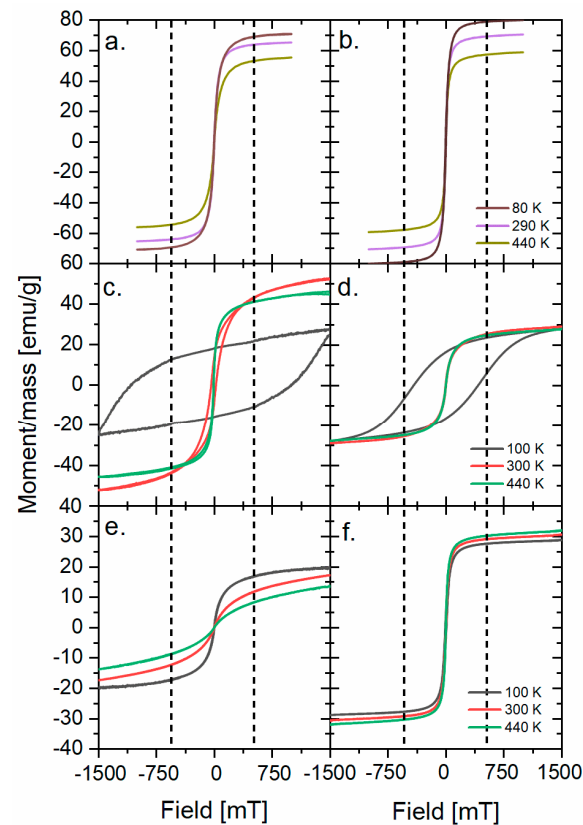


Figure 2. M(H) loops for (a) Fe(Sq), (b) Fe(P3HT), (c) Co(Sq), (d) Co(P3HT), (e) Ni(Sq), and (f) Ni(P3HT). The dotted lines show the field value for which the magnetization saturation for 300 K is observed.

Table 1. Summary of sizes and saturation magnetization in 300 K of all samples.

Sample	Diameter [nm]	Experimental M_s for NPs [emu/g]	M_s for Bulk at 300 K [emu/g]
Fe(Sq)	9.4 ± 1.4	65.5	96.0 [22]
Fe(P3HT)	9.8 ± 2.1	70.0	
Co(Sq)	10.7 ± 1.3	52.7	80.8 [23]
Co(P3HT)	6.8 ± 1.7	28.9	
Ni(Sq)	5.5 ± 0.9	16.9	55.0 [24]
Ni(P3HT)	4.7 ± 1.4	30.6	

Next, the electrical properties of nanocomposites based on the nanoparticles described above were checked. The materials were studied without and with the magnetic field applied during the conductivity measurements.

3.3. Electric Properties

To determine the electrical conductivity mechanism of obtained nanocomposites, the resistivity of the samples was measured at temperatures ranging from 200 to 400 K. Because the resistivity is decreasing with the increase of temperature, the nanocomposites

are typical semiconducting materials with a negative temperature coefficient (insets in Figure 3). Such results suggest a thermally activated conduction mechanism [25] in which the charge carriers are tunneling or hopping between nanoparticles and P3HT.

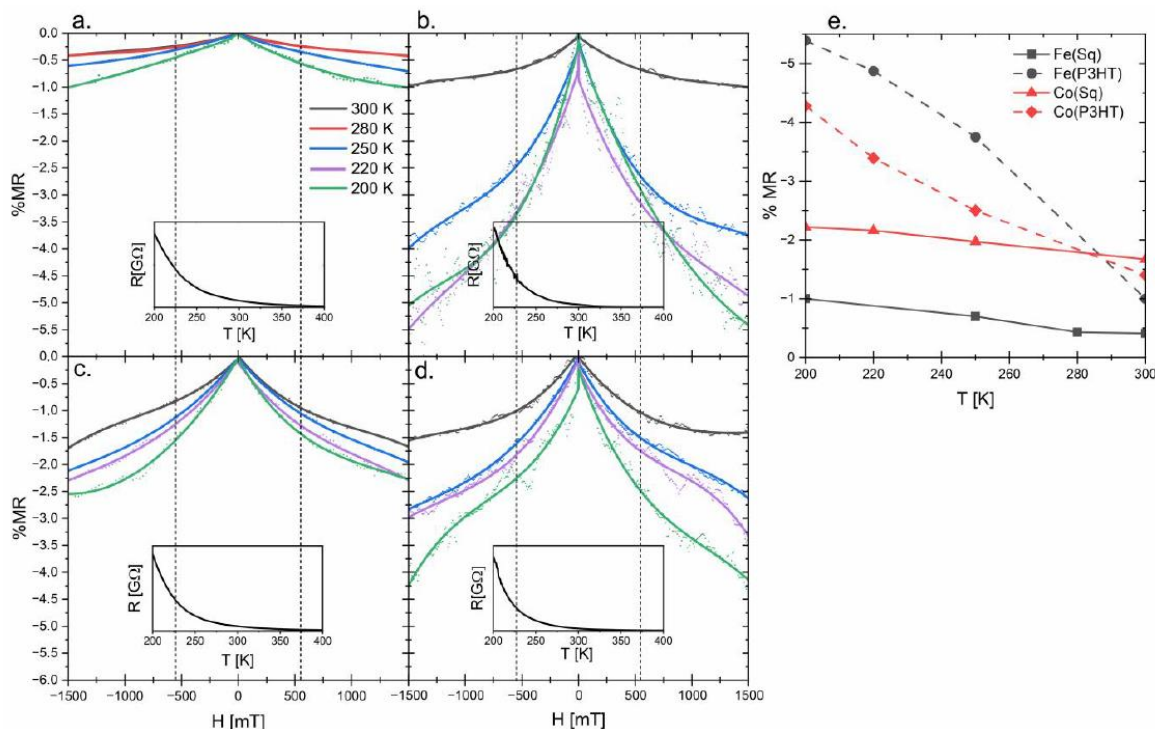


Figure 3. Graphs presenting changes in the magnetoresistance: (a) Fe(Sq), (b) Fe(P3HT), (c) Co(Sq), and (d) Co(P3HT); the lines present in the graphs are to guide the over the results; the insets of the R(H) characteristics prove semiconducting properties of obtained materials; (e) is a summary of the MR values in the 1500 mT at different temperatures.

The conductivity of polymers and their composites strongly depends on the structural order of the system [26]. One of the elements affecting it is the disorder of the polymer chains, which may be influenced by the addition of nanoparticles. The disordered state can be defined as the conductivity ratio measured at different temperatures, or by the Mott temperature calculated from the Mott Variable range hopping conductivity model (VRH) [27]. To express the value of the composite’s disorder, the ratio of the resistance values at 200 K and 300 K was calculated (Table 2). For the pure P3HT, it was not possible to measure resistance below 300 K in our measuring setup, so the disorder was not analyzed, hence in the discussion only synthesized composites are included.

Table 2. Disorder ratio for different types of synthesized nanocomposites with calculated resistance at low temperature and Mott’s temperatures (T_0).

Nanocomposite Sample	Resistivity Ratio R_{200K}/R_{300K}	R_0 [Ohm]	T_0 10^7 [K]
Fe(Sq)	11.1	8.8×10^{-4}	9.22
Fe(P3HT)	28.5	2.0×10^{-11}	94.37
Co(Sq)	14.6	2.8×10^{-5}	11.75
Co(P3HT)	33.6	2.5×10^{-7}	29.15
Ni(Sq)	17.8	1.7×10^{-5}	45.32
Ni(P3HT)	44.7	6.0×10^{-7}	32.47

The conductivities of nanoparticles covered with squalene and dodecanoic acid were measured. The results showed that the resistivity of the samples is so high that it can be concluded that nanoparticles are insulators. For the nanoparticles covered with P3HT, the conductivity was measurable [20]. Only after creating nanocomposites, was it possible to observe electrical conductivity for materials based on both NP(Sq) and NP(P3HT). Since conductivity was measured for all synthesized nanocomposites, the significant influence of the nanoparticles in charge carrier transport is proven. The composites in which nanoparticles were covered with squalene show a more than two times smaller disorder ratio than those in which nanoparticles were coated with polymer. Additionally, it can be observed, that with the change in type of ferrite, the ratio increases from 11.1 for Fe(Sq) to 17.8 for Ni(Sq) and from 28.5 for Fe(P3HT) to 44.7 for Ni(P3HT). These results show that the addition of nanoparticles affects the conducting behavior of the samples in a consistent manner. One probable explanation of the disorder difference is that squalene insulates nanoparticles, which causes only small alterations of the polymer matrix conduction paths. On the other hand, when the composite consists of the polymer and NP(P3HT), the inclusion of chains covering the magnetic nanoparticle in the polymer matrix causes additional distortions and interactions between polymer chains, which greatly increases the disorder of the conduction paths. Furthermore, in the materials based on NP(P3HT), the highly spin-polarized charge carriers injected from the nanoparticles may be transferred to the polymer chain and influence the conductivity of the polymer matrix. In the case of NP(Sq), the barrier may be too high to inject any charge carrier into the polymer matrix [28].

To further study the conduction mechanism of the synthesized materials, the VRH model is applied. Following Guo et al. [29], Equation (2) was used to determine it.

$$\ln\left(\frac{1}{R}\right) = \ln\left(\frac{1}{R_0}\right) - \left(\frac{T_0}{T}\right)^{\frac{1}{1+n}} \quad n = 1, 2, 3 \quad (2)$$

In Equation (2), R is the resistivity of the sample, R_0 is the resistivity of the sample at the infinitely low temperature, T is the temperature (K), and n is the constant <1,3>, which reflects the dimension of the system. Mott temperature (T_0) is related to the decay length of the localized wave function of the charge carriers and the DOS at the Fermi level and is also known as a hopping barrier [30]. The results of the calculations are summarized in Table 2. Since the T_0 is correlated with the disorder of the polymer [31], the results should also reflect the data for the resistivity ratio. Such correlations are observed for four out of six studied composites. For magnetite and cobalt ferrite nanoparticles, both the resistivity ratio and T_0 increase for samples covered with P3HT. This correlation and the fact that samples follow the function trend very well suggest a quasi-3D VRH electrical conduction mechanism for the four measured samples. We believe that the hopping of the carriers may occur between P3HT covering NP(P3HT) and the polymer matrix, and at the same time, the transport may occur along the polymer backbone [29,32]. On the other hand, when nanoparticles are covered with the P3HT, the polymeric shell may affect the polymer chains present in the sample. Additionally, the magnetic core of the nanoparticles stabilizes the spin of the charge carriers and lowers the probability of scattering. Since the magnetic fringe field decreases as the third power of the diameter, if the nanoparticle is not covered with any insulating layer, the influence of such magnetic core is higher, which also leads to lowering the scattering probability.

3.4. Magnetoresistive Properties

The magnetoresistance of four out of six synthesized materials is presented in Figure 3. In the case of pure P3HT and nickel ferrite nanoparticles, no change in the resistivity was observed. Since no response was observed for pure polymer in the VSM measurement, no response to the external magnetic field was expected for these samples. For the nickel-doped nanoparticles, the VSM measurement suggested MDL covering nanoparticles, which may influence the spin orientation of the charges leaving the core of the nanoparticle [19].

Additionally, the charge carrier transport through the polymer matrix is limited by hopping between less-disordered regions [33]. Knowing that it is highly probable that these two effects occur in the materials synthesized with nickel-containing nanoparticles, no MR was expected. Nanocomposites based on magnetite and cobalt ferrite, show different results. For each of the thin films, the resistance of the material is decreasing with the increase of the applied magnetic field (Figure 3e). This is the result of the lowered scattering of the charge carriers between polymer chains and/or nanoparticles present in the material [34]. Even though saturation magnetization is observed for all samples at all temperatures (Figure 2), no saturation of the magnetoresistivity is observed. The hyperfine interactions and spin-orbit splitting have the most significant influence on MR in the field strength up to 500 mT; thus these two phenomena do not explain the conductivity response to the increase in the magnetic field. Worth noting is the fringe field coming from the core of magnetic nanoparticles. In the presented system, nanoparticles are distributed throughout the polymer matrix, which possibly influences the MR in high-strength fields. The described magnetoresistance results are summarized in Figure 3e. For NP(P3HT), the comparison of the results, obtained at room and lower temperatures, shows that even a small change of temperature allows for obtaining much better results. At 200 K, which was the lowest measured temperature, the MR in 1500 mT for Fe(P3HT) reaches almost 5.5%, which is 5.5 times better than observed in the composite containing NP(Sq). It is clearly visible that the composites based on the NP(Sq) show a smaller change of the conductance even in the high-strength fields, and it does not change with the alteration of the temperature. These distinctions between the two types of composites, and the lack of saturation of MR, may be explained by the forward interference model proposed by Nguyen, Spivan, and Shlovskii (the NSS model) [35]. In this model, the conductivity of a material is a sum of all possible conduction paths, so when NP(Sq) is used as a filler, it does not add much to the conductivity, but when nanoparticles are covered with the conductive shell, the enhancement should occur. If we take into consideration the T_0 (which is often taken as a parameter connected to the charge carrier scattering probability [27]) and the fact that at lower temperatures the chance of scattering is lower, then the impact of the shell may play a significant role in the number of possible conduction paths and their interference, which is visible in our results. Additionally, in this model, no saturation of magnetoresistance for material is observed even in high-strength fields.

4. Conclusions

In conclusion, we have created six different nanocomposites, based on magnetic nanoparticles, covered with two types of shells (insulating and conducting), and an electrically conductive polymer matrix. Electrical conductivity measurements have proven a significant influence of the nanoparticles on the charge carrier transport. Results suggest a quasi-3D VRH electrical conduction mechanism for nanocomposites in which magnetite, cobalt, or nickel ferrite nanoparticles were used as fillers. Moreover, we have shown that the choice of shell-covering for the magnetic nanoparticle has a major impact on both the conduction paths in the nanocomposites and the probability of charge carrier scattering. Furthermore, we have shown higher negative magnetoresistance for nanocomposites based on nanoparticles covered with a conductive polymeric shell. We have observed the relationship between the saturation magnetization of nanoparticles and the magnetoresistance change. The highest magnetoresistance variation, of up to 5.5% at a magnetic field of 1500 mT, was measured for the nanocomposite based on the magnetite nanoparticles covered with a conductive shell. As a takeaway summary, our nanocomposites which combine electrical conductivity with a magnetic response can be used as easily made thin sensors of magnetic fields or as new scalable materials for organic spintronic applications.

Author Contributions: Conceptualization, R.W. and A.B.; methodology, R.W., K.M. and A.Ž.; validation, M.M.M. and A.B.; formal analysis, R.W.; investigation, R.W. and A.B.; resources, R.W. and A.B.; data curation, R.W.; writing—original draft preparation, R.W.; writing—review and editing, A.B.,

M.M.M. and S.Z.; visualization, R.W.; supervision, A.B.; funding acquisition, A.B. All authors have read and agreed to the published version of the manuscript.

Funding: This research and RW were partly supported by the EU Project POWR.03.02.00-00-I004/16 and by the “Excellence Initiative—Research University” program for the AGH University of Science and Technology.

Data Availability Statement: The data presented in this study are available on request from the corresponding author.

Conflicts of Interest: The authors declare no conflict of interest. The funders had no role in the design of the study, in the collection, analyses, or interpretation of data, in the writing of the manuscript and in the decision to publish the results.

References



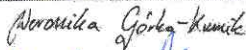
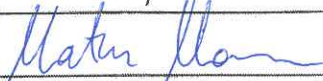
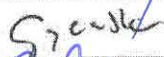
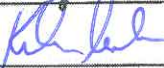




1. Kausar, A. *Conducting Polymer-Based Nanocomposites: Fundamentals and Applications*; Elsevier: Amsterdam, The Netherlands, 2021; ISBN 9780128224632.
2. Hosseini, S.H.; Rahimi, R.; Kerdari, H. Preparation of a Nanocomposite of Magnetic, Conducting Nanoporous Polyaniline and Hollow Manganese Ferrite. *Polym. J.* **2011**, *43*, 745–750. [[CrossRef](#)]
3. Shahrman, M.S.; Mohamad Zain, N.N.; Mohamad, S.; Abdul Manan, N.S.; Yaman, S.M.; Asman, S.; Raoov, M. Polyaniline Modified Magnetic Nanoparticles Coated with Dicationic Ionic Liquid for Effective Removal of Rhodamine B (RB) from Aqueous Solution. *RSC Adv.* **2018**, *8*, 33180–33192. [[CrossRef](#)]
4. Bai, H.; Zheng, Y.; Wang, T.; Peng, N. Magnetic Solvent-Free Nanofluid Based on Fe₃O₄/Polyaniline Nanoparticles and Its Adjustable Electric Conductivity. *J. Mater. Chem. A* **2016**, *4*, 14392–14399. [[CrossRef](#)]
5. Agayev, F.G.; Trukhanov, S.V.; Trukhanov, A.V.; Jabarov, S.H.; Ayyubova, G.S.; Mirzayev, M.N.; Trukhanova, E.L.; Vinnik, D.A.; Kozlovskiy, A.L.; Zdorovets, M.V.; et al. Study of Structural Features and Thermal Properties of Barium Hexaferrite upon Indium Doping. *J. Therm. Anal. Calorim.* **2022**, *147*, 14107–14114. [[CrossRef](#)]
6. Zdorovets, M.V.; Kozlovskiy, A.L.; Shlimas, D.I.; Borgekov, D.B. Phase Transformations in FeCo—Fe₂CoO₄/Co₃O₄-Spinel Nanostructures as a Result of Thermal Annealing and Their Practical Application. *J. Mater. Sci. Mater. Electron.* **2021**, *32*, 16694–16705. [[CrossRef](#)]
7. El-Ghobashy, M.A.; Hashim, H.; Darwish, M.A.; Khandaker, M.U.; Sulieman, A.; Tamam, N.; Trukhanov, S.V.; Trukhanov, A.V.; Salem, M.A. Eco-Friendly NiO/Polydopamine Nanocomposite for Efficient Removal of Dyes from Wastewater. *Nanomaterials* **2022**, *12*, 1103. [[CrossRef](#)] [[PubMed](#)]
8. Xu, J.; Zeng, G.; Lin, Q.; Gu, Y.; Wang, X.; Feng, Z.; Sengupta, A. Application of 3D Magnetic Nanocomposites: MXene-Supported Fe₃O₄@CS Nanospheres for Highly Efficient Adsorption and Separation of Dyes. *Sci. Total Environ.* **2022**, *822*, 153544. [[CrossRef](#)]
9. Li, W.; Yuan, S.; Zhan, Y.; Ding, B. Tuning Magneto-Photocurrent between Positive and Negative Polarities in Perovskite Solar Cells. *J. Phys. Chem. C* **2017**, *121*, 9537–9542. [[CrossRef](#)]
10. Sheng, Z.G.; Nakamura, M.; Koshibae, W.; Makino, T.; Tokura, Y.; Kawasaki, M. Magneto-Tunable Photocurrent in Manganite-Based Heterojunctions. *Nat. Commun.* **2014**, *5*, 1–7. [[CrossRef](#)]
11. Gärditz, C.; Mückl, A.G.; Cölle, M. Influence of an External Magnetic Field on the Singlet and Triplet Emissions of Tris-(8-Hydroxyquinoline)Aluminum(III) (Alq₃). *J. Appl. Phys.* **2005**, *98*, 104507. [[CrossRef](#)]
12. Faulkner, L.R.; Tachikawa, H.; Bard, A.J. Electrogenerated Chemiluminescence. VII. the Influence of an External Magnetic Field on Luminescence Intensity. *J. Am. Chem. Soc.* **1972**, *94*, 691–699. [[CrossRef](#)]
13. Das, K.; Dasgupta, P.; Poddar, A.; Das, I. Significant Enhancement of Magnetoresistance with the Reduction of Particle Size in Nanometer Scale. *Sci. Rep.* **2016**, *6*, 20351. [[CrossRef](#)]
14. Tang, H.; Liang, Y.; Liu, C.; Hu, Z.; Deng, Y.; Guo, H.; Yu, Z.; Song, A.; Zhao, H.; Zhao, D.; et al. A Solution-Processed n-Type Conducting Polymer with Ultrahigh Conductivity. *Nature* **2022**, *611*, 271–277. [[CrossRef](#)] [[PubMed](#)]
15. Trukhanov, A.V.; Almessiere, M.A.; Baykal, A.; Slimani, Y.; Trukhanova, E.L.; Timofeev, A.V.; Kostishin, V.G.; Trukhanov, S.V.; Sertkol, M.; Ul-Hamid, A. Correlation between the Composition, Structural Parameters and Magnetic Properties of Spinel-Based Functional Nanocomposites. *Nano-Struct. Nano-Objects* **2023**, *33*, 100941. [[CrossRef](#)]
16. Xu, H.; Wang, M.; Yu, Z.G.; Wang, K.; Hu, B. Magnetic Field Effects on Excited States, Charge Transport, and Electrical Polarization in Organic Semiconductors in Spin and Orbital Regimes. *Adv. Phys.* **2019**, *68*, 49–121. [[CrossRef](#)]
17. Salehiyan, R.; Sinha Ray, S.; Salehiyan, R.; Ray, S.S. Tuning the Conductivity of Nanocomposites through Nanoparticle Migration and Interface Crossing in Immiscible Polymer Blends: A Review on Fundamental Understanding. *Macromol. Mater. Eng.* **2019**, *304*, 1800431. [[CrossRef](#)]
18. Elizalde, M.L.M.; Acha, C.; Moreno, M.S.; Antonel, P. Tuning Electrical and Magnetic Properties in Multifunctional Composite Materials Based on PEDOT:DBS Conducting Polymer and Magnetite Nanoparticles. *J. Mater. Chem. C* **2022**, *10*, 18264–18278. [[CrossRef](#)]

19. Geng, R.; Luong, H.M.; Pham, M.T.; Das, R.; Stojak Repa, K.; Robles-Garcia, J.; Duong, T.A.; Pham, H.T.; Au, T.H.; Lai, N.D.; et al. Magnetically Tunable Organic Semiconductors with Superparamagnetic Nanoparticles. *Mater. Horiz.* **2019**, *6*, 1913–1922. [[CrossRef](#)]
20. Wirecka, R.; Marzec, M.M.; Marciszko-Wiąckowska, M.; Lis, M.; Gajewska, M.; Trynkiewicz, E.; Lachowicz, D.; Bernasik, A. The Effect of Shell Modification in Iron Oxide Nanoparticles on Electrical Conductivity in Polythiophene-Based Nanocomposites. *J. Mater. Chem. C* **2021**, *9*, 10453–10461. [[CrossRef](#)]
21. Prathipkumar, S.; Hemalatha, J. Magnetoelectric Response and Tunneling Magnetoresistance Behavior of Flexible P(VDF-HFP)/Cobalt Ferrite Nanofiber Composite Films. *Ceram. Int.* **2020**, *46*, 258–269. [[CrossRef](#)]
22. Mascolo, M.C.; Pei, Y.; Ring, T.A. Room Temperature Co-Precipitation Synthesis of Magnetite Nanoparticles in a Large Ph Window with Different Bases. *Materials* **2013**, *6*, 5549–5567. [[CrossRef](#)] [[PubMed](#)]
23. Stein, C.R.; Bezerra, M.T.S.; Holanda, G.H.A.; André-Filho, J.; Morais, P.C. Structural and Magnetic Properties of Cobalt Ferrite Nanoparticles Synthesized by Co-Precipitation at Increasing Temperatures. *AIP Adv.* **2018**, *8*, 056303. [[CrossRef](#)]
24. Nejati, K.; Zabihi, R. Preparation and Magnetic Properties of Nano Size Nickel Ferrite Particles Using Hydrothermal Method. *Chem. Cent. J.* **2012**, *6*, 23. [[CrossRef](#)] [[PubMed](#)]
25. Cho, S.J.; Kauzlarich, S.M.; Olamit, J.; Liu, K.; Grandjean, F.; Rebbouh, L.; Long, G.J. Characterization and Magnetic Properties of Core/Shell Structured Fe/Au Nanoparticles. *J. Appl. Phys.* **2004**, *95*, 6804–6806. [[CrossRef](#)]
26. Liu, C.; Huang, K.; Park, W.T.; Li, M.; Yang, T.; Liu, X.; Liang, L.; Minari, T.; Noh, Y.Y. A Unified Understanding of Charge Transport in Organic Semiconductors: The Importance of Attenuated Delocalization for the Carriers. *Mater. Horiz.* **2017**, *4*, 608–618. [[CrossRef](#)]
27. Gu, H.; Guo, J.; Yan, X.; Wei, H.; Zhang, X.; Liu, J.; Huang, Y.; Wei, S.; Guo, Z. Electrical Transport and Magnetoresistance in Advanced Polyaniline Nanostructures and Nanocomposites. *Polymer* **2014**, *55*, 4405–4419. [[CrossRef](#)]
28. Wang, S.; Yue, F.J.; Wu, D.; Zhang, F.M.; Zhong, W.; Du, Y.W. Enhanced Magnetoresistance in Self-Assembled Monolayer of Oleic Acid Molecules on Fe₃O₄ Nanoparticles. *Appl. Phys. Lett.* **2009**, *94*, 2–5. [[CrossRef](#)]
29. Guo, J.; Chen, Z.; Abdul, W.; Kong, J.; Khan, M.A.; Young, D.P.; Zhu, J.; Guo, Z. Tunable Positive Magnetoresistance of Magnetic Polyaniline Nanocomposites. *Adv. Compos. Hybrid Mater.* **2021**, *4*, 534–542. [[CrossRef](#)]
30. Gu, H.; Zhang, X.; Wei, H.; Huang, Y.; Wei, S.; Guo, Z. An Overview of the Magnetoresistance Phenomenon in Molecular Systems. *Chem. Soc. Rev.* **2013**, *42*, 5907–5943. [[CrossRef](#)] [[PubMed](#)]
31. Sarkar, A.; Ghosh, P.; Meikap, A.K.; Chattopadhyay, S.K.; Chatterjee, S.K.; Ghosh, M. Direct and Alternate Current Conductivity and Magnetoconductivity of Oxalic Acid Doped Polyaniline. *Solid State Commun.* **2007**, *143*, 358–363. [[CrossRef](#)]
32. Guo, J.; Gu, H.; Wei, H.; Zhang, Q.; Haldolaarachchige, N.; Li, Y.; Young, D.P.; Wei, S.; Guo, Z. Magnetite-Polypyrrole Metacomposites: Dielectric Properties and Magnetoresistance Behavior. *J. Phys. Chem. C* **2013**, *117*, 10191–10202. [[CrossRef](#)]
33. Noruzi, R.; Lim, E.; Pokuri, B.S.S.; Chabinyk, M.L.; Ganapathysubramanian, B. A Graph Based Approach to Model Charge Transport in Semiconducting Polymers. *npj Comput. Mater.* **2022**, *8*, 38. [[CrossRef](#)]
34. Prasanna, G.D.; Jayanna, H.S.; Prasad, V. Preparation, Structural, and Electrical Studies of Polyaniline/ZnFe₂O₄ Nanocomposites. *J. Appl. Polym. Sci.* **2011**, *120*, 2856–2862. [[CrossRef](#)]
35. Nguen, V.L.; Spivak, B.Z.; Shklovskii, B.I. Tunnel Hopping in Disordered Systems. *JETP Lett.* **1985**, *62*, 1021–1026.

Disclaimer/Publisher's Note: The statements, opinions and data contained in all publications are solely those of the individual author(s) and contributor(s) and not of MDPI and/or the editor(s). MDPI and/or the editor(s) disclaim responsibility for any injury to people or property resulting from any ideas, methods, instructions or products referred to in the content.

Statement of percentage contribution to the publication

I hereby give the author's percentage contribution to the publication entitled „Gradient of zinc content in core-shell zinc ferrite nanoparticles – precise study on composition and magnetic properties”, Physical Chemistry Chemical Physics, 2019, 21(42), 23473, doi: 10.1039/c9cp03591e

Name of the co-author	Percentage contribution	Signature
Lachowicz Dorota	30%	
Wirecka Roma	30%	
Górka-Kumik Weronika	5%	
Marzec Marek Mateusz	5%	
Gajewska Marta	5%	
Kmita Angelika	5%	
Żukrowski Jan	5%	
Sikora Marcin	5%	
Zapotoczny Szczepan	5%	
Bernasik Andrzej	5%	

Statement of percentage contribution to the publication

I hereby give the author's percentage contribution to the publication entitled "Ion distribution in iron oxide, zinc and manganese ferrite nanoparticles studied by XPS combined with argon gas cluster ion beam sputtering", Surfaces and Interfaces, 2022, 30, 101865, doi: 10.1016/j.surfin.2022.101865

Name of the co-author	Percentage contribution	Signature
Wirecka Roma	70%	Roma Wirecka
Lachowicz Dorota	5%	Dorota Lachowicz
Berent Katarzyna	5%	Katarzyna Berent
Marzec Marek Mateusz	5%	Mateusz Marzec
Bernasik Andrzej	15%	Andrzej Bernasik

Oświadczenie o procentowym udziale autorów w publikacji naukowej z 2021 roku

Ja, niżej podpisana/-y oświadczam, że zgadzam się z procentowym udziałem w niniejszej publikacji naukowej:

Roma Wirecka, Mateusz M. Marzec, Marianna Marciszko-Wiąckowska, Maria Lis, Marta Gajewska, Elżbieta Trynkiewicz, Dorota Lachowicz, Andrzej Bernasik, "The effect of shell modification in iron oxide nanoparticles on electrical conductivity in polythiophene-based nanocomposites", J. Mater. Chem. C, 2021,9, 10453-10461; doi: <https://doi.org/10.1039/D1TC02949E>

Autor	Udział procentowy	Czytelny podpis
Wirecka Roma	60%	Roma Wirecka
Marzec M. Mateusz	5%	Mateusz Marzec
Marciszko – Wiąckowska Marianna	5%	Marciszko - Wiąckowska
Lis Maria	5%	Maria Lis
Gajewska Marta	5%	Marta Gajewska
Trynkiewicz Elżbieta	5%	Trynkiewicz Elżbieta
Lachowicz Dorota	5%	Dorota Lachowicz
Bernasik Andrzej	10%	Andrzej Bernasik

Kraków, 27.01.2022

Statement of percentage contribution to the publication

I hereby give the author's percentage contribution to the publication entitled „Magnetoresistive Properties of Nanocomposites Based on Ferrite Nanoparticles and Polythiophene”, *Nanomaterials*, 2023, 13(5), 879; doi: 10.3390/nano13050879

Name of the co-author	Percentage contribution	Signature
Wirecka Roma	65%	Roma Wirecka
Maćkosz Krzysztof	5%	
Żywczak Antoni	5%	
Marzec Marek Mateusz	5%	Marek Marzec
Zapotoczny Szczepan	5%	Szczepan Zapotoczny
Bernasik Andrzej	15%	Andrzej Bernasik

Statement of percentage contribution to the publication

I hereby give the author's percentage contribution to the publication entitled „Magnetoresistive Properties of Nanocomposites Based on Ferrite Nanoparticles and Polythiophene”, *Nanomaterials*, 2023, 13(5), 879; doi: 10.3390/nano13050879

Name of the co-author	Percentage contribution	Signature
Wirecka Roma	65%	Roma Wirecka
Maćkosz Krzysztof	5%	Maćkosz
Żywczak Antoni	5%	
Marzec Marek Mateusz	5%	Marek Marzec
Zapotoczny Szczepan	5%	
Bernasik Andrzej	15%	Andrzej Bernasik

Statement of percentage contribution to the publication

I hereby give the author's percentage contribution to the publication entitled „Magnetoresistive Properties of Nanocomposites Based on Ferrite Nanoparticles and Polythiophene”, *Nanomaterials*, 2023, 13(5), 879; doi: 10.3390/nano13050879

Name of the co-author	Percentage contribution	Signature
Wirecka Roma	65%	Roma Wirecka
Maćkosz Krzysztof	5%	
Żywczak Antoni	5%	Żywczak Antoni
Marzec Marek Mateusz	5%	Marek Marzec
Zapotoczny Szczepan	5%	
Bernasik Andrzej	15%	Andrzej Bernasik